

# **Diffuse stellar components in galaxies and galaxy clusters**

Dissertation der Fakultät für Physik  
der  
Ludwig-Maximilians-Universität München

vorgelegt von Stefano Zibetti  
aus Gallarate, Italien

München, den 20. September 2004

1. Gutachter: Prof. Dr. Simon D. M. White
2. Gutachter: Prof. Dr. Ralf Bender

Erstgutachter: Prof. Dr. Simon D. M. White

Zweitgutachter: Prof. Dr. Ralf Bender

Tag der mündlichen Prüfung: 19. Oktober 2004

*Ai miei genitori*



# Contents

<b>Zusammenfassung (Summary in German)</b>	<b>3</b>
<b>Summary</b>	<b>5</b>
<b>1 Introduction: framework, motivations and method</b>	<b>7</b>
1.1 The evolving Universe: the growth of structures and the role of interactions . . . . .	7
1.2 Diffuse stellar components . . . . .	8
1.2.1 The Galactic halo and galaxy haloes . . . . .	9
1.2.2 The Intracluster Light . . . . .	17
1.3 Low Surface Brightness Photometry: the observational challenge	23
1.3.1 Statistics against photometric limitations . . . . .	25
1.4 The Sloan Digital Sky Survey . . . . .	25
1.5 The thesis . . . . .	27
References . . . . .	31
<b>2 The stellar halo of disc galaxies</b>	<b>33</b>
2.1 Haloes around edge-on disk galaxies in the Sloan Digital Sky Survey . . . . .	33
2.1.1 Introduction . . . . .	33
2.1.2 The Sample . . . . .	35
2.1.3 The image stacking . . . . .	37
2.1.4 The analysis . . . . .	42
2.1.5 Discussion . . . . .	53
2.1.6 Summary and conclusions . . . . .	59
2.2 A faint red stellar halo around an edge-on disc galaxy in the Hubble Ultra Deep Field . . . . .	65
2.2.1 Introduction . . . . .	65
2.2.2 Observations and Analysis . . . . .	66
2.2.3 Results . . . . .	69
2.2.4 Discussion . . . . .	73

## Contents

---

<b>3</b>	<b>The optical emission from intracluster stars at <math>z \sim 0.25</math></b>	<b>79</b>
3.1	Introduction . . . . .	80
3.2	The sample . . . . .	83
3.2.1	Sample properties . . . . .	85
3.3	The image processing and stacking . . . . .	88
3.4	The photometric analysis . . . . .	91
3.4.1	Definition of the ICL and corrections for mask incom- pleteness . . . . .	93
3.5	Results . . . . .	95
3.5.1	Surface brightness profiles . . . . .	95
3.5.2	Colours of the ICL . . . . .	97
3.5.3	Isophotal ellipticity . . . . .	97
3.5.4	ICL–galaxy connection . . . . .	101
3.5.5	Dependence on cluster properties: SB profiles . . . . .	103
3.5.6	Dependence on cluster properties: integral photometry .	106
3.6	Systematic uncertainties . . . . .	108
3.6.1	Background subtraction . . . . .	108
3.6.2	Corrections for mask incompleteness . . . . .	110
3.7	Discussion . . . . .	113
3.8	Conclusions . . . . .	118
<b>4</b>	<b>Conclusions and outlook</b>	<b>125</b>
	<b>Acknowledgements</b>	<b>129</b>
	<b>Curriculum Vitae</b>	<b>131</b>

# Zusammenfassung

Im derzeit verbreitetsten Szenario entwickelt sich das Universum von einer äußerst homogenen Phase, die aus dem Urknall hervorging, in den heutigen Zustand, der durch eine Vielzahl hierarchisch organisierter Strukturen gekennzeichnet ist, die einige Größenordnungen überspannen: Galaxien, Galaxienhaufen (Cluster), Superhaufen, Wälle und Filamente. Strukturen bilden sich durch gravitative Instabilitäten und wachsen hierarchisch: die kleinsten "Halos" kollabieren zuerst und wachsen dann durch das Ansammeln von Masse aus anderen Halos (Akkretion) oder durch das Verschmelzen mit anderen ähnlichen Strukturen (Merging). Gravitative und dynamische Wechselwirkungen wie Merging, Akkretion, von Gezeitenkräften verursachte Verformungen und komplette Zerstörung spielen daher eine grundlegende Rolle bei der Formung von Galaxien und Galaxienhaufen. Als natürliches Nebenprodukt dieser Wechselwirkungen werden Sterne, die sich ursprünglich in den Galaxien befanden, in die Umgebung der Galaxien und in den Raum zwischen ihnen hinausgeschleudert, sodaß sie dort eine diffuse stellare Komponente stellen. Eine Untersuchung dieser Komponenten kann wichtige Details über die Galaxien- und Clusterbildung enthüllen und ist daher von großem Interesse.

Beobachtungen auf diesem Gebiet werden allerdings dadurch ernsthaft erschwert, daß die zu messende Flächenhelligkeit extrem schwach ist. Sie entspricht nur einem 1/1.000 der typischen Helligkeit des Himmelshintergrundes. Bis jetzt hat dieser Umstand verhindert, daß eine umfangreiche, statistisch signifikante Anzahl an Sternhalos oder Intraclusterpopulationen von Sternen hätten beobachtet werden können.

Die statistische Charakterisierung von Sternhalos und Intraclusterlicht ist das Thema dieser Dissertation. Zu diesem Zweck habe ich eine neue Methode entwickelt, die darin besteht eine große Anzahl ( $\sim 1.000$ ) von relativ wenig tief belichteten Aufnahmen gleichartiger Objekte übereinanderzulegen (Stacking), um so ein extrem tief belichtetes gemittelttes Bild zu erhalten. Systematische Effekte, die durch Kontamination von Fremdquellen und instrumentelle Unterschiede bei der Beobachtung individueller Objekte entstehen, heben sich auf, indem das Mittel aus vielen verschiedenen Beobachtungen gebildet und eine konservative Maskierung der verschmutzenden Fremdquellen gewählt wird. Die umfangreiche Datenbank an Aufnahmen, die für diese Technik benötigt

## Zusammenfassung

---

wird, steht in Form des Sloan Digital Sky Survey zur Verfügung, der größten Katalogisierung des Universums im optischen Licht, die jemals unternommen wurde. Sie wird schlußendlich  $\sim 10.000$  Quadratgrad am Himmel abdecken, inklusive Photometrie in fünf Bändern und Spektroskopie.

Im ersten Teil meiner Dissertation habe ich die stellaren Halos von Scheibengalaxien untersucht. Das Ergebnis aus 1043 kombinierten Aufnahmen führt zu der Schlußfolgerung, daß diese Komponente so gut wie überall in der Umgebung von Galaxienscheiben vorkommt, was zeigt, daß Halos wichtige Bestandteile bei der Galaxienevolution sind. Im Mittel haben stellare Halos ein Profil, das einem Potenzgesetz entspricht, wie auch die Milchstraße und M31. Ihre Form ist nur leicht abgeflacht. Die durchschnittlichen Farben der Sternhalos weisen auf alte und ziemlich metallreiche Sterne hin. Allerdings wurde ein rätselhafter Helligkeitsüberschuß in den extrem roten Bändern gemessen, der nicht durch irgendeine stellare Emission erklärt werden kann, sondern auf das Vorhandensein ionisierten Gases hinweist. Diese Ergebnisse wurden durch die Analyse einer Galaxie, die das Hubble Space Telescope in seiner bislang am längsten belichteten Aufnahme (Ultra Deep Field) beobachtet hat, bestätigt.

Der zweite Teil der Dissertation ist der Untersuchung des Intraclusterlichtes (ICL) gewidmet, was mittels des Übereinanderlegens der Aufnahmen von 683 Galaxienhaufen in einem Rotverschiebungsbereich zwischen 0.2 und 0.3 bewerkstelligt wurde. Durchschnittlich trägt das ICL innerhalb eines 700 kpc Radius vom Haufenzentrum  $10.9 \pm 5\%$  zur Gesamthelligkeit eines Galaxienclusters bei. Das ICL ist bedeutend stärker zum Zentrum hin konzentriert, als das Licht in Galaxien, was mit der Vorstellung konsistent ist, daß das ICL durch das Zerren der Gezeitenkräfte an den Galaxien entsteht, die tief in das Gravitationspotential des Clusters fallen, wodurch ihnen Sterne verlorengehen, oder sie völlig auseinandergerissen werden. Die Farben des ICL stimmen mit jenen der Galaxien im Haufen überein, was darauf hinweist, daß die Intraclustersterne von der selben Population stammen wie die Sterne in Galaxien. Eine weitere Feststellung ist, daß die Menge an ICL mit der Helligkeit der Zentralgalaxie im Haufen, und mit der Anzahl an Haufenmitgliedern korreliert. Zudem entspricht die Ausrichtung des ICL eher jener der Zentralgalaxie, als jener der großräumigen Galaxienverteilung im Cluster. Beides ist ein starkes Indiz dafür, daß der Mechanismus, durch den sich das ICL gebildet hat, in engem Zusammenhang mit der Tiefe vom Gravitationspotential des Haufens steht.

# Summary

In currently favoured scenarios, the Universe evolves from a highly homogeneous phase, emerging from the hot Big Bang, to the present-day state, which is characterised by a wealth of hierarchically organised structures, spanning several orders of magnitudes in size: galaxies, clusters of galaxies, superclusters, walls and filaments. Structures are formed via gravitational instability and grow hierarchically: the smallest “haloes” collapse first and then grow by accreting mass from other haloes or by merging with other similar structures. Gravitational and dynamical interactions, like mergers, accretions, tidal distortions and disruptions thus play a fundamental role in shaping galaxies and galaxy clusters. As a natural by-product of these interactions, stars, originally located within galaxies, are ejected into the space surrounding galaxies and into intracluster space, giving rise to diffuse stellar components. The study of these components can reveal important details of galaxy and cluster formation, and are therefore of great interest.

Observations in this field are severely hampered by the extremely low surface brightness that has to be measured, corresponding to less than 1/1,000 of the typical surface brightness of the sky. So far, this has prevented observing large statistical samples of stellar haloes and intracluster stellar populations.

The statistical characterisation of stellar haloes and of the intracluster light is the objective of this thesis. In order to do this, I have developed a new method in which a large number ( $\approx 1,000$ ) of relatively shallow images of homogeneous objects are stacked to produce an extremely deep average image. Systematic effects that arise from contaminating sources and instrumental biases in the observation of individual objects are cancelled out by taking the average of many different observations and by adopting a conservative masking of the polluting sources. The large image database required for this technique has been provided by the Sloan Digital Sky Survey, the largest optical survey of the Universe ever undertaken, which will eventually cover  $\approx 10,000$  square degrees of sky with 5-band photometry and spectroscopy.

In the first part of the thesis I have studied the stellar haloes of disc galaxies. From the stacking of 1043 galaxies I have been able to infer the almost ubiquitous presence of this component around discs, thus demonstrating that haloes are essential ingredients of galaxy evolution. On average, stellar haloes

## Summary

---

have power-law profiles, consistent with those of the Milky Way and M31. Their shape is moderately flattened. The average halo colours hint at old and fairly metal-enriched stars. However, a puzzling emission excess in the redmost bands has been measured that cannot be explained by any stellar emission, but suggests the presence of ionised gas. These results have been confirmed by the analysis of a galaxy, which has been observed by the Hubble Space Telescope in its deepest exposure (the Ultra Deep Field).

The second part of the thesis is devoted to a study of the intracluster light (ICL) from the stacking of a sample of 683 clusters of galaxies in the redshift range 0.2–0.3. The average contribution of the ICL to the total light of a cluster is  $10.9 \pm 5\%$  within 500 kpc from the cluster centre. The ICL is significantly more centrally concentrated than the light in galaxies, consistent with the idea that the ICL is formed via tidal stripping and disruption of galaxies that plunge deep into the cluster potential. The colours of the ICL are consistent with those of the cluster galaxies, thus indicating that the intracluster stars stem from the same population as the stars in galaxies. The amount of ICL correlates with the luminosity of the central galaxy of the cluster and with cluster richness. Furthermore, the ICL aligns more strongly with the central galaxy than with the larger scale galaxy distribution in the cluster. This strongly suggest that the efficiency of formation of the ICL is strongly dependent on the depth of the gravitational potential well of a cluster.

*Par méthode j'entend des règles certaines et faciles dont la rigoureuse observation empêchera qu'on ne suppose jamais pour vrai ce qui est faux, et fera que, sans se consumer en effort inutiles, mais au contraire en augmentant graduellement sa science, l'esprit parvienne à la véritable connaissance de toutes les choses qu'il peut atteindre.*

Descart, Règles pour la direction de l'esprit

# 1

## Introduction: framework, motivations and method

### 1.1 The evolving Universe: the growth of structures and the role of interactions

The “luminous” Universe as observable today is made of structures spanning several orders of magnitude in scale-length: from galaxies, extending a few to tens of kpc<sup>1</sup>, to clusters of galaxies extending some Mpc, to large super-clusters and filamentary structures, which are distributed in the so-called “cosmic web” over hundreds of Mpc.

In the current standard picture, we live in an expanding Universe that originated 13.8 billions of years ago from a phase of extremely high density and temperature in the Big Bang. 300,000 years later, small fluctuations of the order of some  $10^{-5}$  present in the almost uniform density field, started growing due to gravitational instability. From a number of observations, starting in the 1930s (Zwicky 1937), we know that roughly 85% of the gravitational mass, that governs the growth and dynamical evolution of the structures, is made up of a weakly interacting, collisionless form of matter. Because of its properties, this matter has so far escaped detection through effects other than gravity, and has been dubbed “dark matter”. Theoretical and numerical work over the past decades has shown that primordial dark matter overdensities even-

---

<sup>1</sup>1 pc =  $3.086 \times 10^{18}$  cm

## 1 Introduction: framework, motivations and method

---

tually cease expanding with the universal flow (the “Hubble flow”), collapse and virialize; virialized “haloes” of small mass form first, and then grow by accretion and merging. Thus dark matter structure formation proceeds in a hierarchical “bottom-up” sequence.

Star formation has been occurring in the cores of the dark matter haloes as a consequence of cooling, fragmentation and collapse of the gas, thus giving rise to the galaxies we observe. The details of these processes are still uncertain and our knowledge of the relationship between dark and luminous matter is incomplete: this is the field of investigation of astronomers working on galaxy formation and evolution.

In the framework described above, a wide range of gravitational and dynamical interactions between haloes of different sizes and masses occurs during the evolution of galaxies and galaxy clusters. The most dramatic of them are the merger events, where two haloes of comparable mass and size merge into a single halo. Moreover, smaller haloes can be accreted by larger ones. Tidal forces can disrupt haloes creating extended structures in the vicinity of strong potential gradients, whenever the duration of the halo–potential interaction is comparable or larger than the internal dynamical time of the halo. Shorter interactions can be highly effective too, if they are repeated in time. This is often known as “galaxy harassment” (Richstone 1976; Moore et al. 1996) and occurs in galaxy clusters as a consequence of repeated high velocity encounters between galaxies: the interacting galaxies are repeatedly heated by the tidal forces, and a fraction of their mass (including some stars) eventually becomes loosely bound or even unbound.

As a consequence of all these dynamical interactions, galaxy structure and morphology are altered, and significant number of stars, from galaxies and merging protogalaxies, may spread into the space surrounding galaxies and into the intergalactic space within galaxy clusters. These stars give rise to what we will call “diffuse stellar components”.

### 1.2 Diffuse stellar components

How effective are dynamical interactions in removing stars from galaxies? How large is the amount of light contributed by the diffuse components? How diffuse are they? How are they distributed around galaxies? What kind of stellar populations are they made of? And, finally, what can we learn from them about galaxy and cluster formation? These are just some of the questions that concern astronomers working on the diffuse stellar components.

Theory and observations in this field have been rapidly evolving in recent

years, thanks to the development of new and more efficient observational techniques and to progress in cosmological and N-body simulations. In the next sections I will briefly review the historical background, the state-of-the-art observations and the current understanding of galaxy haloes and of the intracluster light from the point of view of galaxy and cluster formation.

### 1.2.1 The Galactic halo and galaxy haloes

#### 1.2.1.1 The Halo of the Milky Way

Despite representing less than 1% of the mass of the Milky Way, its stellar halo has been playing a crucial role in the understanding of the Milky Way as a galaxy since its discovery. In a series of works between 1918 and 1919, Harlow Shapley studied the globular clusters, spherical and compact aggregates of several thousands to millions of stars. He recognized that the distribution of globular clusters on the sky does not follow that of the Milky Way stars. Instead of concentrating in a narrow band across the sky, the globular clusters are distributed throughout the sky. Assuming a fixed intrinsic luminosity, he was also able to estimate their distance and to conclude that they are spherically distributed around a centre. This centre, according to his calculation, was located in the Milky Way plane, 15 kpc away from the Sun. With these observations Shapley not only identified for the first time the globular clusters as the most outstanding population of the Galactic halo, but also significantly changed the picture of the Milky Way emerging from Kapteyn's studies of the distribution of the disc stars. The Kapteyn's stellar disc, almost centred in the Sun, with a diameter of roughly 10 kpc, had to be replaced with a much larger disc, several tens of kpc wide, with a huge halo of globular clusters orbiting up to 100 kpc away from its centre. The Sun was located in a peripheral position.

In 1927 Lindblad proposed a kinematic model of the Milky Way in which different components have different degrees of flattening, as a consequence of the amount of rotational support. According to this idea, the highly flattened disc should be rapidly rotating (as Lindblad demonstrated), while the globular cluster system should be supported by disordered motions. Lindblad's kinetic theory was further developed by Jan Oort in the following years, and led to the first discovery of halo field stars. Oort observed that, although the majority of stars in the solar neighborhood, and the Sun itself, orbit in the disc plane around the galactic centre with a circular velocity of about  $220 \text{ km sec}^{-1}$ , there are a number of stars that do not follow the main "stream". They have high velocities relative to the Sun (so they were called *high-velocity stars*) and move along orbits that can be highly inclined with respect to the

## 1 Introduction: framework, motivations and method

---

disc. These are the kinematical signature of the halo objects, and those stars were the first individual halo stars discovered.

The next decades and especially the 1950s saw fundamental advances both on the observational and on the theoretical side, that made it possible to link Galactic structure, kinematics, chemistry and age into a unified evolutionary context. The identification of the main structural components of our Galaxy (the disc and the bulge, but not the halo!) with the analogous ones in external galaxies was achieved through Baade’s observations in 1944. The development of the theory of stellar evolution made it possible to date star clusters through the use of colour-magnitude diagrams (Sandage & Schwarzschild 1952). The advance of spectroscopy led to the discovery of element signatures in the stellar spectra that could be used to trace the “metal”<sup>2</sup> enrichment. The discovery by Roman (1954), that metal deficiency is associated with high-velocity stars, was the starting point of the fundamental work by Eggen, Lynden-Bell, & Sandage (1962). They discovered smooth correlations between the orbital eccentricity, the metal deficiency and the vertical velocity of stars in the solar neighborhood. Based on these correlations, they constructed a model where the Galaxy formed from the rapid free-fall collapse of a cloud of metal-poor, primordial gas in a density fluctuation that decoupled from the universal expansion flow. Stars formed during the collapse and reflect the chemical and kinematical state of the gas at the epoch when they formed. The first stars which formed have the lowest metal abundances and move on orbits that are nearly radial: these are the halo stars. As the collapse proceeded and dissipational processes took place, the gas settled in a flattened, rotationally supported disc. These stars have been continuously formed to the present day from the gas that has been progressively enriched.

Searle (1977) noted, however, that the Galactic globular clusters display a wide range of metal abundances, which are not correlated to their orbital parameters, and in particular to their distance from the Galactic Centre. Searle & Zinn (1978) therefore proposed a scenario in which the Galactic halo was assembled over a long period from independently evolved fragments with masses of  $\sim 10^8 M_{\odot}$ <sup>3</sup>. More recent observations indicate that not only is there a large spread in metallicity among the halo stars and the globular clusters, but also a large spread in age of 2–3 Gyr (Marquez & Schuster 1994), thus reinforcing

---

<sup>2</sup>Astronomers call metals all the elements with atomic number higher than 2. With a few exception, all these chemical elements are not primordial, but must be synthesized in stars or in supernova explosions. Thus, the presence of metals in stellar atmospheres is the signature of older stellar generations.

<sup>3</sup> $1 M_{\odot} = 1.989 \times 10^{33}$  g. Note that the total (stars plus dark matter) mass of the Milky Way is  $\sim 10^{12} M_{\odot}$ .

the hypothesis of inhomogeneous formation.

The parallel development of the hierarchical theory of galaxy formation (e.g. White & Rees 1978), in which galaxy formation proceeds through hierarchical aggregation of smaller units from the early universe, provided a robust cosmological basis for the Searl & Zinn view. Although a matter of intense debate for many years, this eventually led to the development of the current paradigm, that the assembly of the halo of the Milky Way occurred over a long period of time through an early collapse and the infall of a large number of small satellites and other debris.

During the last decade, wide-field, deep surveys of stars have produced evidence that the assembly process of the halo is still ongoing. Ibata, Gilmore, & Irwin (1994) discovered a dwarf spheroidal galaxy in Sagittarius, which shows very clear signs of strong tidal disturbance. Its present location at only 16 kpc from the center of the Galaxy and the relatively short orbital period ( $\sim 1$  Gyr) make it the best candidate for being disrupted and accreted, and thus for contributing to the stellar halo. Another clear example of ongoing tidal disruption is provided by the globular cluster Palomar 5 (Odenkirchen et al. 2001), and another phase-space correlation between a stellar stream and a dwarf galaxy in Canis Major has recently been reported by several authors. Moreover, it has been proposed that at least some of the globular clusters may be the dense nuclei of stripped dwarf spheroidal galaxies accreted by the Milky Way (this hypothesis is proposed, in particular, to explain the peculiar properties of the stellar population in  $\omega$  Centauri).

If the accretion scenario is correct, we should expect to find several hundreds of debris streams from disrupted satellites in the Galactic halo (e.g. Helmi & White 1999, and the “spaghetti project”, Fig. 1.1). However, their identification is far from easy, and their low density contrast often requires kinematical information in order to find “cold” structures in the 6-dimensional phase space. Forthcoming space missions, and particularly GAIA, are going to provide high accuracy astrometric and kinematical parameters for millions of stars within 20 kpc of the Sun, and therefore will be able to pinpoint several of these structures. The accompanying spectroscopic coverage will make metal abundances available too, and so will allow us to test the origin of the age/metallicity spread in the halo stars – could it be due to the individuality of the accreted satellites – and to trace the evolution of the halo back in time.

### 1.2.1.2 Stellar Haloes in external galaxies

The Milky Way is just one among billions of galaxies in the Universe. Although there is no reason to think that our Galaxy is special in any respect, a detailed knowledge of its properties or even of its evolutionary history cannot

## 1 Introduction: framework, motivations and method

---

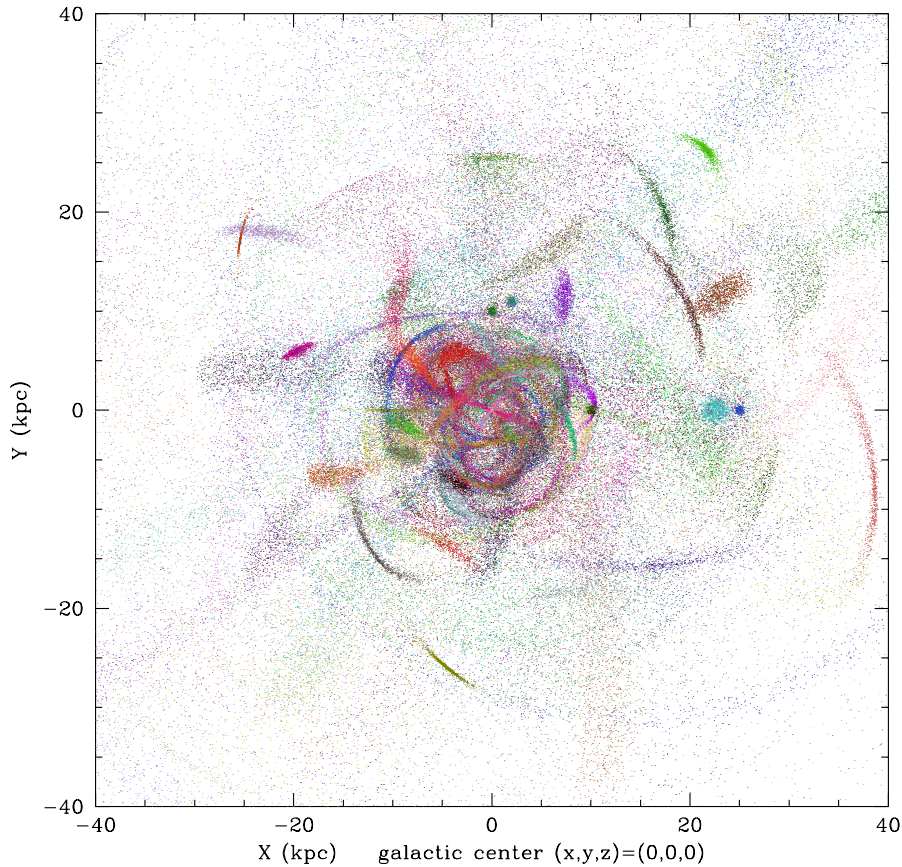


**Figure 1.1:** The superposition of many tidal streams in the Milky Way halo as expected from the numerical simulation of P. Harding, “The Spaghetti Project”

be generalized to the full variety of galaxies that populate the Universe. If we restrict our attention to disc galaxies, where a star-forming disc is the distinctive feature, we see a broad variety of morphologies: from bulgeless, low surface brightness discs (LSB galaxies), to highly structured spiral discs with little or no bulge (Sc), to spirals where a central bulge of old stars accounts for increasing fractions of the total luminosity (Sb and Sa). The first obvious question that can be raised is the following: do all these different morphological types have a stellar halo? And, moreover, are all the haloes produced in the same way?

## 1.2 Diffuse stellar components

---

From the distribution of halo stars in the Milky Way we know that the total luminosity of the halo is less than 1% of the total luminosity (e.g. Morrison 1993). However, since this luminosity is emitted over a very large area, that extends as far as  $\gtrsim 50$  kpc from the Galactic Centre, the resulting surface brightness is hundreds to thousand times fainter than that of the disc or of the bulge. At the solar radius, the Milky Way halo as seen from outside would have a surface brightness of  $27.7 \text{ mag arcsec}^{-2}$  in V, which is less than 1% of the surface brightness of the night sky. In order to be detected, this requires not only high sensitivity, but also that a number of instrumental effects be kept under tight control, as will be shown in a following section. It is no wonder, therefore, that very few detections of halo stellar emission have been obtained so far around external galaxies.

The most obvious target for studying the halo is our largest Local Group companion, the galaxy of Andromeda (M31). Given its relatively small distance of 780 kpc, its giant stars can be resolved and studied individually. Different groups in recent years have used red giant branch (RGB) stars in the halo of M31 to map its surface brightness and to study its metallicity distribution. A well established result is that, compared to the Milky Way, the metallicity of the halo of M31 is higher (0.3 vs. 0.05 in solar units, Durrell, Harris, & Pritchett 2004, and references therein). This indicates a substantial difference between the two haloes (an extended bulge has been invoked to explain the intermediate metallicity of M31 halo) and may reflect the accretion of more massive and more metal-rich satellites. Whatever the origin of this diversity, it clearly indicates that a large statistical sample of galaxies must be observed in order to gain an unbiased view of stellar haloes and of their role in the processes of galaxy formation.

Using wide field imaging, Rodrigo Ibata, Annette Ferguson, Michael Irwin, and collaborators (Ibata et al. 2001; Ferguson et al. 2002; Ibata et al. 2004) have studied the distribution of RGB stars in the halo of M31 out to 50 kpc along the minor axis, covering the entire surrounding region of sky. Interestingly, they found significant substructures that may originate from the tidal disruption of a dwarf spheroidal satellite. The discovery of the core of the remnant galaxy associated with the tidal structures would be the “smoking gun” proving the effectiveness of galaxy disruption as a mechanism of halo formation. Moreover it would provide invaluable clues on the properties of the stellar populations that eventually are spread into the halo.

On the other hand, analogous studies of RGB stars undertaken in the outskirts of the nearby late spiral (very small central bulge and highly structured spiral arms) M33 has produced very controversial results, some of them consistent with the absence of halo stars.

## 1 Introduction: framework, motivations and method

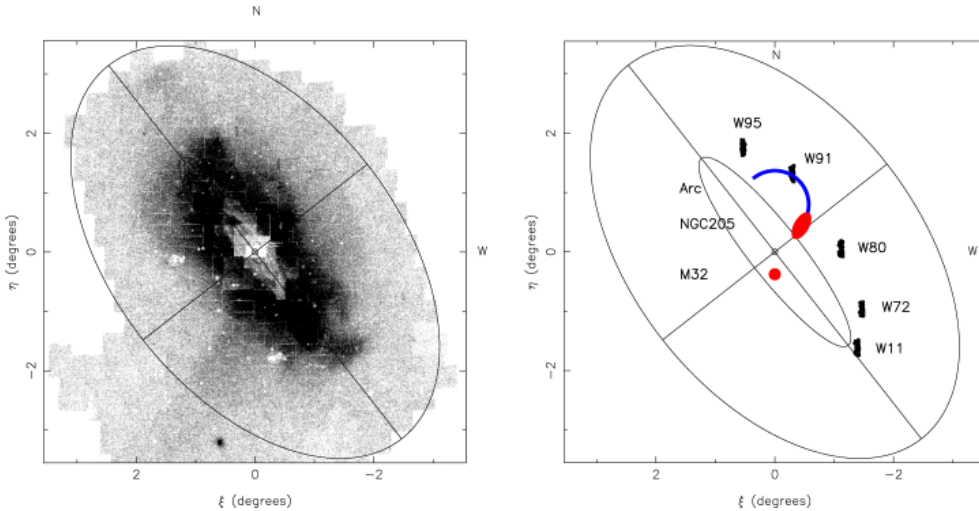


**Figure 1.2:** The distribution of old RGB stars in the outskirts of M31 (left panel) and its dynamical interpretation (on the right). The inner ellipse represents the optical extension of the disc. A number of substructures in the halo are clearly visible in the left panel. From Ibata et al. (2004).

The halo stars of more distant galaxies are not resolved, even with the highest resolution of the Hubble Space Telescope (0.03 arcseconds). The only way to study the halo of these galaxies is to measure their integrated surface brightness. Since the disc is much brighter than the halo, the ideal targets for this kind of study are galaxies which are seen edge-on. The disc then appears as a narrow band and the diffuse emission from the halo stars can be picked out as extra-planar light.

From what we know about the haloes of the Milky Way and of M31, the stellar populations that reside in the halo are old. Since old stars are cool and their emission peaks in the red/near-infrared part of the spectrum, most observations have concentrated on these bands. Early research on halo emission was also motivated by the search for the “dark component”, whose mass is responsible for the flat rotation curves of disc galaxies<sup>4</sup>. Although a number of cosmological arguments today disfavor this hypothesis, one possibility would have been that the halo is made up of a large number of cold sub-stellar objects, emitting mainly in the infrared. That is why, despite the higher surface

<sup>4</sup>If the light traced the mass at all radii, we should expect the rotational velocity of the disc as a function of radius to decrease at large distance, according to Kepler’s laws. What is observed instead is that the rotational velocity of the neutral hydrogen clouds attain a maximum and then stay constant out to several tens of kpc. A massive (unseen!) halo with  $\rho \propto r^{-2}$  is required in order to explain this.

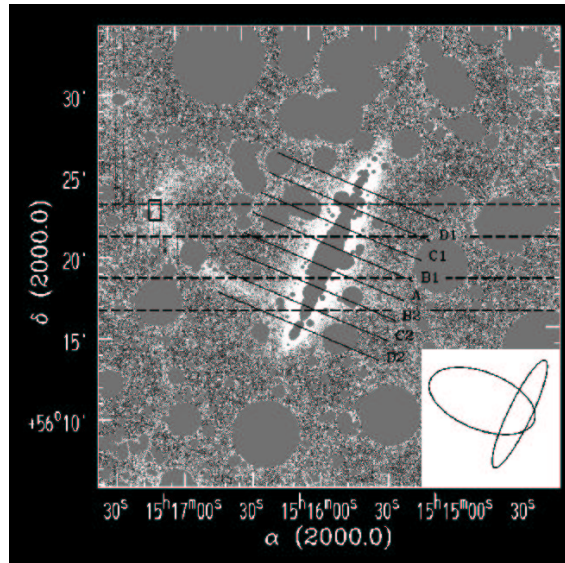


**Figure 1.3:** The low surface brightness emission from the halo of NGC 5907: The stellar ring almost perpendicular to the disc is apparent on the North-East side. From Zheng et al. (1999).

brightness of the sky in those bands, many observations have been made in the near infrared.

A detailed review of the observations and of the history of alternating detection and non-detection is beyond the scope of this introduction (see, however, Chap. 2.1 Zibetti, White, & Brinkmann 2004, for an exhaustive discussion). Nonetheless, it is worth noting the variety of observed halo properties and how deeply the technological improvement and the refinement in observational techniques has influenced our knowledge. The first claim of significant extraplanar emission dates back to 1994 (Sackett, Morrison, Harding, & Boroson 1994) and refers to NGC 5907, a disc galaxy at a distance of roughly 10 Mpc. After many controversial observations, it turned out that the emission is due mainly to an extended ring, probably resulting from the tidal disruption of a companion galaxy (Zheng et al. 1999, Fig. 1.3).

Since the late 1990s modern CCDs and the improved quality of flat-fielding techniques have allowed astronomers to assess the presence of red diffuse envelopes around a handful of edge-on discs. However, the different sensitivities reached in different observations have made it hard to understand:

- i) whether the presence of these envelopes is a common feature in disc galaxies;

## 1 Introduction: framework, motivations and method

---

- ii) whether one should talk about thick discs rather than genuine haloes, i.e. centrally concentrated spheroids.

Actually, the largest sample analyzed to date comprises 47 galaxies (Dalcanton & Bernstein 2002) and reaches a limit of  $\sim 28$  mag arcsec<sup>-2</sup> in R-band. Although it is quite clear that a red envelope is present in most of these galaxies, the sensitivity appears too low in order to understand whether this envelope may extend further out at the typical surface brightness expected for haloes and dispersed tidal features.

### 1.2.1.3 Haloes as fossil records of galaxy formation

Despite theoretical and observational progress in recent years, we still lack a reliable quantitative description of the galaxy formation processes. We know that a primordial dissipative collapse is required, as well as contemporary and subsequent mergers or accretion of smaller pieces. However, the relative importance of these two kinds of mechanism and the time sequence of the events are uncertain.

Although most of the baryonic mass resides in discs and bulges, the violent dissipative processes by which they have been shaped have almost completely erased the imprint of the primordial chemo-dynamical state of the matter. On the contrary, in the haloes dissipational mechanisms are almost absent and dynamical relaxation time-scales are comparable to the age of the Universe. Therefore, haloes can be regarded as fossil records of the epoch when the matter entered the galaxy. As demonstrated by the ongoing accretion of satellites by the Milky Way, however, it is actually simplistic to conclude that the halo reproduces the initial conditions of the galaxy assembly. In fact, much of the material may have been accreted at later stages, after having been pre-processed in small satellites.

In order to understand the origin of stellar haloes and the role they play in the process of galaxy formation, we need to combine the wealth of details coming from the study of the Milky Way halo with a statistical description of the halo properties for a large sample of disc galaxies, so that questions like the following can be answered:

- Is the morphology (presence of a bulge, gas richness, star forming activity) related to the presence and the properties of the halo? Do flat, bulgeless galaxies possess stellar haloes as well as early-type galaxies? Is the formation of the bulge related to the development of the outer halo?
- Does the luminosity, mean age and metallicity of the halo depend on the total mass of a galaxy? If so, how?

- What is the scale dependence of the halo properties? Are haloes self-similar with their parent galaxy, in the sense that galaxies of different sizes are essentially the same, provided that a simple rescaling is applied, as suggested by pure N-body simulations of dark matter haloes, or do baryonic processes (star formation, “feed back”<sup>5</sup>, gas cooling) set characteristic scale lengths?

### 1.2.2 The Intracluster Light

#### 1.2.2.1 Clusters of galaxies

The fact that galaxies are not uniformly distributed in the sky was already recognized toward the end of the 16th century. In 1781, Charles Messier noted that 16 of the first 91 “nebulae” of his catalog happen to lie in the small region of the sky at the north-western edge of the constellation of Virgo and overlapping Coma Berenices. William and John Herschel, in their catalogs, also found many of their “nebulae” concentrating there, and Alexander von Humboldt commented that one-third of all nebulae known in the mid-19th century are situated in one-eighth of the sky around Virgo. We now know that these concentrations of galaxies in Virgo and Coma Berenices are just two of the innumerable clusters of galaxies that populate the Universe, each of them including hundreds to thousands of galaxies.

Clusters are the largest virialized structures in the Universe. Their masses range from  $10^{13}$  to  $10^{15}M_{\odot}$ , roughly 10 to 1000 times the mass of the Milky Way. Their size is usually described in terms of  $R_{200}$ , that is the radius which encloses an average overdensity of matter of a factor 200 with respect to the average density of the Universe. This corresponds to the radius that a spherical top-hat overdensity would eventually reach once it is virialized in a homogeneous, expanding Universe. The density in the cluster cores is actually hundreds of times higher. This makes clusters an ideal laboratory to study the interactions between galaxies and between galaxies and the environment where they live.

#### 1.2.2.2 Interactions in galaxy clusters and the origin of the intracluster light

A galaxy moving within a cluster may experience many kinds of interaction. These can be divided into two gross categories: dynamical/gravitational in-

---

<sup>5</sup>Star formation activity is determined by the gravitational dynamics and by the hydrodynamics of the gaseous component. As the most massive stars come to the end of their life, they inject significant amounts of energy into the interstellar medium through powerful stellar winds and, mainly, supernova explosions.

## 1 Introduction: framework, motivations and method

---



**Figure 1.4:** The rich cluster of galaxies Abell 1689, imaged by the Advanced Camera for Surveys, on board of the Hubble Space Telescope. Credit: N. Benitez (JHU), T. Broadhurst (Hebrew Univ.), H. Ford (JHU), M. Clampin (STScI), G. Hartig (STScI), G. Illingworth (UCO/Lick), ACS Science Team, ESA, NASA

teractions and interactions with the hot ( $\sim 10^6$  K) gas that permeates the intracluster space. Although they are both extremely relevant to the evolution of galaxies, I will concentrate on the dynamical/gravitational interactions alone in the following. It is impossible here to review all the contributions to this field from the literature. Very schematically the relevant gravitational interactions can be summarized as follows:

- mergers or accretions;
- low velocity galaxy–galaxy encounters, that produce tidal distortion and tails;
- high velocity galaxy–galaxy encounters, that heat the internal dynamics of galaxies. Repeated high velocity encounters are known as “harassment”.
- interactions with the global gravitational potential of the cluster, producing a variety of effects, from tidal stirring, to tidal truncation of the galaxy density profile.

As already mentioned at the beginning of this chapter, all these processes and their interplay cause a significant number of stars to become unbound from

their parent galaxies and to end up orbiting freely in the cluster potential: they are sources of Intracluster Light (ICL). ICL might come also from stars formed *in situ* between galaxies.

The rate and effectiveness of these interactions depend critically on the dynamical properties of the cluster and on the internal mass distribution and dynamics of the galaxies involved. For example, as already shown by early numerical simulations (Toomre & Toomre 1972), discs are particularly fragile and can be easily disrupted by tidal forces.

The definition of “high” or “low” velocity encounter refers to the encounter velocity of the galaxies compared to the internal velocity dispersion of the stars within the galaxies. For a typical bright galaxy the internal dispersion is around some hundreds of km/s, whereas rich clusters have velocity dispersions of the order of 1,000 km/s. Low velocity galaxy–galaxy interactions are therefore quite rare in rich clusters, while they become more and more likely the lower the mass of the cluster is. The maximum rate is expected in small compact groups. High velocity encounters and tidal interactions with the cluster potential are the dynamically dominant effects in rich clusters.

The effects of close low velocity encounters and the evolution of stellar orbits for a galaxy in a fixed smooth potential can be reliably simulated with modern supercomputers, since high resolution is required for a limited number of particles representing the one or two galaxies involved. The effects of the “harassment” and of the clumpy potential in a rich cluster are much harder to predict, however, since these processes are effective over a very long time scale and depend strongly on the detailed mass distributions and internal dynamics of each individual galaxy. Further complications can be added including a realistic cosmological environment, with infall and mergers of subclusters, and the simultaneous evolution of the baryons (gas cooling, star formation, feed-back). Thus, modeling the distribution of stripped stars in a cluster of galaxies using simulations is extremely complicated. Although some attempts have been made in recent years by several groups (Napolitano et al. 2003; Murante et al. 2004; Willman et al. 2004; Sommer-Larsen, Romeo, & Portinari 2004), we are still far from having robust simulations that can be used to check the physical assumptions adopted against observation.

### 1.2.2.3 Observations of the Intracluster Light

The first discovery of diffuse stellar emission within a cluster of galaxies dates back to the 1951. In a paper on “The Coma cluster of galaxies”, Fritz Zwicky reported the discovery that “vast and often very irregular swarms of stars and other matter exist in the spaces between the conventional spiral, elliptical and irregular galaxies” (Zwicky 1951).

## 1 Introduction: framework, motivations and method

---

Although clearly visible in the densest regions of rich clusters, the intracluster starlight has typical very low surface brightness  $\gtrsim 26$  mag arcsec $^{-2}$  in the red bands. Advances in photographic techniques allowed several authors in the 1970s to detect very extended stellar haloes around the largest elliptical galaxies located in the centre of clusters (cD galaxies) and common envelopes permeating the whole cluster (e.g. Kormendy & Bahcall 1974). But it was only with the development of photoelectric photometry that the first reliable quantitative estimates of the amount and the distribution of intracluster stars could be made. Melnick, Hoessel, & White (1977) analyzed a strip across the Coma cluster and found that the intracluster light may contribute up to 25% of the total optical emission in the cluster.

With the advent of large panoramic CCD<sup>6</sup> detectors, capable of imaging several tens of square arcminutes with quantum efficiency  $\gtrsim 80\%$ , a new leap could be made in the observations of the ICL.

Although hampered by a number of technical difficulties, ICL surveys have been conducted during recent years by several groups (in particular Anthony Gonzalez and collaborators, and John Feldmeier and collaborators). Their main results may be summarized as follows:

- the ICL contributes roughly 20% of a cluster's luminosity;
- the amount of ICL correlates with the size of the cluster: massive clusters with large cDs tend to have relatively more ICL than the small ones;
- part of the ICL may be attributed to tidal structures, such as arcs, tails and streams, originating from recent disruption or stripping of galaxies in intense tidal fields (see Fig. 1.5).

Further contributions to the study of the intracluster stars, and, particularly, of their dynamics have come from the observation of the intracluster planetary nebulae (IPNae). Planetary nebulae mark the endpoint of stellar evolution for stars with masses between  $\sim 0.8$  and  $8 M_{\odot}$ . They are glowing shells of gas, which are ejected during the giant phase of the star. These shells are ionized by the ultraviolet radiation from the newly exposed, hot burning core. Because of their low density, they emit in many forbidden lines, among which the most important is [OIII]  $\lambda 4959/5007$ . Since most of the luminosity of the central star is emitted in this line, a comparison between the images taken in two narrow-band filters centred on the line and on a slightly offset wavelength (on-off) can easily pick out a planetary nebula, even in a crowded

---

<sup>6</sup>CCD stands for Charge-Coupled Device, and indicates an array of coupled semi-conductor photon detectors. The signal in each detector is read by shifting the charge of the photoelectrons along the line of detectors.

## 1.2 Diffuse stellar components

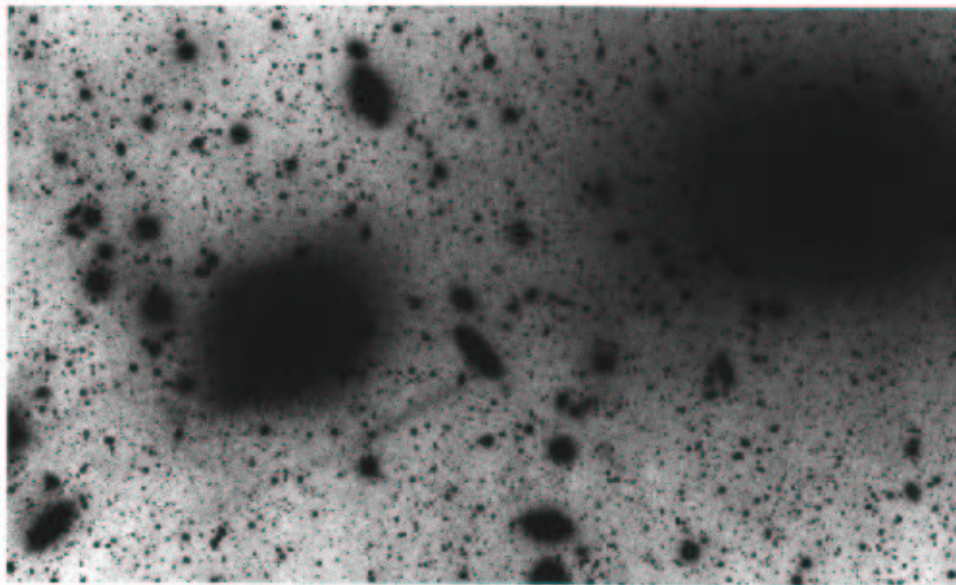
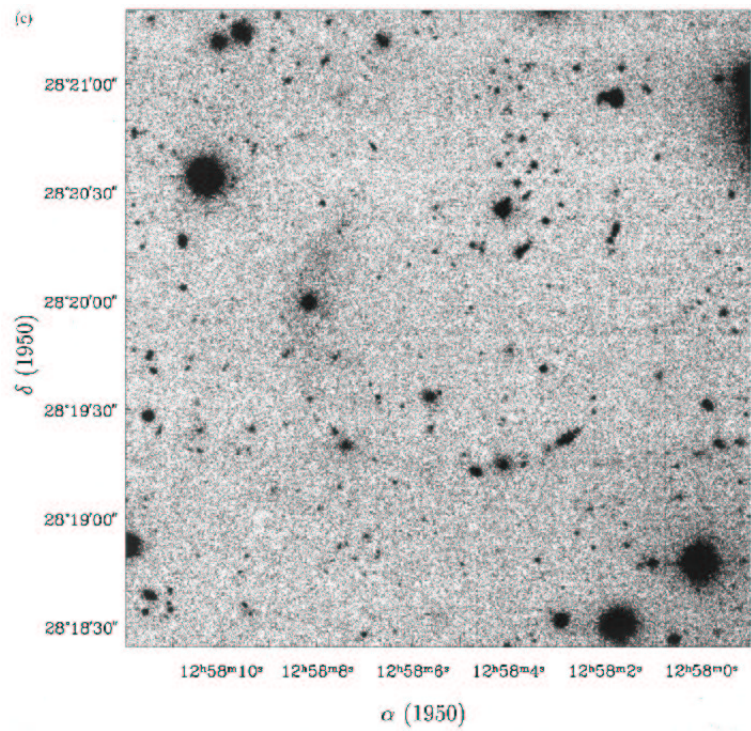


**Figure 1.5:** Two outstanding tidal structures in nearby clusters. Upper plate: an arc structure in Coma, from Trentham & Mobasher (1998). Lower plate: a 100 kpc long trail in Centaurus, from Calcáneo-Roldán et al. (2000).

## 1 Introduction: framework, motivations and method

---

field at distances up to 20 Mpc. Moreover, the emission line spectrum of PNae makes them a relatively easy spectroscopic target in order to measure their velocities.

Arnaboldi et al. (1996) reported for the first time observations of three PNae around the giant elliptical galaxy NGC 4406 (M86) in the Virgo cluster, which display high velocities relative to the galaxy and therefore can be interpreted as part of the intracluster stellar population. In the last years over three hundred IPNae have been observed (Feldmeier et al. 2004b) in the Virgo cluster, providing an independent estimate of the ICL amount of about 16% of the total luminosity. Future analysis of the distribution of these objects in position–velocity space will provide a valuable insight into the dynamical state of the intracluster stars and hence into their origin.

### 1.2.2.4 Intracluster Light: our state-of-the-art understanding

Observations have shown that a significant amount of starlight (around 20% of the total) is emitted by stars in the intergalactic space between galaxies in clusters. These stars are presumably unbound to any individual galaxy, being located far beyond their tidal radii. The unbound state of these intracluster stars is supported by the dynamics of a number of intracluster planetary nebulae.

The spectacular tidal structures observed in nearby clusters suggest a tidal and disruptive origin for many of the intracluster stars, as expected from theoretical arguments.

In the highly complex scenario of hierarchical structure formation, the development of an intracluster stellar population is influenced by a number of factors that can vary the effectiveness of the interactions mentioned above. The interplay of the many different stripping and disrupting mechanisms requires detailed numerical simulations in order to make careful comparison with the observations and hence obtain significant constraints on the assembly history of clusters and on the structural parameters of the dark matter haloes. However, the study of the ICL (amount, distribution, colours) in different environments, from the richest to the poorest clusters, from the deepest to the shallowest potential wells, from dynamically young clusters to the old ones, can provide some key information:

- where the ICL is preferentially formed within a cluster;
- when it is formed, whether during the early virialization phase or continuously during the history of the cluster;

### 1.3 Low Surface Brightness Photometry: the observational challenge

---

- how the cluster mass influences the formation of the ICL: whether the ICL is mostly produced in small groups via two-body encounters or in massive regular clusters via tidal stripping by the cluster potential (plus harassment);
- which galaxies are the main contributors of intracluster stars.

### 1.3 Low Surface Brightness Photometry: the observational challenge

As already stressed several times in previous sections, the observation of galaxy haloes and of the ICL is made difficult by the low surface brightness of these components. In typical ground-based observing conditions the surface brightness of the sky caused by the atmospheric glow is around  $20.5 \text{ mag arcsec}^{-2}$  in the red bands. Therefore, in order to measure a surface brightness of  $28 \text{ mag arcsec}^{-2}$  one must be able to measure fluxes with an accuracy better than 1/1,000.

Modern photometric measurements are made using Charge-Coupled Devices or CCDs for short. A thorough description of this kind of detector is beyond the scope of this introduction and I will only give a brief description, stressing the details which are relevant to measurement of low surface brightnesses.

An astronomical CCD, working in the optical regime, is essentially an array of semi-conductor detectors of photons, linked or coupled to each other. On photon arrival, valence band electrons in the semiconductor are excited to the conduction band and immediately stored in a capacitor. Applying an alternate voltage (“clock”) to the line of coupled detectors/capacitors it is possible to make the charge shift to an output amplifier and to “read” the signal. The CCD is located at the focal plane of the telescope camera, and each detector of the array integrates the flux at its specific position. The flux intensity in each detector is used as a picture element (pixel) in order to reconstruct the focal plane image.

A CCD image is therefore the result of the  $N$  measurements of the  $N$  pixels, each corresponding to a different detector, with slightly different noise properties and efficiency. These need to be known and calibrated in order to make photometric measurements possible. Moreover, one has to consider that the illumination of the CCD is, in general, inhomogeneous, due to the optical properties of the camera. Large scale variation of the illumination can be of the order of a few%, thus can easily mimic low surface brightness excesses.

## 1 Introduction: framework, motivations and method

---

Standard data reduction procedures are meant to subtract the electronic noise of each pixel, as estimated from *dark current* and *bias* images, and to correct all pixel intensities to a uniform effective (detector+telescope) response. This is done through the so called *flat field* correction. A uniformly illuminated field (usually the inner side of the dome or the sky at the twilight) is imaged, so that the relative response of each pixel can be determined. Typical flat field accuracy is around 1% or slightly less, and is therefore inadequate for measuring low surface brightnesses.

In order to improve the homogeneity of the CCD response, a drift scan technique may be adopted (Gonzalez et al. 2000). In this particular acquisition mode, the CCD does not stare at the same field during the exposure time, but drifts. The CCD columns are aligned along the drift direction and the clock signal that makes the charge shift is synchronous with the drift. The image is thus read while it is being integrated, and the intensity in each image pixel results from the signal integrated in all the CCD elements of the corresponding column. The effective response is averaged along the columns, and flat field variations are limited to the columns, thus making the response intrinsically more homogeneous.

Another strategy adopted by other authors consists instead in combining a large number of sky exposures to obtain “super sky flats”. Severe clipping algorithms are applied in order to exclude sky sources and cosmic rays. In both cases, the effective response can be determined with accuracy of some 0.1%.

Unfortunately target galaxies and clusters are not isolated on the sky, but are surrounded by and superposed to many foreground and background sources, whose brightness can be thousands of times higher than the diffuse light that one wants to measure. Because of the diffraction in the optical system and of the effects of differential refraction in the atmospheric layers (the so-called “seeing”), the images of point-like sources are spread over large areas, according to the Point Spread Function (PSF). Although the core of typical PSFs is well described by a Gaussian with FWHM varying from 0.4 to a few arcseconds (depending on the telescope and the seeing of the observing site), the far wings of the PSF are usually much flatter and more extended. The flux of very bright stars, therefore, can be spread several arcseconds away, and significantly affect measurements of the diffuse light. Careful modeling and subtraction of the PSF is thus required, but is extremely hard to achieve, since roughly four orders of magnitude in intensity must be covered. Subtler, but still relevant contaminations can arise from the light that undergoes internal reflections in the camera and scattering at the numerous optical interfaces (including the anti-reflection layers, which cover the optical pieces

and the CCD surface).

All these effects are difficult to model to high accuracy and the residuals from their subtraction are included into the background fluctuations. Only the lowest order harmonics (large scale gradients) of these fluctuations can be removed by fitting smooth polynomials to the background intensity distribution. Measurements of the diffuse light inevitably include the residuals from this subtraction, thus increasing the error budget.

### 1.3.1 Statistics against photometric limitations

The observational conditions for a galaxy or a cluster cannot be changed: in fact, there is no way to remove bright foreground stars or large nearby galaxies from the field of view we are interested in! Nevertheless, if the goal is to describe the statistical properties of a certain class of objects, one can think of combining the observations of a large number of objects in such a way that the errors on the individual observations cancel out, leaving the average quantity unbiased. For the specific purpose of measuring the diffuse light, this can be achieved by stacking several hundred images, where bright polluting sources can be masked, and for which one can reasonably assume that the contaminant sources are uniformly distributed. Provided that the targets are positioned in different parts of the field of view of the camera, the residual inhomogeneities of the flat-field corrections are averaged out too. This method requires a huge amount of homogeneous imaging data for the class of objects one aims at studying. Such a database has only recently become available to the astronomical community thanks to the Sloan Digital Sky Survey, as I will briefly describe in the next section.

## 1.4 The Sloan Digital Sky Survey

The Sloan Digital Sky Survey (SDSS) is probably the most ambitious large scale optical survey of the sky ever undertaken. It is a joint project of The University of Chicago, Fermilab, the Institute for Advanced Study, the Japan Participation Group, The Johns Hopkins University, the Los Alamos National Laboratory, the Max-Planck-Institute for Astronomy (MPIA), the Max-Planck-Institute for Astrophysics (MPA), New Mexico State University, University of Pittsburgh, Princeton University, the United States Naval Observatory, and the University of Washington.

Started in 2000, the SDSS aims at covering by the end of 2005 one quarter of the sky with five-band imaging and medium resolution spectroscopy (York et al. 2000). The survey area is centered on the north Galactic cap and includes

## 1 Introduction: framework, motivations and method

---

in addition three stripes in the southern Galactic hemisphere (one of those, the equatorial stripe, is being observed repeatedly to study variable objects and obtain deeper detections).

The main goal of the SDSS is to produce the most complete map of the Universe ever realized, up to a redshift of 0.4. Its characteristics, however, make the SDSS an invaluable goldmine of data for most astronomical branches, dealing with the properties of galaxies and galaxy clusters, the distribution and properties of quasars up to high redshift, the stellar structure of the Milky Way, the study of stellar populations and rare stars, and variable phenomena like stellar variability and moving objects in the Solar System.

Imaging data are acquired during good seeing, moonless nights at the dedicated 2.5 m f/5 modified Ritchey-Chrétien wide-field altitude-azimuth telescope, located at the Apache Point Observatory (APO), Sunspot, New Mexico. The photometric/astrometric camera is attached at the Cassegrain focus and images the sky in drift scan mode, along great circles. The corrected 3 degree field is covered with a mosaic of 30  $2048 \times 2048$  Tektronix CCDs, 6 for each photometric band. The five pass-band filters cover the spectral region from the near ultra-violet ( $u$ -band,  $3551\text{\AA}$ ) to the near-infrared ( $z$ -band,  $8931\text{\AA}$ ), passing through the visible wavelengths ( $g$ -,  $r$ -, and  $i$ -bands at  $\lambda = 4686, 6165, 7481 \text{\AA}$  respectively). The pixel scale is  $0.396 \text{ arcsec/pix}$ , and the equivalent exposure time per pixel is 54.1 seconds.

The reduction of the imaging data relies on automatic pipelines, which perform the standard reduction and calibration procedures. The photometric analysis includes the sky subtraction, the deblending of overlapping sources, the extraction of the catalogue of objects and the measurement of their relevant photometric properties (fluxes, characteristic radii, shape of the surface brightness profile, momenta of the light distribution). These tasks are performed by the photo pipeline, developed by Robert Lupton (Lupton et al. 2001).

The spectroscopic survey aims at observing complete samples of the three following categories of objects (primary targets):

- Galaxies, selected to be brighter than  $r=17.77 \text{ mag}$ , using Petrosian magnitudes;
- Luminous Red Galaxies, selected by their color and magnitude to be a roughly volume-limited sample of the most luminous red ellipticals to  $z \approx 0.45$ ; and
- Quasars, selected by their distinctive colors in the SDSS photometric system, and by radio detection in the FIRST survey catalog.

A total of about one million of spectra of galaxies and 150,000 spectra of quasars will be observed by the end of the survey in 2005.

The spectra are obtained with two double (red plus blue arms) fiber-fed spectrographs, permanently mounted on the image rotator of the APO telescope. The telescope can be switched from the imaging to the spectroscopic mode by substituting the camera with a fiber plug plate. The plate is drilled according to the astrometric coordinates obtained from the imaging data, for all the primary targets. A number of fibers is allocated to empty sky positions in order to measure the sky background emission. The remaining plug positions left free are assigned to secondary targets, such as X-ray sources, cool stars and white dwarfs.

The spectra are taken whenever the photometric requirements are not fulfilled (provided that the sky is clean). The average spectral resolution of the SDSS spectrographs is  $\frac{\lambda}{\Delta\lambda} = 2000$ , and the covered wavelengths range from 3800 to 9200 Å.

Automatic pipelines are devoted at the reduction of the spectra, which include the standard wavelength calibration and the sky subtraction. The redshift of each spectrum is obtained independently using emission lines and absorption features. In the first case, positive peaks in the spectrum are identified and their positions are compared to those of known emission lines of galaxies and quasars. For the absorption, a cross-correlation between the observed spectrum and high signal-to-noise templates is performed. The most reliable redshift estimate is given as fiducial redshift of the object. The comparison with template spectra of different astronomical sources allows the classification of the observed object into different spectral classes (star, galaxy, QSO, high-redshift QSO).

At the time of writing 97% of the imaging has been completed, corresponding to 8216 square degrees, and 62% of the spectroscopic survey. 3324 square degrees of imaging (2627 square degrees covered by spectra) are already available to the community as the “Second Data Release”. The enormous impact of the SDSS on the development of astronomy is witnessed by the almost 600 refereed papers that mention it in their abstract.

## 1.5 The thesis

The goal of this thesis is to provide for the first time a statistical description of the diffuse stellar components around disc galaxies and in galaxy clusters. Many of the questions proposed in the previous sections will be addressed. With this work I aim at providing a quantitative assessment of the frequency,

## 1 Introduction: framework, motivations and method

---

distribution and stellar populations (as derived from optical colours) of the stellar haloes around disc galaxies, paying particular attention to the dependence of these properties on the global luminosity of the galaxies. For the intracluster light, the objective is to measure its surface brightness profile and its optical colours out to unprecedentedly large clustercentric distances and to compare them to those of the cluster galaxies. Subsamples of clusters with different masses, richness and luminosity of the first ranked galaxy will be studied and compared, in order to derive clues to the mechanisms that lead to the formation of the unbound stellar population and to understand how their effectiveness depends of the global cluster properties and evolutionary history.

As anticipated above, instead of obtaining exceedingly deep images of the individual targets, the strategy adopted in this study is statistical and consists in stacking a large number of images of targets, homogeneously selected from the SDSS.

The large number of images utilized not only enhances the S/N per pixel, but also makes it possible to efficiently remove the spurious signal contributed by polluting sources and possible instrumental anomalies. In fact, the large statistical basis allows to mask out stars and other bright sources in a very conservative way, avoiding their far wings. In addition, the fact, that the targets are observed with different fore- and back-grounds and lie in different regions of the image frame, produces an almost uniform background of contaminants in the stacked images, which can be easily removed.

In order to stack the images of the targets, they must be rescaled to the same size and photometric intensity scale. The latter can be easily recovered once the photometric calibration, the Galactic extinction and the redshift (when cosmological dimming<sup>7</sup> is not negligible) are known. The size rescaling is much more problematic, since the apparent size of an extragalactic object depends both on its distance and on its intrinsic properties. The proper physical size or different apparent characteristic scale-lengths can be used, in principle, to rescale the targets. In this work the most robust size estimators have been adopted, that is the exponential scale-length for the disc galaxies and the proper metric size for the clusters, and the validity of this choice has been checked using more homogeneous subsamples.

The construction of the masks for all the sources that must be excluded from the stacking has been accomplished combining different strategies, which comprise image filtering and smoothing, SB thresholding, source deblending, mask growing, superposition of large patches for identified bright stars. The pop-

---

<sup>7</sup>The surface brightness of a source decreases by a factor  $(1+z)^4$  due to the expansion of the Universe

ular SExtractor source extractor code (Bertin & Arnouts 1996) has been largely utilized in this task, but many original contributions to elaborate the masks and exclude sources detected by the SDSS `photo` pipeline have been implemented too.

In this thesis, the images of more than 1,000 edge-on disc galaxies and roughly 700 clusters of galaxies, observed by the SDSS in the optical passbands, have been analyzed, processed and stacked in order to measure SBs as faint as  $30 \text{ mag arcsec}^{-2}$ .

Data from the SDSS database and from different in-house pipelines have been combined. The huge amount of data analyzed and processed has required a big effort to develop fast and efficient methods and procedures, that can process more than 10 GB of raw imaging data into the final stacked image in less than 24 hours running on a single commercial personal computer. Most of the image processing software has been developed in the IRAF environment. Python has been largely utilized as an interface to the SDSS database query tools.

A great effort have been devoted to the development of the surface photometry software. Given the special features of the signal that had to be measured, many pieces of original code in C have had to be developed in order to apply the non-standard methods of background and error estimation, that will be thoroughly described in the following chapters.

The thesis is organized as follows. Chapter 2 is dedicated to the stellar haloes of disc galaxies. In the first part I report the analysis of the stacking of 1047 edge-on disc galaxies as published in Zibetti, White, & Brinkmann (2004): the stacking technique, here utilized for the first time, has allowed us to detect the ubiquitous presence of luminous haloes around disc galaxies. The average shape and surface brightness profile of these haloes have been measured out to 10 exponential disc scale-lengths, at the level of  $31 \text{ mag arcsec}^{-2}$  in the SDSS *r*-band. Multi-band data have pointed out anomalous colours, whose origin has not yet been clarified. In the second part of Chapter 2, the deepest exposure of the Hubble Space Telescope, the Hubble Ultra Deep Field, published in March 2004, has been used to study the halo of an edge-on disc galaxy at  $z \sim 0.3$  lying in its field of view. This study has been published in Zibetti & Ferguson (2004). The results from the previous stacking have been spectacularly confirmed on this single galaxy, thus validating the method and raising new questions on the origin of the anomalous colours of the halo emission.

The study of the Intracluster Light from the stacking of a sample of  $\sim 700$  clusters of galaxies between  $z = 0.2$  and  $0.3$  is reported in Chapter 3: for

## **1 Introduction: framework, motivations and method**

---

the first time the amount and the surface brightness profile of the ICL have been assessed on a statistical sample and extended to cluster-centric distances of roughly 700 kpc. This chapter reproduces the paper by Zibetti, White, Schneider & Brinkmann, submitted to MNRAS.

In Chapter 4 I will summarize the main results of this thesis and present an outlook on further developments of this research, and on the possibility of applying the stacking technique to other fields where the “statistical photometry” may be of great relevance.

## References

- Arnaboldi, M., et al. 1996, *ApJ*, 472, 145
- Bertin, E. & Arnouts, S. 1996, *A&AS*, 117, 393
- Calcáneo-Roldán, C., Moore, B., Bland-Hawthorn, J., Malin, D., & Sadler, E. M. 2000, *MNRAS*, 314, 324
- Dalcanton, J. J. & Bernstein, R. A. 2002, *AJ*, 124, 1328
- Durrell, P. R., Harris, W. E., & Pritchett, C. J. 2004, *AJ*, 128, 260
- Eggen, O. J., Lynden-Bell, D., & Sandage, A. R. 1962, *ApJ*, 136, 748
- Feldmeier, J., Ciardullo, R., Jacoby, G., & Durrell, P. 2004, *ArXiv Astrophysics e-prints*, astro-ph/0407274
- Ferguson, A. M. N., Irwin, M. J., Ibata, R. A., Lewis, G. F., & Tanvir, N. R. 2002, *AJ*, 124, 1452
- Gonzalez, A. H., Zabludoff, A. I., Zaritsky, D., & Dalcanton, J. J. 2000, *ApJ*, 536, 561
- Helmi, A. & White, S. D. M. 1999, *MNRAS*, 307, 495
- Ibata, R. A., Gilmore, G., & Irwin, M. J. 1994, *Nature*, 370, 194
- Ibata, R., Irwin, M.,
- Ibata, R., Chapman, S., Ferguson, A. M. N., Irwin, M., Lewis, G., & McConnachie, A. 2004, *MNRAS*, 351, 117
- Kormendy, J. & Bahcall, J. N. 1974, *AJ*, 79, 671
- Lewis, G., Ferguson, A. M. N., & Tanvir, N. 2001, *Nature*, 412, 49
- Lupton, R. H., Gunn, J. E., Ivezić, Z., Knapp, G. R., Kent, S., & Yasuda, N. 2001, *ASP Conf. Ser.* 238: *Astronomical Data Analysis Software and Systems X*, 10, 269

## References

---

- Marquez, A. & Schuster, W. J. 1994, *A&AS*, 108, 341
- Melnick, J., Hoessel, J., & White, S. D. M. 1977, *MNRAS*, 180, 207
- Moore, B., Katz, N., Lake, G., Dressler, A., & Oemler, A. 1996, *Nature*, 379, 613
- Morrison, H. L. 1993, *AJ*, 106, 578
- Murante, G., et al. 2004, *ApJ*, 607, L83
- Napolitano, N. R., et al. 2003, *ApJ*, 594, 172
- Odenkirchen, M., et al. 2001, *ApJ*, 548, L165
- Richstone, D. O. 1976, *ApJ*, 204, 642
- Roman, N. G. 1954, *AJ*, 59, 307
- Sackett, P. D., Morrison, H. L., Harding, P., & Boroson, T. A. 1994, *Nature*, 370, 441
- Sandage, A. R. & Schwarzschild, M. 1952, *ApJ*, 116, 463
- Searle, L. 1977, *Evolution of Galaxies and Stellar Populations*, 219
- Searle, L. & Zinn, R. 1978, *ApJ*, 225, 357
- Sommer-Larsen, J., Romeo, A. D., & Portinari, L. 2004, *ArXiv Astrophysics e-prints*, astro-ph/0403282
- Toomre, A. & Toomre, J. 1972, *ApJ*, 178, 623
- Trentham, N. & Mobasher, B. 1998, *MNRAS*, 293, 53
- White, S. D. M. & Rees, M. J. 1978, *MNRAS*, 183, 341
- Willman, B., Governato, F., Wadsley, J., & Quinn, T. 2004, *ArXiv Astrophysics e-prints*, astro-ph/0405094
- York, D. G., et al. 2000, *AJ*, 120, 1579
- Zheng, Z., et al. 1999, *AJ*, 117, 2757
- Zibetti, S. & Ferguson, A. M. N. 2004, *MNRAS*, 352, L6
- Zibetti, S., White, S. D. M., & Brinkmann, J. 2004, *MNRAS*, 347, 556
- Zwicky, F. 1937, *ApJ*, 86, 217
- Zwicky, F. 1951, *PASP*, 63, 61

*Ma non però doviamo, per quel che io stimo, distorci totalmente dalle contemplazioni delle cose, ancor che lontanissime da noi, se già non avessimo prima determinato, esser ottima risoluzione il posporre ogni atto specolativo a tutte le altre nostre occupazioni.*

Galileo Galilei, Terza lettera del Sig. Galileo Galilei al Sig. Marco Velsari delle macchie solari, 1612

# 2

## The stellar halo of disc galaxies

### 2.1 Haloes around edge-on disk galaxies in the Sloan Digital Sky Survey

Zibetti, S., White, S.D.M., Brinkmann, J., 2004, MNRAS, **347**, 556

#### Abstract

We present a statistical analysis of halo emission for a sample of 1047 edge-on disk galaxies imaged in five bands by the Sloan Digital Sky Survey (SDSS). Stacking the homogeneously rescaled images of the galaxies, we can measure surface brightnesses as deep as  $\mu_r \sim 31$  mag arcsec<sup>-2</sup>. The results strongly support the almost ubiquitous presence of stellar halos around disk galaxies, whose spatial distribution is well described by a power-law  $\rho \propto r^{-3}$ , in a moderately flattened spheroid ( $c/a \sim 0.6$ ). The colour estimates in  $g-r$  and  $r-i$ , although uncertain, give a clear indication for extremely red stellar populations, hinting at old ages and/or non-negligible metal enrichment. These results support the idea of halos being assembled via early merging of satellite galaxies.

#### keywords:

galaxies: halos, galaxies: structure, galaxies: photometry, galaxies: spiral

#### 2.1.1 Introduction

The most commonly accepted paradigm for the formation of structure in the universe, ranging from galaxies to clusters and superclusters of galaxies, pre-

## 2 The stellar halo of disc galaxies

---

dicts that they are assembled via the hierarchical clustering of dark matter (DM) halos, in the framework of the so called  $\Lambda$ CDM cosmology. Although these models have been very successful in describing large scale structure and much recent progress has been made in understanding the processes behind the assembly of individual galaxies through numerical simulations (e.g. Navarro & White 1994; Sommer-Larsen, Gelato & Vedel 1999; Navarro & Steinmetz 2000; Scannapieco & Tissera 2003), semi-analytic modelling (e.g. Kauffmann, White & Guiderdoni 1993; Baugh, Cole & Frenk 1996; Somerville & Primack 1999), and their combination (e.g. Kauffmann, Nusser & Steinmetz 1997; Kauffmann et al. 1999; Benson et al. 2000; Springel et al. 2001), much work is still needed.

The study of the stellar halos of disk galaxies, such as our own Milky Way (MW), can give a substantial contribution in this field. From many studies (for a review see e.g. Majewski 1993), it is known that the MW halo is populated by old, metal-poor stars, whose origin is debated. They may have formed in the early stages of the dissipational collapse of the gas in the proto-galactic DM halo. Alternatively they may have been accreted through the stripping of stars from satellite galaxies. Evidence that this process plays an important role in building up the stellar population of the halo, has come from the Sagittarius dSph (Ibata, Gilmore & Irwin 1994), a low-latitude halo stream found in the Sloan Digital Sky Survey (hereafter SDSS, Yanny et al. 2003; Ibata et al. 2003), the ongoing disruption process of the Palomar 5 globular cluster (Odenkirchen et al. 2002), and the detection of streams in local high velocity stars (Helmi et al. 1999). How much of the halo light and mass must be ascribed to this kind of interactions and how common they were in the past is still unclear.

In order to answer these questions in a more general context, the extension of the observations to a statistical sample of external galaxies is required. Unfortunately the surface brightness contributed by a stellar halo similar to the one in the MW is typically 7 to 10 magnitudes fainter than the central parts of the other galactic components (disk, bulge) and than the sky. At present day, observations of the halo are available only for a handful nearby galaxies and provide varying results. Recent work by Ferguson et al. (2002) has demonstrated the presence of substructure in the moderately metal-enriched stellar halo of M31, that is likely to be the relic of the disruption of one or more small companion galaxy. The search for halos in more distant galaxies, for which stars belonging to different components cannot be resolved, has been focused on edge-on disks, because of the much lower contamination of the halo by the projected disk stars. Problems with flat fielding, scattered light from other background and foreground sources, and extended PSF wings make it extremely difficult to obtain reliable photometry down to 29-30 mag arcsec<sup>-2</sup>,

## 2.1 Haloes around edge-on disk galaxies in the Sloan Digital Sky Survey

---

as required in order to characterise galactic halos. After the first detection of halo around NGC 5907 claimed by Sackett et al. (1994), many controversial results have followed. The latest and deepest observations of this galaxy (see e.g. Zheng et al. 1999) strongly support the extraplanar emission being instead a ring which results from tidal disruption of a satellite galaxy. In the most complete study so far, (but see Sec. 2.1.5 for a more exhaustive review of recent results in the literature), the deep observations of a sample of 47 edge-on galaxies, by Dalcanton & Bernstein (2002), provide evidence for the ubiquitous presence of red envelopes around disk galaxies, which the authors attribute to an old, moderately metal-enriched, thick disk structure.

In this paper we present the results from the statistical study of halo emission from a sample of more than 1000 edge-on disk galaxies imaged by the Sloan Digital Sky Survey (SDSS, York et al. 2000). The SDSS is imaging about a quarter of the sky in the  $u$ ,  $g$ ,  $r$ ,  $i$ , and  $z$  bands, with 54 sec drift scan exposures at the dedicated 2.5 m Apache Point Observatory telescope (Fukugita et al. 1996; Gunn et al. 1998; Hogg et al. 2001; Smith et al. 2002; Pier et al. 2003), reaching  $\sim 25$  mag arcsec $^{-2}$  at  $S/N \sim 1$  for a single pixel. In order to reach a surface brightness as low as 29 mag arcsec $^{-2}$ , we adopt a stacking technique, in which we combine the images of all the galaxies. First, the images must be geometrically transformed in order to make the galaxies superposable. Other external sources must then be masked. Finally, the count statistics of each pixel is considered and a suitable estimator is chosen to represent the distribution. In this way it is possible not only to increase the  $S/N$  by a factor  $\sim \sqrt{1000}$ , but also to remove statistically the major sources of contamination for deep photometry of individual objects, namely foreground and background sources, inhomogeneities in the flat field and light scattered inside the camera.

The paper is organised as follows: the sample is described in Sec. 2.1.2; in Sec. 2.1.3 we describe the image processing and the stacking procedure. The results are analysed in Sec. 2.1.4, paying particular attention to the noise properties of the resulting images and to the possible sources of error and of bias. A discussion, including a comprehensive comparison with previous results in the literature and the possible implications for galaxy formation, is given in Sec. 2.1.5. A summary and the conclusions of this work are reported in Sec. 2.1.6.

### 2.1.2 The Sample

As of April 2002 the SDSS has covered  $\sim 2000$  square degrees both in 5-band imaging and spectroscopy. Blanton et al. (2002) have selected a sample of

## 2 The stellar halo of disc galaxies

---

galaxies from the Main Galaxy Sample (Strauss et al. 2002), also known as ‘Large-Scale Structure Sample 10’ (LSS10), including all sources with average surface brightness within the Petrosian<sup>1</sup> radius in  $r$  band  $\mu_r < 17.77$ , that have been successfully targeted by the spectroscopic observations (see Blanton et al. 2003, for details about the ‘tiling’ algorithm). We refer the reader to Blanton et al. (2002) for the details of the sample and the regions of the sky covered.

For the purposes of this work we selected a subsample of edge-on galaxies from the LSS10 requiring the following conditions to be satisfied:

- Petrosian magnitude ( $Pmag$ ) successfully measured at least in the three most sensitive SDSS pass-bands, namely the  $g$ ,  $r$ , and  $i$  band;
- $Pmag_i \leq 17.5$ ;
- isophotal semi-major axis<sup>2</sup>  $a > 10$  arcsec in  $i$  band;
- isophotal axis ratio  $b/a \leq 0.25$  in  $g$ ,  $r$  and  $i$  band.

Images of the 1221 selected galaxies were inspected by eye in order to prune from the sample objects that are unsuitable for stacking. First of all we discarded a few percent of the galaxies whose axis ratios had been clearly underestimated due to some failure in the SDSS PHOTO reduction pipeline. Galaxies showing evidence of interaction with nearby companions, warps or other irregularities were rejected. The absence of nearby bright sources contaminating the background was required as well. The resulting sample is composed of 1047 galaxies, ranging from  $-22.5$  to  $-16.0$   $i$ -band absolute Petrosian magnitude, in units of  $\text{mag} + 5 \log h$ . The redshift distribution of the sample peaks at  $z \sim 0.05$  with a standard deviation of 0.035. Typical physical dimensions range from  $\sim 1$  to  $\sim 25$   $\text{kpc } h^{-1}$  (Petrosian radius in the  $i$  band), with a median value of  $7.4$   $\text{kpc } h^{-1}$ . A summary of the sample properties is reported in Fig. 2.1. Eye inspection of the single galaxies confirms that our sample is dominated by late-type disk galaxies, with at most a few per cents of Sb-c or Sb. Most of the galaxies appear to be almost bulge-free and the the remainder have quite small ‘classical’ bulges.

---

<sup>1</sup>Petrosian (1976) defines the Petrosian radius as the radius at which the surface brightness equals a given fraction of the average surface brightness inside that radius. The Petrosian flux (and hence the magnitude) is defined as the flux inside a certain number of Petrosian radii. See Stoughton et al. (2002) for the full description of the procedure adopted in the SDSS data reduction and the actual parameters.

<sup>2</sup>the SDSS reduction pipeline PHOTO (Lupton et al. 2001) provides an elliptical fit of the  $25.0$   $\text{mag arcsec}^{-2}$  isophote parametrised by the semi-axes  $a$  and  $b$

## 2.1 Haloes around edge-on disk galaxies in the Sloan Digital Sky Survey

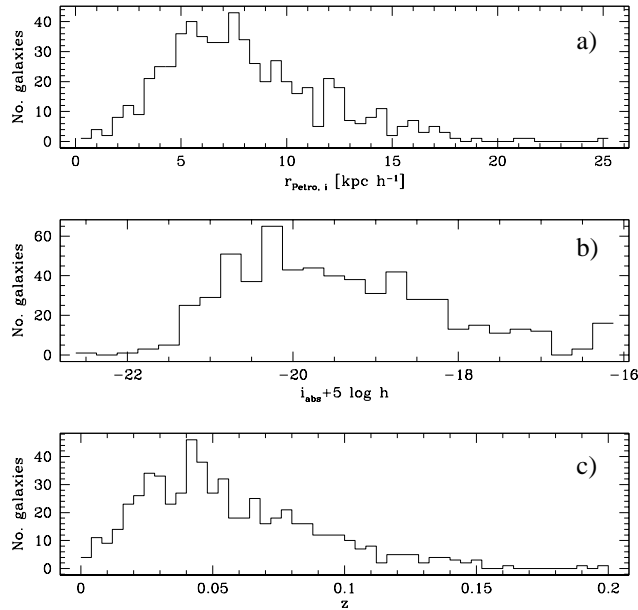


**Figure 2.1:** Distributions of the sample galaxies in Petrosian radius (panel a), absolute  $i$  band magnitude (panel b), and redshift (panel c).

### 2.1.3 The image stacking

#### 2.1.3.1 The image pre-processing

The raw SDSS imaging data is available as  $2048 \times 1489$  pixel<sup>2</sup> ( $13.5 \times 9.8$  arcmin<sup>2</sup>) bias subtracted and flat-fielded ‘corrected frames’. Using SExtractor v2.2.2 (Bertin & Arnouts 1996) we accurately determined the centre and the position angle of the major axis for each galaxy. From the segmentation image output by SExtractor we obtain a mask for all the sources in each field detected with  $S/N \geq 1$ . The background level for each galaxy was determined as the mode of the pixel count distribution in an annulus with inner radius  $3 \times a_{\text{iso}, i}$  and outer radius  $6 \times a_{\text{iso}, i}$  (where  $a_{\text{iso}, i}$  is the isophotal major semi-axis at 25.0 mag arcsec<sup>-2</sup> in  $i$ -band). This background was then subtracted from each image.

#### 2.1.3.2 Photometric scale-lengths

The main hypothesis underlying the stacking technique as a reliable statistical tool to investigate halo properties is an assumed self-similarity of the disk

## 2 The stellar halo of disc galaxies

---

galaxies, or at least of their diffuse component. There must exist a ‘characteristic’ scale-length, such that after rescaling, all galaxies can be superposed. The validity of this assumption will be discussed in more detail in Sec. 2.1.4.2. Since the surface brightness distribution of edge-on disks is affected strongly by dust extinction, we chose the  $i$  band ( $\lambda_{\text{eff}} = 7480\text{\AA}$ ) as the reference pass-band in order to characterise the scale-length of our sample. This choice represents the best trade-off between the need for a high sensitivity and the desire to limit the effects of dust<sup>3</sup>. Many different scale-lengths can be defined from photometric analysis.

We consider the following four scale-lengths:

- the Petrosian radius  $r_{\text{Petro}}$ , as obtained from the SDSS photometric database (see Stoughton et al. 2002; Abazajian et al. 2003)
- the effective or half light radius  $r_{50}$
- the exponential scale-length  $r_{\text{exp}}$
- an isophotal radius obtained from the one-dimensional light profile along the major axis  $r_{1\text{D}}$

$r_{50}$ ,  $r_{\text{exp}}$  and  $r_{1\text{D}}$  have been determined using dedicated software developed in the IRAF environment. In order to evaluate the two former parameters, we derive a surface brightness profile from circular aperture photometry extending out to 1.5 isophotal ( $\mu_i = 25 \text{ mag arcsec}^{-2}$ ) radii.  $r_{50}$  is then obtained as the radius enclosing 50 per cent of the total flux, while the exponential scale radius  $r_{\text{exp}}$  is derived from the least squares fit to the surface brightness profile between  $r_{50}$  and  $r_{90}$  (i.e. the radius enclosing 90 per cent of the flux). The basic motivation for analysing an one-dimensional brightness profile, derived by collapsing the image of the galaxy along the minor axis, is to have an estimate of the brightness which is as much as possible independent of the inclination. The surface brightness enhancement is, in fact, important and severely dependent on the inclination, when the edge-on condition is approached. Assuming low or negligible extinction, the quantity  $\zeta \equiv -2.5 \log \frac{d\text{Flux}(x)}{x dx}$ , where  $\text{Flux}(x)$  is the flux enclosed within the projected distance  $x$  from the minor axis of the galaxy, is independent both of the inclination and of the distance of the galaxy. As reference level for determining  $r_{1\text{D}}$  we chose  $\zeta = 25.0 \text{ mag arcsec}^{-2}$ , which corresponds roughly to a surface brightness of  $\mu = 25.0 \text{ mag arcsec}^{-2}$  for a typical edge-on galaxy.

All four scale-lengths are quite strongly correlated, as expected for self-similar

---

<sup>3</sup>The  $z$  band is in fact the red-most one, but its sensitivity is about a factor 2-3 lower than the  $i$  band.

## 2.1 Haloes around edge-on disk galaxies in the Sloan Digital Sky Survey

**Table 2.1:** Median scale-lengths (in arcseconds) and rescaling reference values (in pixel)

$r_{\text{Petro}}$		$r_{50}$		$r_{\text{exp}}$		$r_{1D}$	
arcsec	pix	arcsec	pix	arcsec	pix	arcsec	pix
10.07	25	4.74	12	3.76	10	15.50	40

exponential profiles. The typical scatter around the 1:1 relation between pairs of corresponding scale-lengths is  $\sim 15$  per cent.

### 2.1.3.3 The image transformation and stacking

For each of the four scale-lengths considered, the median value in the sample, rounded to an integer number of pixels<sup>4</sup>, has been taken as reference for the rescaling, as given in Table 2.1. All galaxy images have been geometrically transformed using the drizzle re-sampling technique (as implemented in the IRAF **geotran** task) in order to correctly propagate the original noise properties. Each image has been translated to the galaxy centre, rotated according to the measured position angle of the major axis, and expanded or contracted according to the ratio between the reference scale length and the corresponding measured one. The same transformation has been applied to the corresponding mask, and a ‘grow radius’ of 10 pixels (in the original image size) around each masked pixel has been adopted in order to mask the extended PSF wings of the brightest sources. Since each image has a different photometric calibration and the measured surface brightness of a galaxy is differently affected by Galactic attenuation, depending on its location in the sky, an intensity rescaling is needed as well. The transformation from the original pixel intensity  $i$  to the rescaled one  $i'$  is given by the following formula:

$$i' = i \times 10^{-0.4(Z_p - Z_{p,\text{ref}} - K \times \text{Airmass} - \text{Reddening})},$$

where  $Z_p$  and  $Z_{p,\text{ref}}$  are the flux calibration zero points of the image and of reference, respectively,  $K \times \text{Airmass}$  is the airmass correction, and  $\text{Reddening}$  is the attenuation due to our Galaxy, as given by Schlegel, Finkbeiner, & Davis (1998). All the quantities are expressed in magnitudes.

The combination of the transformed and rescaled images has been performed using the **imcombine** IRAF procedure. First of all, the masked pixels are rejected. The median of the count distribution of the remaining pixels is then calculated in order to obtain the median image. An average image is

<sup>4</sup>The pixel scale of the SDSS CCDs is  $0.396 \text{ arcsec pix}^{-1}$

## 2 The stellar halo of disc galaxies

---

calculated as well, after clipping the 16 per cent percentile tails of the count distribution of the unmasked pixels. Adopting the standard approximation for the mode of a distribution

$$mode = 3 \times median - 2 \times average,$$

we calculate the mode image. The resulting  $512 \times 512$  pixel<sup>2</sup> images extend much beyond the detected emission from the galaxies and allow us to determine the properties of the background in great detail. A careful comparison between the three statistical combinations shows that, despite of the conservative masking method adopted, the diffuse luminosity of sources other than the considered galaxies can result in significant skewness in the pixel count distribution and in a systematic increase of the sky surface brightness up to 31 mag arcsec<sup>-2</sup> in i-band in the outermost regions of the average frame with respect to the innermost ones, in which contaminating sources are avoided by selection. This systematic effect in the background is almost completely removed in the mode image. In the following, therefore, we will always refer to that one as the resulting stacked image.

For each stacked image the residual background level is determined as the count mode in an annulus of 130 pixel inner radius, 96 pixel thick, and subtracted.

In Fig. 2.2 we present the images for the four most sensitive pass-bands ( $g$ ,  $r$ ,  $i$ ,  $z$ ), obtained by stacking the images rescaled according to the galaxy exponential scale length. For the  $u$  band the signal-to-noise is not sufficient to say anything about the presence and the characteristics of halo emission, therefore we will neglect this band in the following analysis and discussion. Rescaling according to the other scale-lengths does not change the resulting images significantly, as we will demonstrate more quantitatively later on, and therefore they are not shown here. Intensity levels in Fig. 2.2 are coded in square-root transformation grey scale, suitably adjusted to show the maximum extension of the low surface brightness envelope. We superpose isophotal contours in two magnitude ranges: black contours, corresponding to the faintest isophotes, are obtained adopting a boxcar smoothing scale of  $10 \times 10$  pixel, whereas the white, brightest ones, have been calculated with a  $2 \times 2$  pixel smoothing scale. The represented isophotal levels are given in the figure caption. The images and the superposed isophotes show very clearly the presence of a diffuse luminous envelope around the disk, in all four considered bands. This halo (whatever physical meaning we give to this word) is particularly evident and round in the  $r$  and the  $i$  bands, whereas it is significantly flattened in the  $g$  and  $z$  bands (but the lower sensitivity in the latter band does not allow us to say much).

## 2.1 Haloes around edge-on disk galaxies in the Sloan Digital Sky Survey

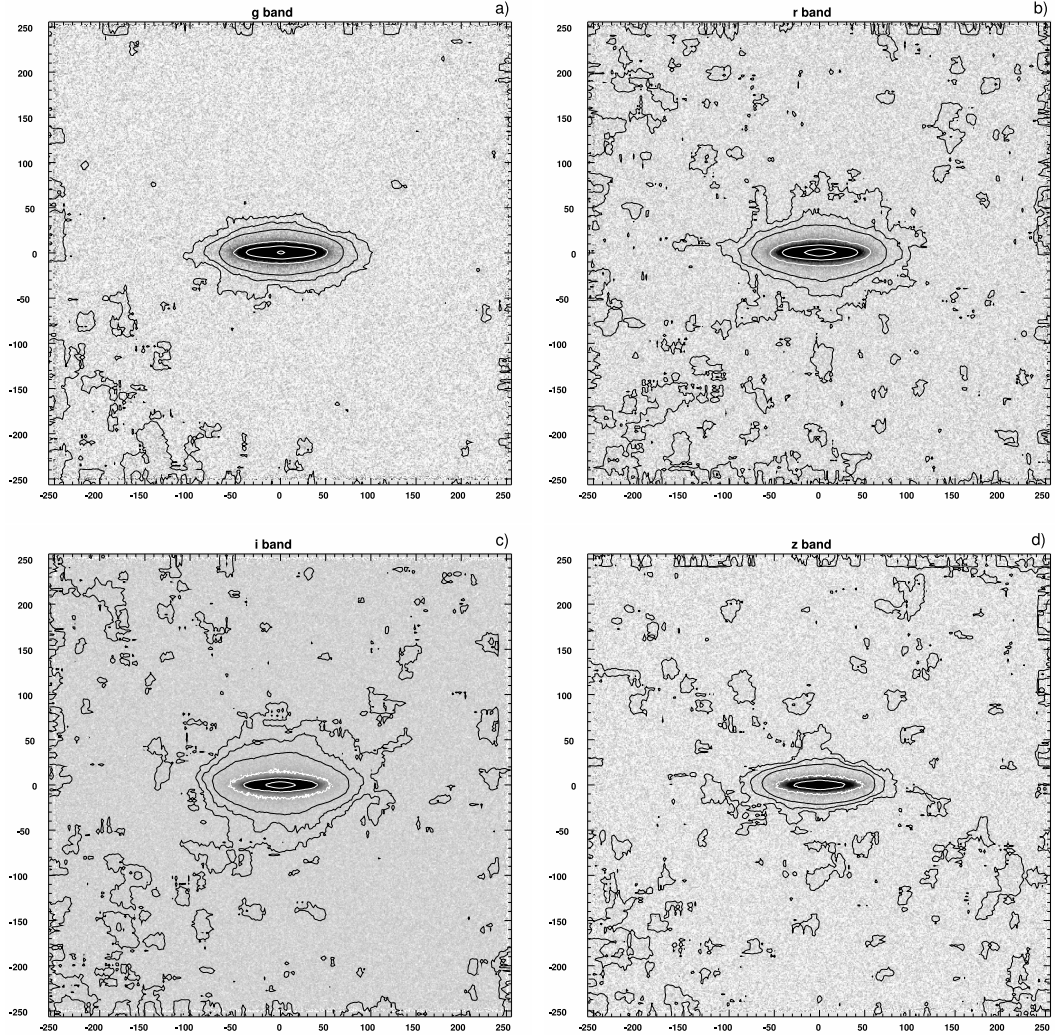


**Figure 2.2:** The images resulting from the stacking of the galaxies rescaled according to their exponential scale length, in  $g$ ,  $r$ ,  $i$ , and  $z$  band. Intensity is coded in grey levels through a square root transformation, adopting arbitrary bias and contrast. The overplotted isophotal levels are as follows: 30.0, 29.0, 28.0, 26.0, 24.0, 22.0 for the  $g$  and the  $r$  band; 29.5, 28.5, 27.5, 25.5, 23.5, 21.5 for the  $i$  band; 28.0, 27.0, 26.0, 24.0, 22.0 for the  $z$  band. See text for the details. The scales indicate the offset from the galaxy centre in pixel,  $10 \text{ pixel} = r_{\text{exp}}$ .

## 2 The stellar halo of disc galaxies

---

### 2.1.4 The analysis

In this section we present the results of an analysis of the stacked images in the  $g$ ,  $r$ ,  $i$ , and  $z$  pass-bands. We mainly concentrate on the stacking of the complete sample (1047 galaxies), because of the resulting higher sensitivity, but we also consider the stacking of three subsamples of bright, intermediate and low luminosity flat galaxies (Sec. 2.1.4.5), in order to better understand the possible dependence of the observed halo properties on total luminosity. After analysing the background properties of the stacked images in order to assess our detection limits (Sec. 2.1.4.1), the photometric properties are investigated by means of radial sector-averaged surface brightness profiles (Sec. 2.1.4.2), and compared to different models of luminosity distributions, namely thin+thick disks and disk+halo (Sec. 2.1.4.3). The average halo colours are presented in Sec. 2.1.4.4. Unless otherwise specified, we will always use the stacking of the images rescaled according to the exponential disk scale-length. We devote an entire paragraph in Sec. 2.1.4.2 to demonstrate that the adopted scale-length is not critical in determining the characteristics of the observed halos.

#### 2.1.4.1 The background noise properties

Since our photometric measurements are performed by integrating the flux over different image areas, as will be explained in Sec. 2.1.4.2, it is crucial to determine the noise properties on different scales. The presence of large-scale fluctuations is already obvious from a superficial inspection of the contour plots in Fig. 2.2. We restrict the analysis of the noise to the annulus (130 pixel inner radius and 96 pixel thickness) on which the sky level has been computed, and we consider the rms of the intensity after re-binning the image by different linear factors, ranging from 1 to 50. The dependence of the  $rms$  on the scale-length  $L$  is well described by a power law of the form

$$rms(L) = rms_0 L^{-\alpha}, \quad (2.1)$$

where  $rms_0$  is the noise on one-pixel scale, and  $\alpha \sim 0.7 - 0.8$ , thus indicating that the noise has significant large scale structure in excess to what is expected in the case of pure Gaussian noise (for which  $\alpha = 1$ ).

#### 2.1.4.2 The surface brightness profiles

The most obvious way to investigate the properties of the approximately round, low surface brightness structures emerging in Fig. 2.2 is to extract surface brightness (SB) profiles, averaging the flux in large wedges at different

## 2.1 Haloes around edge-on disk galaxies in the Sloan Digital Sky Survey

position angles. First of all, we divide the image in four circular sectors of  $60^\circ$  aperture, centred at  $0^\circ$ ,  $90^\circ$ ,  $180^\circ$  and  $270^\circ$  position angles (PAs). Each of these sectors is in turn radially divided into a number of coronae, geometrically spaced such that the outer radius of the  $k$ th corona is given by  $r_k = r_0 \cdot 1.15^k$ , with  $r_0 = 6$  pixel  $= 0.6 r_{\text{exp}}$ . Finally, we estimate the mean SB as a function of the radius for  $0^\circ$  (i.e. along the disk) and  $90^\circ$  PA (i.e. perpendicular to the disk) averaging the SB in pairs of corresponding coronae in the two symmetric sectors at  $0^\circ$  and  $180^\circ$  and at  $90^\circ$  and  $270^\circ$  PA, respectively. In each of the four graphs of Fig. 2.3 we show the SB profiles for the  $g$ ,  $r$ ,  $i$ , and  $z$  images respectively, in linear scale (upper left panel) and logarithmic scale (upper right panel): open circles represent the  $0^\circ$  PA profile, filled triangles the  $90^\circ$  PA. The shaded areas represent the level of the rms background fluctuations at the scale length corresponding to the area of the coronae in which the SB is averaged, as calculated in the previous section. Thus the  $1 - \sigma$  detection limits for the SB profiles can be assessed as  $\sim 31$  mag arcsec $^{-2}$  for the  $g$ ,  $r$  and  $i$  band and as  $\sim 28$  mag arcsec $^{-2}$  for the  $z$  band.

In order to evaluate the errors on the SB we must consider contributions from 1) the background fluctuations and 2) the intrinsic scatter in the average signal from a galaxy. The first one is just provided by the background rms as evaluated in the previous section using Eq. 2.1, with  $L$  given by the square root of the area of the corona over which the signal is integrated. The estimation of the intrinsic scatter contribution is much more cumbersome, since the shape of the statistical distribution of the pixel counts in the coronae is not known *a priori* and the light distribution of the galaxy itself is likely to give a major contribution to the rms of the count statistics. In order to remove it, for each pixel we consider the deviation from the average intensity of the corresponding pixels in the four image quadrants, which are symmetric with respect to the  $x$  and  $y$  axes, and express the intrinsic rms as:

$$rms_{\text{intrinsic}} = \sqrt{\frac{1}{3N} \sum_{i=1}^N \sum_{j=1}^4 [I_{ij} - \langle I_{ij} \rangle_j]^2} \quad (2.2)$$

where  $I_{ij}$  is the pixel intensity,  $N$  is the number of pixels per corona per quadrant, and  $\langle I_{ij} \rangle_j$  is the average intensity over the  $j$  index. In the absence of any large scale background fluctuation the error on the average intensity is just obtained dividing the (2.2) by  $\sqrt{4N}$ . Adding the contribution of the large scale fluctuations, we can write the error as:

$$\sigma = \sqrt{\frac{(rms(L))^2}{2} + \frac{rms_{\text{intrinsic}}^2}{4N}} \quad (2.3)$$

## 2 The stellar halo of disc galaxies

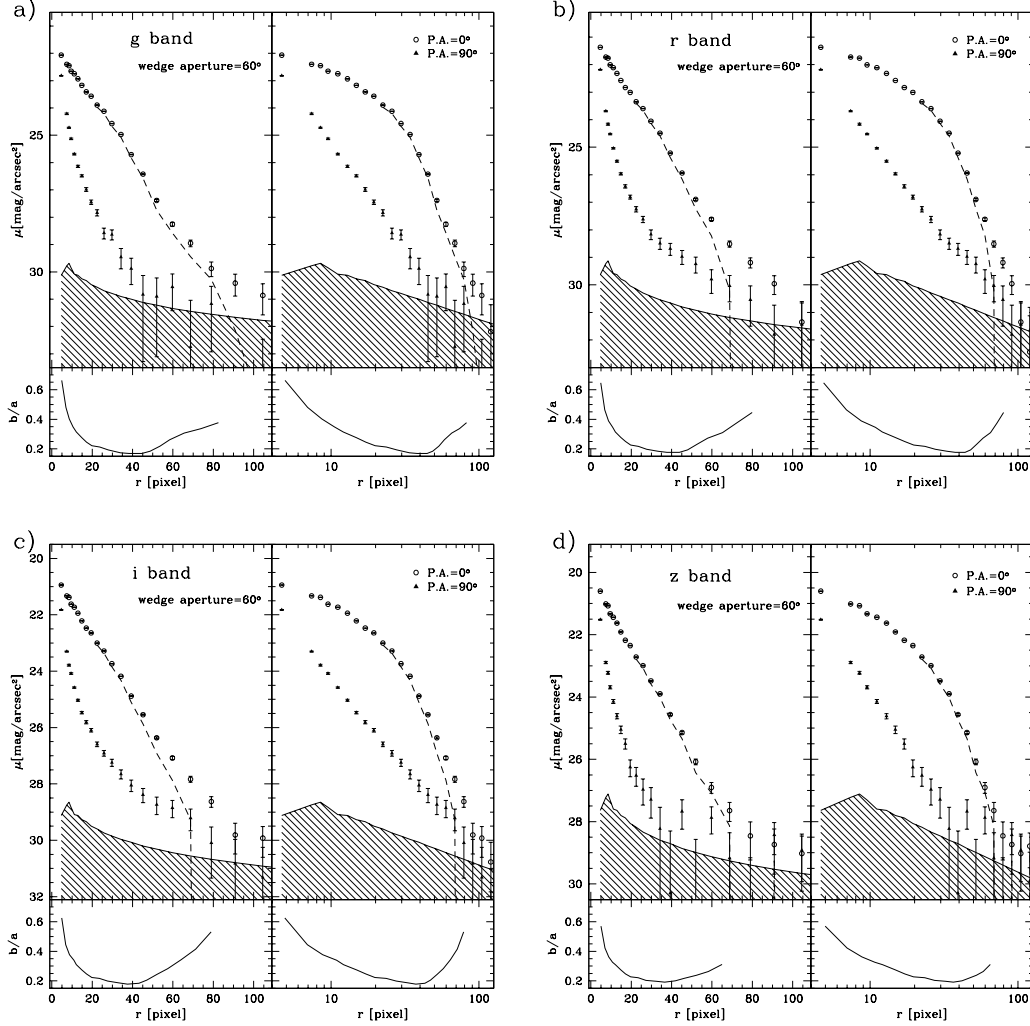


**Figure 2.3:** The SB profiles in  $g$ ,  $r$ ,  $i$ , and  $z$  band, in  $60^\circ$  wedges along the disk (PA= $0^\circ$ , open circles) and perpendicular to it (PA= $90^\circ$ , filled triangles). Distances from the centre in pixels (10 pixels corresponding to  $1 r_{\text{exp}}$ ) are shown in linear scale (left panels) and logarithmic scale (right panels). The sky rms is represented by the shaded areas. Dashed lines represent the ‘pure’ disk profile at  $r > 20$  pix, obtained as explained in the text. The bottom panels of each graph show the  $b/a$  axial ratio of the isophotes as a function of the major axis  $a$ .

## 2.1 Haloes around edge-on disk galaxies in the Sloan Digital Sky Survey

---

where  $rms(L)$  is given by Eq.2.1 with  $L$  given by the square root of the area of the corona, and the factor 2 comes in from having averaged two coronae. Such an error estimate has been proved to be consistent with the scatter of the average intensity in the corresponding coronae in the four quadrants.

In the lower panels of each graph in Fig. 2.3 we plot the axial ratio  $b/a$  of the isophotes as a function of the radius (semi-major axis). This is calculated as follows. We assign a number of SB levels and determine the radius  $r$  at which such SB's are reached at different PAs  $\theta$ , by interpolating the SB profiles extracted from 6 wedges per quadrant. Assuming  $r = r(\theta)$  is well represented by an ellipse with the major axis along the x direction, we derive the best fitting semi-axes  $a$  and  $b$  by means of a standard least squares algorithm.

As it is apparent from the straight-line behaviour of the open circles in the linear-scale plots of Fig. 2.3, the profile of the wedges centred on the disk show an exponential decrease of the SB with radius, as it is typical for disks. Perpendicular to the disk, instead, the rapid initial decrease of the SB becomes shallower as we go further away from the centre of the galaxy. The trend is well approximated by a power-law with index  $\sim 2$ , as the straight-line behaviour of the triangles in the log-scale plots points out. This is in general true for the four bands analysed. However, the relative intensity at the same radial distance along the disk and perpendicular to it is different in different bands, reflecting a possible dependence of the flattening of the diffuse halo on the band and, in turn, this points to colours gradients in the halo itself. As already noted from the isophotal contours in Fig. 2.2, the halo is prominent in the  $r$  and the  $i$  band, reaching a SB comparable to that of the disk at  $r \sim 8 - 10 r_{\text{exp}}$  and making the isophotal shape significantly rounder ( $b/a \sim 0.5 - 0.6$ ). In the  $g$  band the halo has very little extension (the surface brightness drops below  $31 \text{ mag arcsec}^{-2}$  beyond  $\sim 4 r_{\text{exp}}$ ), thus leaving the isophotes extremely flattened. For the  $z$  band the measurements are inconclusive: there is some hint of a shallowing of the slope of the profile, but the  $S/N$  drops below 1 already at  $\sim 3 r_{\text{exp}}$  at the level of  $28.5 \text{ mag arcsec}^{-2}$ .

In Fig. 2.3, for  $r > 20 \text{ pix}$ , we also show as dashed lines the 'pure disk' profiles obtained subtracting the  $90^\circ$  profile from the  $0^\circ$  profile, after stretching the former by a factor  $0.6^{-1}$  to take the flattening of the halo into account (see Sect. 2.1.4.3 for details on the 0.6 factor). There is evidence that the 'pure' disk slope steepens beyond  $4 - 5 r_{\text{exp}}$  in the  $r$  and  $i$  bands, consistent with studies of individual disks in the literature (see e.g. van der Kruit 2001; Kregel, van der Kruit & de Grijs 2002, and references therein), whilst the results are unclear in the  $g$  and  $z$  bands.

## 2 The stellar halo of disc galaxies

---

In order to rule out scattered light and the extended wings of the point spread function (PSF) as major contributors to the observed halos, we have performed the same stacking procedure on the images of stars taken from the same frames as the galaxies to generate effective PSF's in each band. In each frame we identify a star 1) whose central brightness differs by less than  $2 \text{ mag arcsec}^{-2}$  from the central SB of the galaxy and 2) which is distant from other contaminating sources, as requested for the galaxy selection. Then, sources other than the star are masked, the frame is re-centred on the star and the same geometrical transformations as applied to the galaxy are performed. The radial profile of the PSF can be reproduced by a Gaussian core plus exponential wings over a large extension. Fig. 2.4 shows the analytic fit to the measured PSF's in the four bands, expressed as the difference of magnitude with respect to the central surface brightness. The decline in the core is very sharp,  $6 - 7 \text{ mag arcsec}^{-2}$  within 5 pixel, and the exponential wings contribute less than  $1/10^4$  of the central surface brightness at radii larger than 20 pixels. We will analyse the effects of the PSF on the measured profiles in the next section, by convolving with different models for the light distributions.

The characteristics of the observed halo profiles show little or no dependence on the scale-length adopted for rescaling the images of the galaxies. In Fig. 2.5 we plot the SB profile in the  $90^\circ$  PA wedge in the four bands, using different symbols for the different rescalings: open circles for  $r_{\text{exp}}$ , filled triangles for  $r_{50}$ , open squares for  $r_{\text{iso1D}}$  and filled circles for  $r_{\text{Petro}}$ . The  $r$  coordinate of each point is exactly rescaled in order to match the sample median values of the four scale-lengths considered. As in Fig. 2.3, the shaded areas represent the sky rms. The error-bars are calculated as explained before. The agreement between the different rescalings is extremely good: almost all points are consistent within the error-bars, with a handful of exceptions for the  $r_{\text{iso1D}}$  rescaling. Even for these, the deviation is less than  $3 \sigma$ . Thus we conclude that there is no systematic dependence of the average halo properties on the profile shape of the disk as described by variations in relative scale-lengths.

### 2.1.4.3 Modelling the halo

In this section we investigate the structural properties of the detected emission by means of simple models of the light distribution. In particular, we consider the possible contribution from a thick disk component, with an exponential vertical light density distribution, and from a (moderately) flattened power-law halo. Making predictions from models of this kind is non-trivial and must take into account that the observed emission results from a double convolu-

## 2.1 Haloes around edge-on disk galaxies in the Sloan Digital Sky Survey

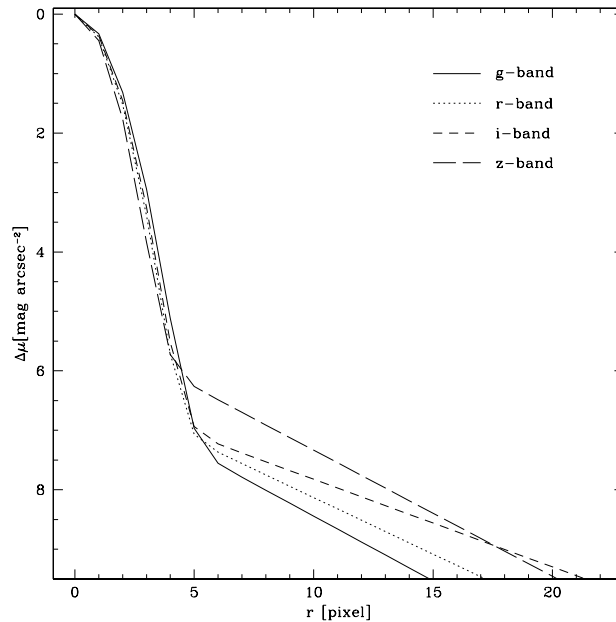


**Figure 2.4:** The PSF profiles in  $g$  (solid line),  $r$  (dotted line),  $i$  (short-dashed line), and  $z$  band (long-dashed line), expressed as difference of magnitude with respect to the central surface brightness. The lines represent the analytic fit (Gaussian core plus exponential wings) to the radial profile measured on the stacked image of stars, as explained in the text.

tion of the ‘true’ average light density distribution of the galaxies with 1) the distribution of inclinations and 2) the effective PSF, as computed above. The models are calculated as follows. First we assume a particular 3-dimensional distribution of light. We produce a set of 1000 Monte Carlo realizations of the projected surface brightness, uniformly varying the inclination angle of the disk between 0 and 15 degrees (roughly corresponding to a projected axial ratio between 0 and 0.25 for an infinitely thin disk, as required by the sample selection criterion for the galaxies). The 1000 realizations are then averaged and convolved with the analytic PSF computed in the previous section, separately for each band. We do not expect to reproduce the stacked images near the nucleus nor at small distances from the disk plane, because we do not model dust extinction. Thus we compare our models to the observations by means of vertical-cut profiles, that allow us to exclude these ‘forbidden’ regions. In each cut, whose width is chosen to be proportional to the distance from the minor axis of the image, we average the flux coming from the four

## 2 The stellar halo of disc galaxies

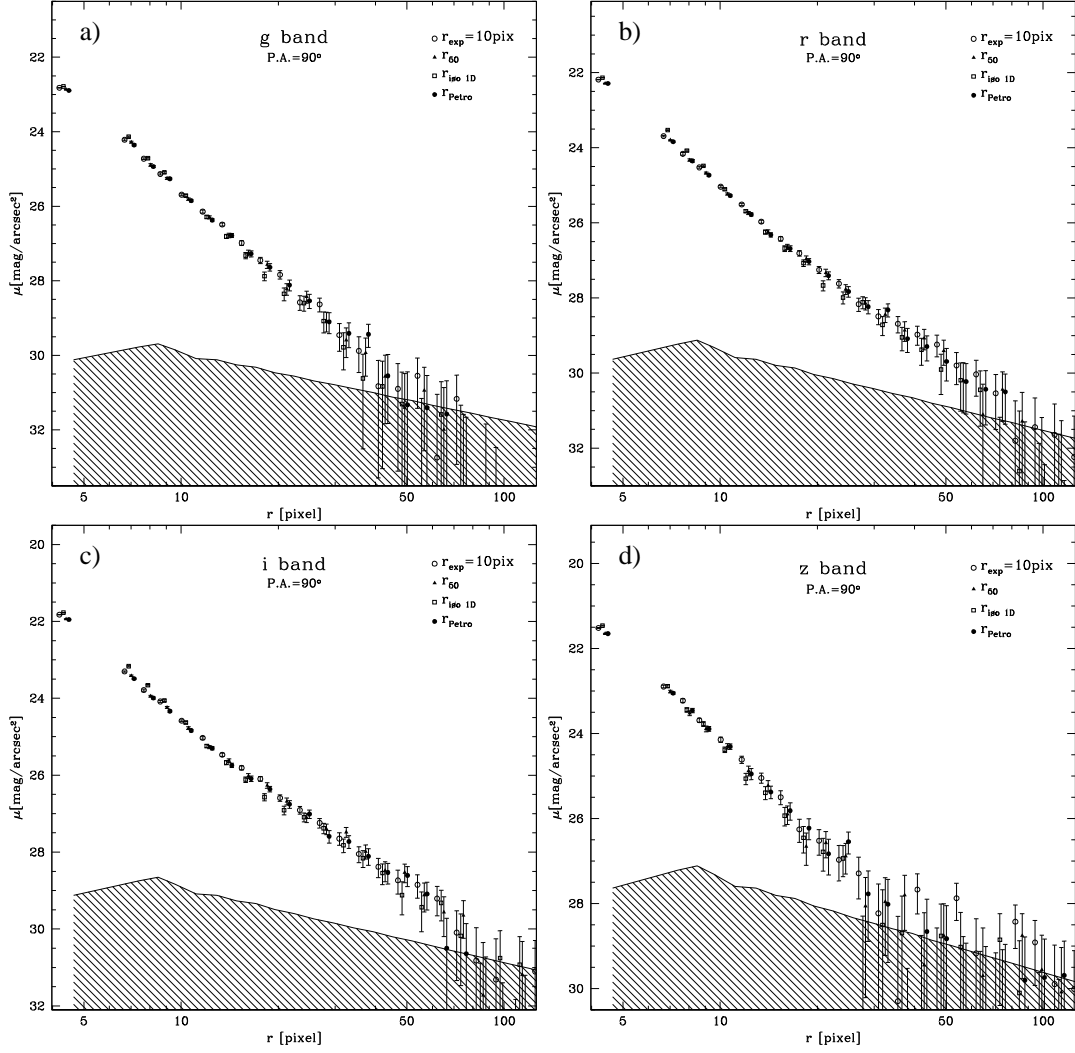


**Figure 2.5:** The surface brightness profiles in  $g$ ,  $r$ ,  $i$  and  $z$  band, at  $90^\circ$  PA, for different adopted rescalings. Open circles refers to images rescaled according to  $r_{\text{exp}}$ , filled triangles to  $r_{50}$ , open squares to  $r_{\text{iso1D}}$  and filled circles to  $r_{\text{Petro}}$ . The sky rms is represented by the shaded areas.

quadrants.

In the thin+thick disk model the 3-dimensional light density of each individual galaxy is assumed to be given by:

$$\nu(r, z) = N e^{-\frac{r}{r_{\text{exp}}}} \left[ e^{-\frac{|z|}{z_{\text{thin}}}} + R \frac{z_{\text{thin}}}{z_{\text{thick}}} e^{-\frac{|z|}{z_{\text{thick}}}} \right] \quad (2.4)$$

## 2.1 Haloes around edge-on disk galaxies in the Sloan Digital Sky Survey

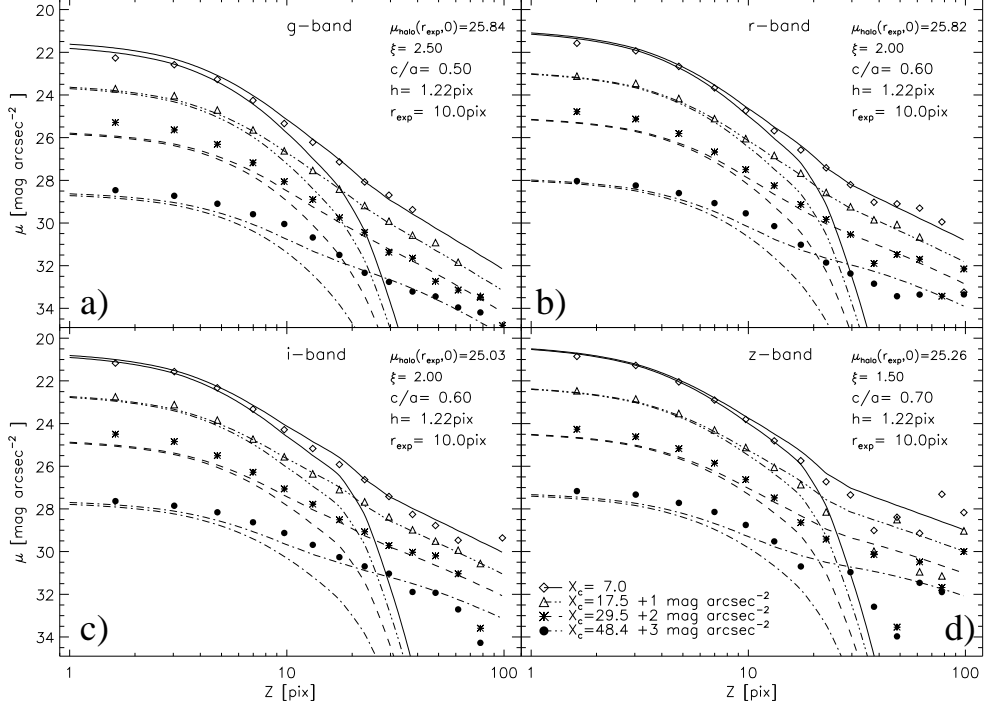


**Figure 2.6:** Vertical cut SB profiles with superposed the prediction from the power-law halo+disk model. Points are the SB measured in four vertical cuts at distance  $X_c$  from the centre (in pixel units, see legend). Profiles are offset 1 mag arcsec<sup>-2</sup> from each other. Heavy lines represent the model profiles, light lines are the disk component of the model alone.

where  $N$  is the normalisation factor,  $R$  is the flux ratio of the thick over the thin disk,  $r_{\text{exp}}$  is the exponential scale-length of the radial SB distribution,  $z_{\text{thin}}$  and  $z_{\text{thick}}$  are the exponential vertical scale-lengths of the thin and thick disks respectively. We fix  $r_{\text{exp}} \equiv 10$  pixels, and  $z_{\text{thin}} \equiv 1$  pixel. No disk truncation is adopted. The realizations cover a logarithmic spaced grid of four by four values in the  $z_{\text{thick}} - R$  parameter space ( $z_{\text{thick}}$  ranging from  $10^{0.2}$  to  $10^{0.8}$  pixels,  $R$  from 0.01 to 0.4). The normalisation  $N$  is left as a free parameter and fitted by minimising the  $\chi^2$ . We find that the thin+thick disk models fail to reproduce the observed SB distribution of the observed halos, since they predict a sharp exponential cut-off of the SB along the  $z$  coordinate, which is inconsistent with the observed power-law profile.

In the disk+halo models, we assume a halo component with a generalised Hubble density distribution as introduced by Elson, Fall & Freeman (1987),

## 2 The stellar halo of disc galaxies

---

modified to allow the iso-density surface to be oblate spheroids:

$$\nu_{\text{halo}}(r, z) \propto \left[ 1 + \frac{r^2 + \frac{z^2}{(c/a)^2}}{r_c^2} \right]^{-(\xi+1)/2} \quad (2.5)$$

where  $c/a$  is the flattening parameter,  $r_c$  is the softening parameter or core radius<sup>5</sup>, and  $\xi$  is the power-law index of the projected SB. The disk component is modelled by a double exponential distribution in  $r$  and  $z$ , without any truncation:

$$\nu_{\text{disk}}(r, z) \propto e^{-\frac{r}{r_{\text{exp}}}} \cdot e^{-\frac{|z|}{h}} \quad (2.6)$$

with  $r_{\text{exp}}$  and  $z_0$  representing the exponential scale lengths in  $r$  and  $z$  respectively. We fix  $r_c \equiv 1$  pixel and  $r_{\text{exp}} \equiv 10$  pixels, and realize a grid of models in the  $h - \xi - (c/a)$  parameter space, covering the following ranges:  $h = 0.50 - 3.00$ ,  $c/a = 0.3 - 1.0$ ,  $\xi = 1.50 - 4.00$ . The total (disk+halo) normalisation and the normalisation of the halo relative to the disk for each model on the grid have been fitted by minimising the  $\chi^2$ . The best fitting models for the  $g$ ,  $r$ ,  $i$  and  $z$  band are represented in Fig. 2.6. For each band we plot the vertical SB profiles at four different distances  $x_c$  from the centre of the galaxy, as obtained in the vertical cuts described above, offset by 1 mag arcsec<sup>-2</sup> one from the other. Even if the  $\chi^2$  are extremely high, thus demonstrating that the adopted models cannot reproduce in the details the complexity of the galaxy structure, the general agreement with the measured points is satisfactory and we are successful in reproducing the trend of the profiles. Besides the total model profiles (heavy lines), we plot also the exponential disk components alone (light lines): while dominating at small height, they give negligible contribution at  $z \gtrsim 30$  pixels ( $3 r_{\text{exp}}$ ). The best fitting model parameters are reported in the panels of Fig. 2.6. The disk scale-height is quite well constrained to  $h \sim \frac{1}{10} r_{\text{exp}}$ . The power-law slope ( $\xi$ ) is steeper in  $g$  band (2.50), and increasingly shallower in  $r$  and  $i$  (2.00) and  $z$  band (1.50), while the halo shapes get increasingly rounder from  $c/a = 0.50$  in  $g$ , to 0.60 in  $r$  and  $i$ , and 0.70 in  $z$  band. This is in good agreement with the previous analysis on the images themselves and on the radial profiles. The surface brightness of the halo component at  $r = r_{\text{exp}}$  along the minor axis is 25.84, 25.82, 25.03 and 25.26 mag arcsec<sup>-2</sup> in the  $g$ ,  $r$ ,  $i$  and  $z$  band respectively. We can estimate the amount of halo light coming from outside the 25 mag arcsec<sup>-2</sup> isophote as  $\sim 2 - 3$  per cent of the total galaxy light.

The models derived above allow us to quantify the pollution of the outer envelope by scattered light and PSF wings. We note that, at  $r = 20$  pix, the

---

<sup>5</sup> The core radius is introduced only for mathematical convenience, to avoid the central divergence of a pure power law.

## 2.1 Haloes around edge-on disk galaxies in the Sloan Digital Sky Survey

PSF-convolved disk component contributes  $\sim 30$  per cent of the total surface brightness<sup>6</sup>. This contribution decreases very rapidly at larger distances, and becomes negligible at  $r > 30$  pix in all the bands. We conclude that scattered light from the disk contributes much less than 30 per cent of the total (disk+halo) measured light beyond 20 pixel.

### 2.1.4.4 The halo colours

Based on the SB profiles presented in Sec. 2.1.4.2, we derive the colour profiles in the two  $60^\circ$ -aperture sectors including the disk and perpendicular to it. We concentrate on the  $g - r$  and  $r - i$  colours, excluding colours involving the  $z$  band, because of its lower sensitivity. In Fig. 2.7 the dots represent the colours measured perpendicular to the disk, with the error-bars derived from the errors on the SB profiles; for comparison, with the dotted lines we plot the colour profiles for the disk. This has a blueing gradient toward the outer parts, which is particularly evident for  $g - r$ , but it is still clearly apparent in  $r - i$ . Disk colours ( $g - r = 0.7 - 0.5$ ,  $r - i \approx 0.4$ ) are consistent with typical star-forming galaxies, once we allow for significant dust extinction, as expected for edge-on conditions. The increasing presence of dust near the galaxy centre and age and metallicity gradients in the disk can also easily explain the observed gradients. Beyond  $4 - 5 r_{\text{exp}}$  there is evidence for colours getting redder, possibly indicating that the halo is overtaking the disk. This is consistent with the steepening of the profiles of the ‘pure disk’, shown as dashed lines in Fig. 2.3.

The  $g - r$  profile perpendicular to the disk is extremely noisy: no clear trend can be established and the measurements are definitely unreliable beyond 20 pixels. The halo in these bands is roughly as red as the inner parts of the disk. The  $r - i$  colour shows instead a clear reddening toward the outskirts of the galaxy, reaching extremely red colours  $\sim 0.8$ , about 0.4 mag redder than the disk. We derive the best estimate of the halo colours using the mean colour around 20 pixels and consider the uncertainties given both by the error bars and by the scatter of the points around an ‘ideal’, smooth profile:

$$g - r = 0.65 \pm 0.1$$

$$r - i = 0.60 \pm 0.1$$

These results are not corrected for the effects of the PSF. Based on the analysis in the previous section, we estimate that the SB at  $r = 20$  pixel is polluted by scattered light from the inner parts by up to  $\sim 30$  per cent. However, this contribution is very similar in all the bands (20 per cent in the  $g$ , 33 per cent in the  $r$  and the  $i$  bands) and can redden the real halo colours by some hundredths up to 0.2 mag (worse case for  $g - r$ ). It is worth stressing

---

<sup>6</sup>20 per cent in the  $g$ , 33 per cent in the  $r$  and the  $i$ , and 40 per cent in the  $z$  band

## 2 The stellar halo of disc galaxies

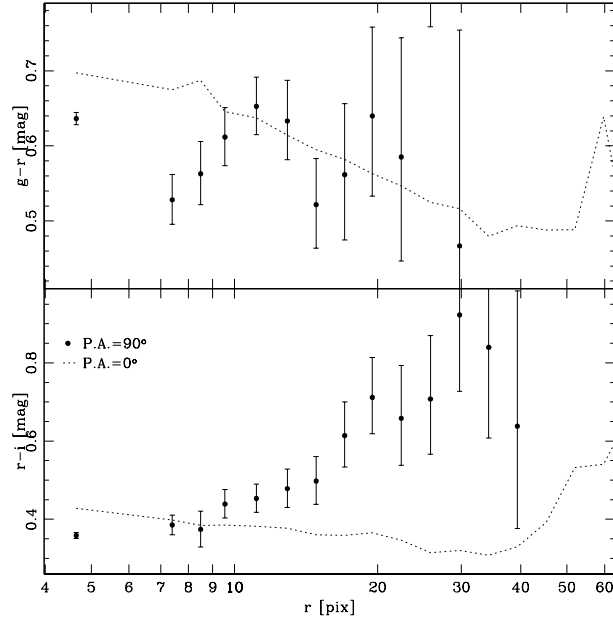


**Figure 2.7:** The  $g - r$  and  $r - i$  colour profiles. The filled circles refer to the  $60^\circ$ -aperture sector perpendicular to the disk, the dotted lines represent the colours in the wedge along the disk.

that this assessment has large uncertainties, due to the very simplistic nature of the models here adopted and to their extreme sensitivity to the fitting parameters (e.g., changing the vertical scale-length of the disk affects very slightly the goodness of the fit, but can significantly change the disk and scattered light contributions to the colours at 20 pixels).

The robustness and the significance of the estimates given above, will be discussed in detail in Sec.2.1.5.

### 2.1.4.5 Dependence on the total galaxy luminosity

In order to understand the dependence of the halo features on the galaxy luminosity, we analyse the stacked images (exponential scale-length rescaling) for three luminosity bins in the  $i$  band, namely the ‘bright’ ( $-22.5 < i_{\text{abs}} + 5 \log h \leq -20.2$ ), the ‘intermediate’ ( $-20.2 < i_{\text{abs}} + 5 \log h \leq -19.0$ ) and the ‘faint’ one ( $-19.0 < i_{\text{abs}} + 5 \log h \leq -16.0$ ). The profiles at  $0^\circ$  and  $90^\circ$  PA (obtained as in Sec. 2.1.4.2) are plotted in Fig. 2.8: open triangles for the ‘faint’ bin, filled squares for the ‘intermediate’, and open circles for the

## 2.1 Haloes around edge-on disk galaxies in the Sloan Digital Sky Survey

---

‘bright’. The solid lines running through the points are the profiles as obtained from the complete sample. We notice that the halo SB is correlated with the luminosity of the galaxy, with the less luminous ones having also fainter halos. A similar correlation with the total luminosity holds for the disk SB as well, indicating that the relative brightness of the halo with respect to the disk is roughly constant. This luminosity dependence is barely observable in the  $g$  band, but becomes increasingly evident at longer wavelengths, with an average offset of  $\sim 0.5$  mag arcsec $^{-2}$  between the ‘bright’ and the ‘faint’ profile in the  $i$  band. This also implies that the halos of the bright galaxies are redder than the faint ones by some 0.1 mag in both  $g - r$  and  $r - i$  colours.

### 2.1.5 Discussion

The analysis performed in the previous section provides strong evidences for the generalised presence of a diffuse, low-surface brightness stellar component around disk galaxies. By stacking more than 1000 images, we are able to extract reliable photometry at SB level as faint as  $\sim 31$  mag arcsec $^{-2}$  in the  $g$ ,  $r$  and  $i$  band and  $\sim 28$  mag arcsec $^{-2}$  in the  $z$  band.

It is worth stressing that the statistical estimator adopted in this work to compute the combined images is extremely robust. The evaluation of the *mode* for each pixel in the composite image as  $3 \times \text{median} - 2 \times \text{average}$ , with the *average* calculated over the count distribution after rejecting the 16 per cent percentile tails and the masked pixels, is effective in removing outliers and spurious contributions from other sources, and in correcting for the skewness of the distribution, while reducing the noise of the standard *mode* estimation. The isophotal contours superposed to the images in Fig. 2.2 show the presence of luminous halos whose shape is clearly rounder than the highly flattened central disk. The shape of the effective PSF, obtained from the stacking of 1000 stars selected from the same frames and with similar criteria as the galaxies, after applying the same geometrical transformations, is not consistent with scattered light and extended PSF wings giving a major contribution to the light detected in the halo. Comparisons with the light distribution expected from simple thin+thick disk models, in which we have accounted for the whole range of galaxy inclinations and for the effective PSF, demonstrate that no exponential vertical disk component can yield the observed power-law shape of the SB profiles at  $r > 4 r_{\text{exp}}$  in any of the four considered bands. Adding a moderately flattened ( $c/a \sim 0.6$ ), power-law ( $I \propto r^{-2}$  or  $\rho \propto r^{-3}$ ) halo component to a simple exponential disk, it is possible to reproduce the basic features in the observed profiles quite well.

It could be argued, that the emission we detect in the outer regions is produced by small bulges. However, MacArthur, Courteau & Holtzman (2003) have

## 2 The stellar halo of disc galaxies

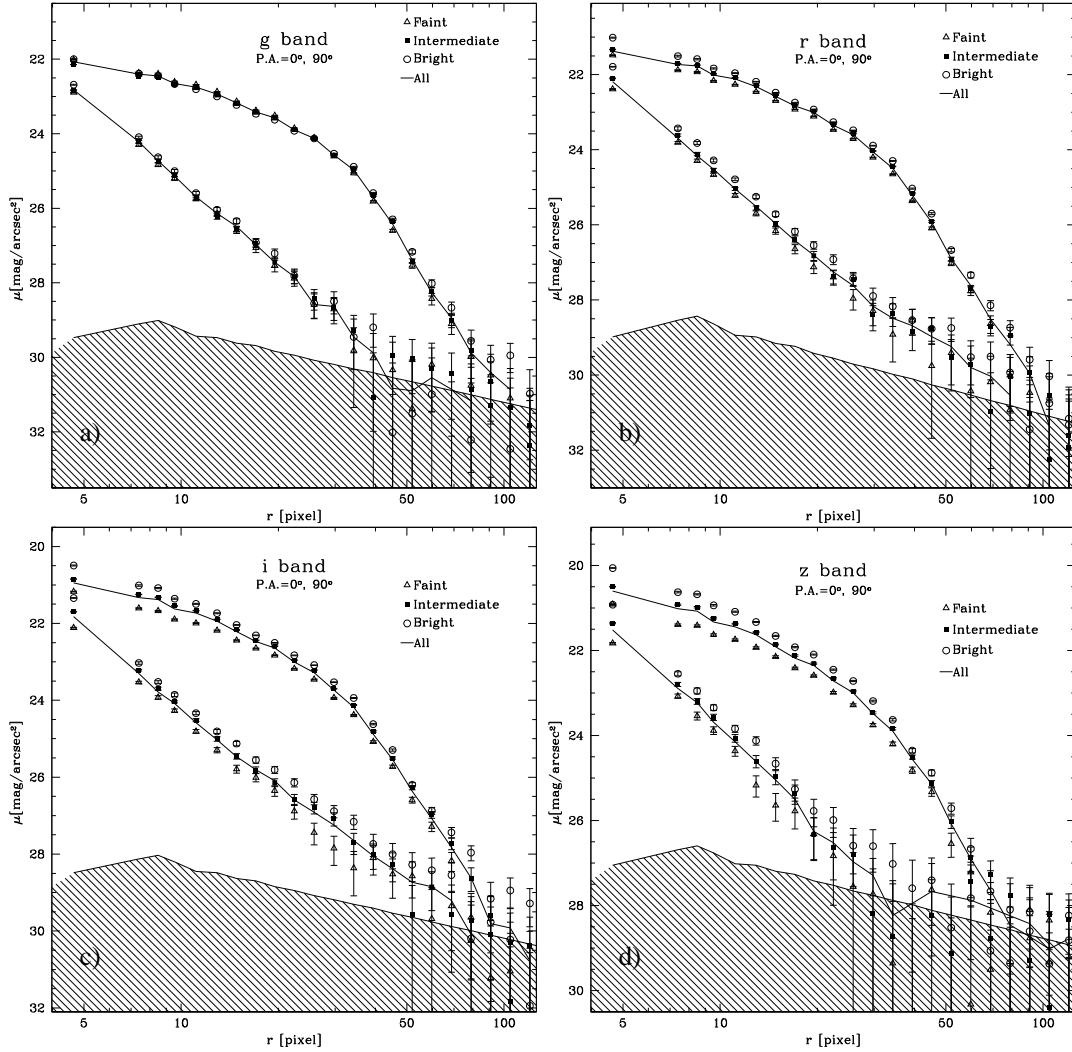


**Figure 2.8:** The stacked SB profiles in  $g$ ,  $r$ ,  $i$  and  $z$  band, at  $0^\circ$  (upper curves) and  $90^\circ$  PA (lower curves), for three luminosity bins: open triangles represent the ‘faint’ bin, filled squares the ‘intermediate’ and open circles the ‘bright’ one. The solid line is the all-sample profile. The shaded area is the rms background fluctuation.

shown that the bulges of disk-dominated galaxies, like the ones in our sample, are in general well represented by exponential laws with  $h_{\text{bulge}}/h_{\text{disk}} = 0.13 \pm 0.06$  ( $h_{\text{bulge}}$  and  $h_{\text{disk}}$  being the exponential scale-length of the bulge and of the disk respectively). Assuming an upper limit of  $\mu_r = 18 - 19 \text{ mag arcsec}^{-2}$  for the central surface brightness of the bulge, this implies that bulges con-

## 2.1 Haloes around edge-on disk galaxies in the Sloan Digital Sky Survey

---

tribute no more than 30 mag arcsec<sup>-2</sup> beyond 20 pixels. The light we have measured is thus not a simple outward extension of the small bulges often seen in late-type galaxies.

We have shown in Fig. 2.5 that the results obtained are independent of the scale-length adopted for rescaling the galaxies: this is a strong indication for the absence of any significant dependence of halo characteristics on the detailed shape of the disk SB profile, even if it does not necessarily imply complete homology of the disks in our sample.

These results are consistent with some known features of the Milky Way halo. Confirming previous results by Harris (1976), Zinn (1985) derived a halo stellar density declining as  $r^{-3.5}$  from the distribution of the globular clusters. Similar results were obtained from the RR Lyrae distribution by Saha (1985),  $\rho \propto r^{-3.5}$ , by Preston, Shectman & Beers (1991),  $\rho \propto r^{-3.2 \pm 0.1}$ , and by Ivezić et al. (2000),  $\rho \propto r^{-2.7 \pm 0.2}$ . The spatial distribution of Blue Horizontal Branch (BHB) stars (Preston et al. 1991; Kinman, Suntzeff & Kraft 1994) is in good agreement with those estimates, yielding  $\rho \propto r^{-3.5}$  at height  $z \gtrsim 5$  kpc  $\sim 2.5 r_{\text{exp}}$  above the disk plane. The SB provided by the MW halo stars is expected to be roughly of the order of 30 mag arcsec<sup>-2</sup> at  $r \sim 8$  kpc  $\sim 4 r_{\text{exp}}$  in V band (Binney & Merrifield 1998, par. 10.5), consistently with our measurements in *g* band. The analysis by Hartwick (1987) and by Preston et al. (1991), considering RR Lyrae and BHB stars, provides an estimate for moderate flattening of the spheroidal halo  $c/a \sim 0.6$ , which is also consistent with the findings in this work.

Comparisons with analogous studies of external galaxies are in general difficult. Although its small distance makes M31 the easiest target for observing of the halo population of a disk galaxy, the prominence of its bulge makes it hard to disentangle the density distribution of the halo so that it is perhaps more appropriate to talk about a generic spheroid. Pritchett & van den Bergh (1994) measured the SB of M31 spheroid to  $\mu_V \sim 30$  mag arcsec<sup>-2</sup> and concluded that it can be modelled either by a de Vaucouleurs law or, in its outer parts, by a power-law  $\rho \propto r^{-5}$ , which is much steeper than what we find. However, the globular cluster distribution follows  $\rho \propto r^{-3}$  (Racine 1991) and there is evidence for a shallower power-law index in the outer parts of the halo from more recent observations (Irwin, private communication).

Recent observations of the red giant stars of the nearby, late-type spiral M33 (Ferguson et al. 2003, in preparation), seem to exclude the presence of a spheroidal component around this galaxy, but its nearly face-on aspect makes it difficult to draw firm conclusions.

Results from more distant galaxies are even more uncertain, because of the overwhelming difficulties in going deeper than 28 mag arcsec<sup>-2</sup>. After the first

## 2 The stellar halo of disc galaxies

---

claim by Sackett et al. (1994) of the detection of halo emission from NGC5907, many discrepant measurements have been made by different groups in bands from the optical to the NIR (see e.g. Barnaby & Thronson 1994; Lequeux et al. 1996; Rudy et al. 1997; James & Casali 1998; Lequeux et al. 1998). The latest observations by Zheng et al. (1999) with intermediate-band filters, and by Yost et al. (2000) in optical and NIR, together with the RGB star counts derived by Zepf et al. (2000) from NICMOS observations, seem to rule out the presence of a halo, favouring instead a luminous ring produced by the tidal disruption of a dwarf companion.

However, despite the non-detection of any diffuse component in the Scd galaxy NGC 4244 by Fry et al. (1999), probably because of the low sensitivity of their observations ( $\mu_R < 27.5$  mag arcsec<sup>-2</sup>), many studies during the last years support the idea of a luminous envelope (thick disk or halo) surrounding many of disk galaxies. Morrison et al. (1997) detected thick disk emission from NGC 891; Abe et al. (1999) have measured  $R$  and  $I$  light excesses with respect to an exponential disk model in the Scd galaxy IC 5249; Wu et al. (2002) have observed NGC 4565 at 6600Å obtaining good accuracy photometry as faint as  $\mu = 27.5$  mag arcsec<sup>-2</sup> and found a halo component with power-law  $r^{-2.3--4.0}$ . Similar results are found by Rauscher et al. (1998) in the NIR  $K$  band for ESO 240-G11 (power-law halo  $\rho \propto r^{-3.5}$ ). After observing a sample of 47 extremely flat galaxies in  $B$ ,  $R$  and  $K_s$  down to extremely faint SB, Dalcanton & Bernstein (2002) have claimed the ubiquitous presence of red stellar envelopes around disk galaxies. It is not clear whether these envelopes extend to a spheroidal halo or are just thick disks, as the authors claim, because their detection limits are just at the surface brightness where we start to see our power-law halo component unambiguously

In order to establish the origins of these stellar populations, very precise colour measurements are needed. Due to the enormous observational difficulties, reliable colour measurements of the halos around disks are very scarce: excluding the MW, M31 and M33 for which colour-magnitude diagrams of halo stars and globular clusters can be obtained, the only optical colours available to now are the ones derived by Lequeux et al. (1998) for NGC 5907. Beside these, Dalcanton & Bernstein (2002) have measured  $(B - R)$  and  $(R - K_s)$  for the thick disks in their sample. The colours we derived in Sec. 2.1.4.4 are, in fact, very uncertain, both because of the intrinsic error of the measurements and because of the practical impossibility to avoid contributions from the disk component. The analysis in Sec. 2.1.4.4 showed that scattered light from the disk component is likely to affect the colours by a few hundredths of a mag, but colour excesses up to 0.2 mag cannot be ruled out. If we trust these results ( $g - r = 0.65 \pm 0.1$ ,  $r - i = 0.60 \pm 0.1$ ), we find that halos are made of stars which are only marginally ( $2\sigma$ ) consistent with old, moderately metal-poor

## 2.1 Haloes around edge-on disk galaxies in the Sloan Digital Sky Survey

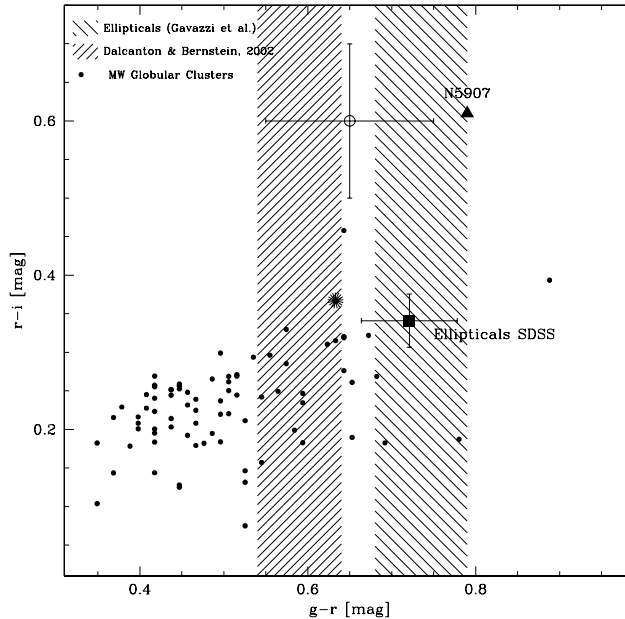


**Figure 2.9:** Comparison of the halo colours with other stellar systems in the  $(r-i)$  vs  $(g-r)$  diagram. The open circle with error-bars is our measurement, filled circles are the MW globular clusters from Harris (1996), the filled square with error-bar is the average  $\pm$  rms of the SDSS ellipticals at  $z = 0.05$  from Bernardi et al. (2003), and the triangle is the measure of NGC 5907 from Lequeux et al. (1998). The shaded areas represent the  $g-r$  range for the thick disks in Dalcanton & Bernstein (2002) and the interquartile range of the Virgo and Coma ellipticals from GOLDMiNe (Gavazzi et al. 2003, back slanted shading).

stellar populations. In Fig. 2.9 we compare the stacked halo  $g-r$ ,  $r-i$  colours with different data taken from the literature<sup>7</sup>. Our point (open circle with error bars) is almost inconsistent with the colours of the MW globular clusters (filled circles, from Harris 1996), being much redder in  $r-i$ , and as red as the metal-rich tail of the globular cluster distribution in  $g-r$ . We have highlighted 47 Tucanae in the plot (starred dot), because its integrated colours are very similar to M31's halo. Its  $g-r$  is about the same as our measurements. We note that  $g-r$  is also consistent with the blue end of the elliptical sequence as derived from the SDSS at the median redshift of the

<sup>7</sup>Photometric transformations between different standards are taken from Smith et al. (2002).

## 2 The stellar halo of disc galaxies

---

sample  $z = 0.05$  (filled square, Bernardi et al. 2003), and from the observations in Virgo and Coma by Gavazzi et al. in B and V, as given in GOLDMiNe (Gavazzi et al. 2003), whose interquartile range is represented by the backshaded area. Reasonable agreement is found with the optical colours  $B - R$  derived by Dalcanton & Bernstein (2002) for their thick disks (whose range is represented by the shaded area in Fig. 2.9). Reconciling the measured  $r - i$  colour with any known stellar population is almost impossible, even if we allow for an extreme 0.1 mag reddening caused by the PSF, as discussed in Sec. 2.1.4.4. It is however interesting to note that the colours derived for NGC 5907 by Lequeux et al. (1998) are consistent with ours, but nonetheless troublesome. We exclude significant dust reddening for two reasons. First, the unusually red colour in our data is  $r - i$ , despite the fact that dust mostly affects optical/blue bands. Second, in the  $r - i$  profile there is quite strong evidence for a red gradient toward the outer parts, whereas it is known that the dust is concentrated in a thin layer in the disk. Thus we conclude that there is evidence for the halos being made of extremely red stellar populations. This is likely to be primarily due to an old age, but other effects, such as high metallicity or ‘exotic’ low-mass dominated IMF, would be required in order to explain the unusually high  $r - i$ .

Our red colours seem to exclude the possibility that the majority of the halos we observe around disk galaxies are made of metal-poor stars, or that they result from the integrated light of globular cluster populations. The correlation between the disk and halo SB suggests a link between the two components. On the other hand, the high latitude extension of the emission rules out ‘disk heating’ as an effective formation mechanism. An accretion (or ‘cannibalism’) scenario, in which the halo is built up by capture and disruption of spheroidal satellites, presents many advantages in explaining the observations. In this scenario dwarf spheroidal galaxies, made of old, metal enriched stars, are tidally disrupted by the gravitational field of the central galaxy and their stars are spread to fill the phase space almost isotropically in a few dynamical times. Thus both the spheroidal shapes and the extremely red colours of the halos could be explained, at least qualitatively. As already mentioned, recent observations in the halo of MW and M31, of the Sagittarius stream in the MW, and of the ring in the halo of NGC 5907 support the idea that this mechanism has been working till very recent times and is not uncommon among the disk galaxies.

Our analysis in different luminosity bins shows that the halo luminosity, at least on average, is proportional to disk luminosity. Prominent halos are in the more luminous galaxies. The decrease of the average surface brightness

## 2.1 Haloes around edge-on disk galaxies in the Sloan Digital Sky Survey

---

at lower luminosity affects mostly the redder pass-bands and is reflection of the well known correlation of disk surface brightness with disk luminosity in the red bands (see e.g. Shen et al. 2003). The light we see does not appear to be a straightforward extension of the bulge, since the power-law shapes of the profiles, irrespective of luminosity, are not consistent with classical de Vaucouleurs or exponential bulges. We can interpret the halo-disk luminosity relation we find here in the hierarchical picture, in which more luminous galaxies sit in more massive DM halos, with a larger number of merging sub-halos contributing to the stellar halo luminosity. However, deeper and more detailed observations, along with more reliable theoretical predictions for the number, stellar mass and metal content of the accreted satellites, are needed in order to confirm this hypothesis.

### 2.1.6 Summary and conclusions

By stacking a large number ( $> 1000$ ) of edge-on disk galaxies imaged in the SDSS we have been able to detect a diffuse, spheroidal, low-surface brightness component around the disk. This detection is significant in the  $g$ ,  $r$ ,  $i$  and  $z$  bands, and cannot be ascribed to any obvious instrumental artifact (e.g. scattered light or PSF). Given the statistical estimator we adopt for combining the images, our result indicates that a substantial fraction of the stacked galaxies must share the observed halo characteristics, even if we cannot exclude the possibility that a number of disk galaxies actually have no halo at all. The halo can be described by a power-law projected density profile  $I \propto r^{-\alpha}$ , with  $\alpha \sim 2$  nearly irrespective of the band.

The colour measurements provide inconclusive and troublesome results, but there is a clear indication for extremely red colours.  $g - r$  is consistent with old, moderately metal-poor stellar populations, such as the more metal-rich MW's globular clusters, 47 Tucanae, the halo of M31 and the most metal-poor ellipticals.  $r - i$  is (at  $2 \sigma$ ) 0.2 mag redder than the reddest known stellar populations in globular clusters and elliptical galaxies and it is difficult to reconcile with any theoretical models, even allowing for *ad hoc* modified IMF's dominated by low-mass stars and high metallicity. The data also suggest a correlation between the luminosity of the halo and the total luminosity of the galaxy.

The results presented in this work are far from being conclusive, but nevertheless they are consistent with the idea that a large fraction of disk galaxies are surrounded by a luminous halo. The colours, although affected by large uncertainties, hint at old, but not particularly metal-poor stellar populations, thus supporting a scenario in which the halos are mostly contributed by stars

## 2 The stellar halo of disc galaxies

---

stripped from accreted or merged companions, in which the chemical evolution was already advanced.

Deeper, individual observations of a large sample of nearby galaxies will be required, however, in order to assess the validity of this scenario by quantifying not only the average halo, but also the whole distribution of individual halo parameters.

### Acknowledgements

We wish to thank the referees James Lequeux and Françoise Combes for helpful advice.

S.Z. wishes to thank Annette Ferguson, Stéphane Charlot, Amina Helmi and Tim McKay for the useful discussions.

Funding for the creation and distribution of the SDSS Archive has been provided by the Alfred P. Sloan Foundation, the Participating Institutions, the National Aeronautics and Space Administration, the National Science Foundation, the U.S. Department of Energy, the Japanese Monbukagakusho, and the Max Planck Society. The SDSS Web site is <http://www.sdss.org/>.

The SDSS is managed by the Astrophysical Research Consortium (ARC) for the Participating Institutions. The Participating Institutions are The University of Chicago, Fermilab, the Institute for Advanced Study, the Japan Participation Group, The Johns Hopkins University, Los Alamos National Laboratory, the Max-Planck-Institute for Astronomy (MPIA), the Max-Planck-Institute for Astrophysics (MPA), New Mexico State University, University of Pittsburgh, Princeton University, the United States Naval Observatory, and the University of Washington.

## Bibliography

- Abazajian K., et al. 2003, preprint(astro-ph/0305492)
- Abe F., et al. 1999, AJ, 118, 261
- Barnaby D., Thronson H. A., 1994, AJ, 107, 1717
- Baugh C. M., Cole S., Frenk C. S., 1996, MNRAS, 283, 1361
- Benson A. J., Baugh C. M., Cole S., Frenk C. S., Lacey C. G., 2000, MNRAS, 316, 107
- Bernardi M., et al. 2003, AJ, 125, 1882
- Bertin E., Arnouts S., 1996, A&AS, 117, 393
- Binney J., Merrifield M., 1998, Galactic astronomy. Princeton University Press, Princeton, NJ
- Blanton M. R., et al. 2002, preprint(astro-ph/0210215)
- Blanton M. R., Lin H., Lupton R. H., Maley F. M., Young N., Zehavi I., Loveday J., 2003, AJ, 125, 2276
- Dalcanton J. J., Bernstein R. A., 2002, AJ, 124, 1328
- Elson R. A. W., Fall S. M., Freeman K. C., 1987, ApJ, 323, 54
- Ferguson A. M. N., Irwin M. J., Ibata R. A., Lewis G. F., Tanvir N. R., 2002, AJ, 124, 1452
- Fry A. M., Morrison H. L., Harding P., Boroson T. A., 1999, AJ, 118, 1209
- Fukugita M., Ichikawa T., Gunn J. E., Doi M., Shimasaku K., Schneider D. P., 1996, AJ, 111, 1748
- Gavazzi G., Boselli A., Donati A., Franzetti P., Scodreggio M., 2003, A&A, 400, 451

## 2 The stellar haloes of disc galaxies

---

- Gunn J. E., et al. 1998, *AJ*, 116, 3040
- Harris W. E., 1976, *AJ*, 81, 1095
- Harris W. E., 1996, *AJ*, 112, 1487
- Hartwick F. D. A., 1987, in *NATO ASIC Proc. 207: The Galaxy The structure of the Galactic halo.* pp 281–290
- Helmi A., White S. D. M., de Zeeuw P. T., Zhao H., 1999, *Nature*, 402, 53
- Hogg D. W., Finkbeiner D. P., Schlegel D. J., Gunn J. E., 2001, *AJ*, 122, 2129
- Ibata R. A., Gilmore G., Irwin M. J., 1994, *Nature*, 370, 194
- Ibata R. A., Irwin M. J., Lewis G. F., Ferguson A. M. N., Tanvir N., 2003, *MNRAS*, 340, L21
- Ivezić Ž., et al. 2000, *AJ*, 120, 963
- James P. A., Casali M. M., 1998, *MNRAS*, 301, 280
- Kauffmann G., Colberg J. M., Diaferio A., White S. D. M., 1999, *MNRAS*, 303, 188
- Kauffmann G., Nusser A., Steinmetz M., 1997, *MNRAS*, 286, 795
- Kauffmann G., White S. D. M., Guiderdoni B., 1993, *MNRAS*, 264, 201
- Kinman T. D., Suntzeff N. B., Kraft R. P., 1994, *AJ*, 108, 1722
- Kregel M., van der Kruit P. C., de Grijs R., 2002, *MNRAS*, 334, 646
- Lequeux J., Combes F., Dantel-Fort M., Cuillandre J.-C., Fort B., Mellier Y., 1998, *A&A*, 334, L9
- Lequeux J., Fort B., Dantel-Fort M., Cuillandre J.-C., Mellier Y., 1996, *A&A*, 312, L1
- Lupton R. H., Gunn J. E., Ivezić Z., Knapp G. R., Kent S., Yasuda N., 2001, in *ASP Conf. Ser. 238: Astronomical Data Analysis Software and Systems X The SDSS Imaging Pipelines.* pp 269–+
- MacArthur L. A., Courteau S., Holtzman J. A., 2003, *ApJ*, 582, 689
- Majewski S. R., 1993, *ARA&A*, 31, 575

## 2.1 Haloes around edge-on disk galaxies in the Sloan Digital Sky Survey

---

- Morrison H. L., Miller E. D., Harding P., Stinebring D. R., Boroson T. A., 1997, *AJ*, 113, 2061
- Navarro J. F., Steinmetz M., 2000, *ApJ*, 538, 477
- Navarro J. F., White S. D. M., 1994, *MNRAS*, 267, 401
- Odenkirchen M., Grebel E. K., Dehnen W., Rix H., Cudworth K. M., 2002, *AJ*, 124, 1497
- Petrosian V., 1976, *ApJ*, 209, L1
- Pier J. R., Munn J. A., Hindsley R. B., Hennessy G. S., Kent S. M., Lupton R. H., Ivezić Ž., 2003, *AJ*, 125, 1559
- Preston G. W., Shectman S. A., Beers T. C., 1991, *ApJ*, 375, 121
- Pritchett C. J., van den Bergh S., 1994, *AJ*, 107, 1730
- Racine R., 1991, *AJ*, 101, 865
- Rauscher B. J., Lloyd J. P., Barnaby D., Harper D. A., Hereld M., Loewenstein R. F., Sevenson S. A., Mrozek F., 1998, *ApJ*, 506, 116
- Rudy R. J., Woodward C. E., Hodge T., Fairfield S. W., Harker D. E., 1997, *Nature*, 387, 159
- Sackett P. D., Morrison H. L., Harding P., Boroson T. A., 1994, *Nature*, 370, 441
- Saha A., 1985, *ApJ*, 289, 310
- Scannapieco C., Tissera P. B., 2003, *MNRAS*, 338, 880
- Schlegel D. J., Finkbeiner D. P., Davis M., 1998, *ApJ*, 500, 525
- Shen S., Mo H. J., White S. D. M., Blanton M. R., Kauffmann G., Voges W., Brinkmann J., Csabai I., 2003, preprint(astro-ph/0301527)
- Smith J. A., et al. 2002, *AJ*, 123, 2121
- Sommer-Larsen J., Gelato S., Vedel H., 1999, *ApJ*, 519, 501
- Somerville R. S., Primack J. R., 1999, *MNRAS*, 310, 1087
- Springel V., White S. D. M., Tormen G., Kauffmann G., 2001, *MNRAS*, 328, 726

## 2 The stellar haloes of disc galaxies

---

Stoughton C., et al. 2002, AJ, 123, 485

Strauss M. A., et al. 2002, AJ, 124, 1810

van der Kruit P. C., 2001, in ASP Conf. Ser. 230: Galaxy Disks and Disk Galaxies Truncations in Stellar Disks. pp 119–126

Wu H., et al. 2002, AJ, 123, 1364

Yanny B., Newberg H. J., Grebel E. K., Kent S., Odenkirchen M., Rockosi C. M., Schlegel D., Subbarao M., Brinkmann J., Fukugita M., Ivezić Z., Lamb D. Q., Schneider D. P., York D. G., 2003, ApJ, 588, 824

York D. G., et al. 2000, AJ, 120, 1579

Yost S. A., Bock J. J., Kawada M., Lange A. E., Matsumoto T., Uemizu K., Watabe T., Wada T., 2000, ApJ, 535, 644

Zepf S. E., Liu M. C., Marleau F. R., Sackett P. D., Graham J. R., 2000, AJ, 119, 1701

Zheng Z., et al. 1999, AJ, 117, 2757

Zinn R., 1985, ApJ, 293, 424

## 2.2 A faint red stellar halo around an edge-on disc galaxy in the Hubble Ultra Deep Field

Zibetti, S., & Ferguson, A.M.N., 2004, MNRAS, **352**, L6

### Abstract

We analyse the detailed structure of a highly-inclined ( $i \gtrsim 80^\circ$ ) disc galaxy which lies within the Hubble Ultra Deep Field (UDF). The unprecedented depth of the UDF data allow disc and extraplanar emission to be reliably traced to surface brightness levels of  $\mu_{V,i,z} \sim 29 - 30$  mag arcsec $^{-2}$  (corresponding to rest-frame equivalents of  $\mu_{g,r,i} \sim 28 - 29$  mag arcsec $^{-2}$ ) in this redshift  $z = 0.32$  system. We detect excess emission above the disc which is characterised by a moderately-flattened ( $b/a \sim 0.6$ ) power-law ( $I \propto R^{-2.6}$ ). The structure and colour of this component are very similar to the stellar halo detected in an SDSS stacking analysis of local disc galaxies (Zibetti, White, & Brinkmann 2004) and lend support to the idea that we have detected a stellar halo in this distant system. Although the peculiar colours of the halo are difficult to understand in terms of normal stellar populations, the consistency found between the UDF and SDSS analyses suggests that they cannot be easily discounted.

### keywords:

galaxies: haloes, galaxies: structure, galaxies: photometry, galaxies: spiral

### 2.2.1 Introduction

In the currently-favoured  $\Lambda$ CDM framework, galaxy formation proceeds hierarchically with small structures forming first and later merging and accreting to form large galaxies. In these models, a significant fraction the stars which reside in the stellar halo and thick disc are tidally-stripped from small satellites as they fall within the host potential (*e.g.* Abadi, Navarro, Steinmetz & Eke 2003). The structure, composition and ubiquity of these faint stellar components are thus expected to reflect the details of the galaxy assembly process (*e.g.* Bullock & Johnston 2004).

Observations of stellar haloes and thick discs in external galaxies are extremely challenging. These faint components typically have surface brightnesses  $\mu_R \gtrsim 28$  mag arcsec $^{-2}$ , which corresponds to  $\gtrsim 7$  magnitudes fainter than the sky. Measurements of diffuse emission require flat-fielding and sky subtraction uncertainties, as well as scattered light effects, to be significantly less than 0.1 per cent. Until recently, few observational constraints were available with which to confront models. While there have been some detections of faint stellar components in external galaxies (*e.g.* Sackett et al. 1994; Morrison et al. 1997; Lequeux et al. 1998; Abe et al. 1999), there have also been

## 2 The stellar haloes of disc galaxies

---

non-detections (*e.g.* Zheng et al. 1999; Fry et al. 1999), leading one to question to what extent the results reflect real variance as opposed to systematic effects (see Zibetti, White, & Brinkmann 2004, hereafter Z04, for a full discussion). The alternative technique of using wide-area resolved star counts to study stellar haloes sidesteps the difficulties inherent in quantifying extremely faint diffuse emission, but can only be applied to a handful of nearby galaxies (*e.g.* Ferguson et al. 2002).

Recently Z04 have conducted the first statistical study of stellar halo emission by stacking  $\gtrsim 1000$  homogeneously rescaled edge-on galaxies from the Sloan Digital Sky Survey (SDSS). This technique has allowed quantitative analysis of the “mean” stellar halo to  $\mu_r \sim 31$  mag arcsec<sup>-2</sup>. These authors find a halo characterised by a moderately-flattened ( $b/a \sim 0.6$ ) power-law ( $I \propto R^{-2}$ ) and puzzling colours ( $g - r = 0.65$ ,  $r - i = 0.6$ ) that cannot be easily explained by normal stellar populations. The detection of flatter red stellar envelopes around extreme late-type edge-on disc galaxies by Dalcanton & Bernstein (2002) may represent the higher surface brightness regions of these haloes.

The recent release of the Hubble Ultra Deep Field (UDF), a public survey carried out with the Advanced Camera for Surveys using Director’s Discretionary time in Cycle 12 (Beckwith, Somerville & Stiavelli 2003), provides a rare opportunity to quantitatively study galaxy structure to the depths where halo emission should prevail. This *Letter* reports the detection of a faint red stellar halo around a  $z = 0.32$  edge-on galaxy in the UDF.

### 2.2.2 Observations and Analysis

The Hubble Ultra Deep Field (UDF) consists of 400 orbits of integration on a single 11.3 arcmin<sup>2</sup> field lying within the Chandra Deep Field South GOODS area, centred at RA= 03<sup>h</sup>32<sup>m</sup>39.0, Dec= -27°47′29″.1 (J2000). Four filters have been utilised: *B*(F435W), *V*(F606W) (each for 56 orbits, 37.5 hours) and *i*(F775W), *z*(F850LP) (each for 144 orbits, 96.4 hours). The UDF represents the deepest observations yet obtained with HST, or any ground-based telescope.

We focus on a relatively large, well-formed disc galaxy located at RA= 03<sup>h</sup>32<sup>m</sup>41.1, Dec= -27°48′52″.9 (J2000). This galaxy is clearly detected in all 4 bands and is identified with source #31611 at  $z = 0.322$  in the COMBO-17 photometric redshift survey of Wolf et al. (2004). The high inclination of this system makes it an ideal target for a study of faint extraplanar emission. At this redshift, 1 arcsec=4.7 kpc and the lookback time is 3.6 Gyr<sup>8</sup>. We note the

---

<sup>8</sup>For  $H_0=70$ km sec<sup>-1</sup> Mpc<sup>-1</sup>,  $\Omega_0=1$ ,  $\Omega_\Lambda=0.7$

## 2.2 A faint red stellar halo around an edge-on disc galaxy in the Hubble Ultra Deep Field

presence of a ring-like structure of blue knots lying along the western major axis (see Fig. 2.10(a)); this structure has a photometric redshift of unity according to Wolf et al. (2004) and thus appears as a chance alignment.

Our analysis is based on the reduced UDF data v1.0 released to the community by STScI on March 9, 2004<sup>9</sup>. The data were pre-processed using the standard ACS/WFC pipeline and subsequently combined using the Multidrizzle package. The observations were obtained using a 4-point dither pattern to provide sub-pixel sampling, as well as a larger-scale pattern to cover the 2 arcsec gap between the ACS/WFC chips. The final pixel scale after drizzling is 0.6 of the original, corresponding to 0.03 arcsec. Note that all magnitudes are on the *AB*-system with zero-points provided by STScI. We have additionally applied a correction for Galactic extinction using Schlegel et al. (1998).

Using the geometric parameters obtained from *STSDAS-ellipse* fitting of the *i*-band isophotes, we have extracted  $1200 \times 1200$  pixel<sup>2</sup> frames in each band, centred on the galaxy and rotated according to the average position angle of the isophotes at  $\mu_i \sim 24$  mag arcsec<sup>-2</sup>. The RGB colour composite image of the galaxy is shown Fig. 2.10 (a), where we use the *B*-band image for the blue channel, *V* for the green, and *i* + *z* for the red.

We use SExtractor v2.3 (Bertin & Arnouts 1996) to extract very low signal-to-noise segmentation images of the frames, adopting a  $5 \times 5$  pix<sup>2</sup> gaussian smoothing kernel ( $\sigma = 2$  pixels), a  $1\text{-}\sigma$  detection threshold and a 25 pixel minimum detection area. After excluding the segment(s) corresponding to the galaxy and manually editing the mask to include sources that were not correctly deblended from the galaxy, we combine the masks in the four bands and “grow” the resulting mask by 2 pixels, in order to have better coverage of the extended diffuse sources. The masked *i* + *z*-band image is shown in Fig. 2.10 (b), with an enhanced contrast in order to show the lowest intensity levels.

Visual inspection indicates that the galaxy is close to edge-on and this is confirmed by the measured isophotal axial ratio of 0.2 at  $\mu_i \sim 24$  mag arcsec<sup>-2</sup>. Assuming the standard formula for an infinitely thin disc ( $\cos i = b/a$ ), this corresponds to an inclination of 78°. For the more realistic case of finite thickness, the inclination will be somewhat greater than this. Fig. 2.10 a) also suggests a late-type classification for the galaxy based on prominent star-forming spiral arms, a significant amount of dust in the inter-arm region and a very small bulge, if present at all. In Fig. 2.10 b), one can clearly see the presence of red extraplanar emission which will be analysed in significant detail in the following section.

Although the UDF science images are already background subtracted, we

---

<sup>9</sup>Available from <http://www.stsci.edu/hst/udf/release>

## 2 The stellar haloes of disc galaxies

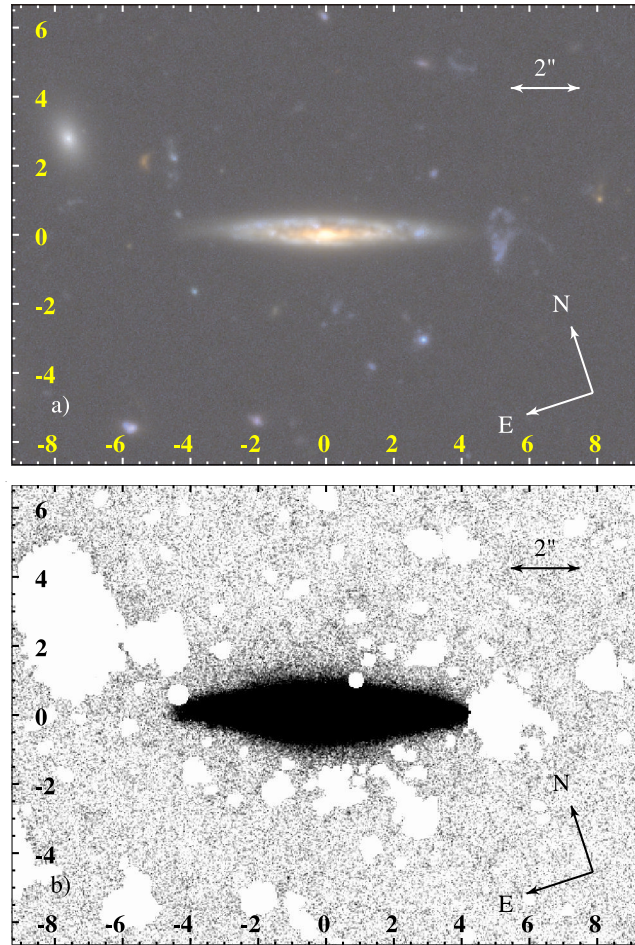


**Figure 2.10:** a) Full resolution colour composite RGB (( $i+z$ )- $V$ - $B$ ) image of the galaxy showing whole dynamic range. b)  $i+z$  band inverted gray-scale image, with enhanced contrast in the low surface brightness levels and masked regions superposed. Intensity scaling is a square root function in both panels. Axes show the offset in arcseconds with respect to the galaxy centre.

estimate and subtract the residual average local background using an annulus (inner radius= 400 pixels or 56 kpc, width = 200 pixels or 28 kpc) around the galaxy on the masked images . This annulus is chosen to lie outside the region where we might reasonably expect faint halo emission to be present. The maximum correction corresponds to a surface brightness of  $\sim 31$  mag arcsec $^{-2}$  (measured in the  $z$ -band); comparison to the faintest measured  $z$ -band surface brightness indicates that the level of uncertainty due to the

## 2.2 A faint red stellar halo around an edge-on disc galaxy in the Hubble Ultra Deep Field

background is no more than 20%. Smaller background uncertainties are found in all other bands.

The primary photometric analysis is performed on the masked images using an in-house developed C code which provides us with the average pixel value as a function of radius within a wedge-shaped region with apex located at the galaxy centre. As we believe the galaxy is close to edge-on, this technique provides an alternative to making simple major and minor axis cuts and is particularly well-suited to the study of very faint emission at large radius since relatively more pixels are averaged in these parts. Errors are attached by taking into account both the count statistics and the typical rms background fluctuations occurring on the same scale as the aperture. The latter quantity is computed by evaluating the surface brightness in a number of non-overlapping apertures spread throughout the frame and located at least 400 pixels from the centre of the galaxy.

### 2.2.3 Results

In Fig. 2.11 and 2.12, we show the surface brightness profiles measured along the major and minor axes of the galaxy respectively. As described in the legend, the different coloured symbols correspond to the four bands. The asymmetry seen in the inner regions of both profiles attests to the presence of spiral structure and dust lanes in these parts. We include these regions for completeness, but note their interpretation is complicated; our main focus is the behaviour of the profiles at very large radius.

The major axis profile is extracted using wedges aligned with the  $+x$  and  $-x$ -axes and with a small opening angle of  $10^\circ$  (see Fig. 2.11). While a warp is present in the outer parts of the disk, our extraction method involves summing over many pixels at large radius and is thus not significantly affected by the deviation from the midplane. In all four bands, the profile shows a profound change in slope at  $\sim 3$  arcsec. By fitting an exponential function to the surface brightness profile of the bright inner disc (corresponding to the region where highly structured spiral arms and dust lanes are visible in Fig.2.10), we find that the projected scalelength varies with wavelength from  $r_{\text{inner},B} = 4.2$  arcsec to  $r_{\text{inner},z} = 1.3$  arcsec. The steeper outer profile is very similar in all bands, with exponential scalelength of  $\sim 0.55$  arcsec. Beyond 5 arcsec an excess with respect to the exponential profile is seen in the three reddest bands at the level of  $\mu \sim 29 - 30$  mag arcsec $^{-2}$ .

The minor axis profile is extracted using wedges aligned with the the  $+y$  and  $-y$ -axes and with a wider opening angle of  $45^\circ$  in order to ensure adequate S/N far from the disc plane (see Fig. 2.12). On the southern side of the galaxy, the inner profile is more regular and declines as a smooth exponential until

## 2 The stellar haloes of disc galaxies

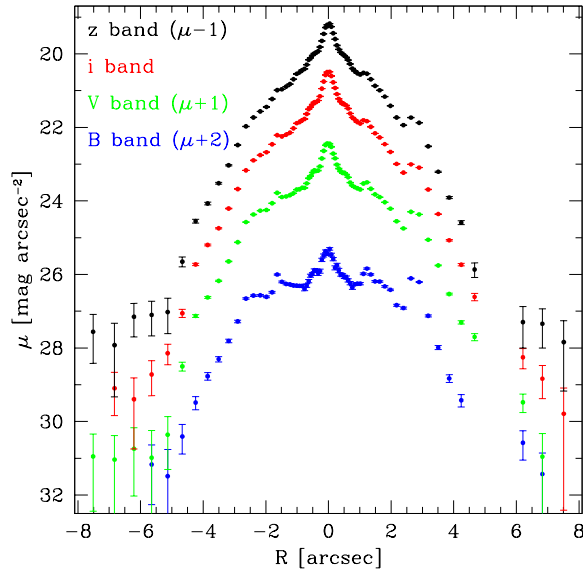


**Figure 2.11:** Major axis surface brightness profiles. Negative  $R$  are used for the eastern side, positive for the western. Error bars are computed as explained in the text. Only points with  $S/N > 1$  are plotted. The profiles for the different bands are coded in different colours and offset in order to avoid confusion, as indicated in the legend.

approximately 0.5 arcsec. Beyond 1 arcsec, a significant power-law excess is apparent (on both sides of the plane) in all four bands (see Fig. 2.12). The slope of this power-law component is measured to be  $\sim 2.6$  in the three reddest bands; we expect the effect of dust (as well as emission from an inclined disc) to be minimal at these heights ( $\gtrsim 5$  kpc) from the midplane.

We have checked that the point spread function (PSF) does not have a significant effect on our derived profiles by studying the surface brightness profile of a relatively bright, unsaturated star ( $m_V \sim 20.5$  mag) which falls within the UDF. We find that the surface brightness drops by  $\gtrsim 10(12)$  mag arcsec $^{-2}$  from the centre to 1 (2) arcsec in all bands. As a result, scattered light from the central PSF should be well below our measurement uncertainties.

In order to estimate the isophotal ellipticity of the power-law component, we measure the surface brightness as a function of radius in narrow wedges ( $13^\circ$  wide) placed at different position angles. By comparing surface brightnesses as a function of position angle out to a radius of 5.5 arcsec, we derive an axial ratio of  $b/a \sim 0.45$  in the  $i$ -band at  $\mu_i \sim 29$ . The outermost isophotes thus appear significantly rounder than the inner (disc-dominated) isophotes. Our

## 2.2 A faint red stellar halo around an edge-on disc galaxy in the Hubble Ultra Deep Field

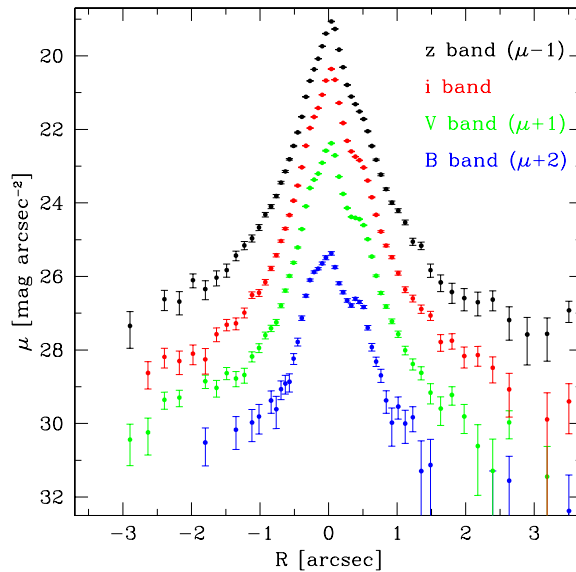


**Figure 2.12:** Same as Fig.2.11 for the minor axis. Negative  $R$  are used for the southern side, positive for the northern.

measurement represents a lower limit on the actual flattening however, since low-level disc emission may still contaminate the isophotes at 0 and  $180^\circ$ . Indeed, if we exclude the sectors which lie within  $25^\circ$  of the major axis, the ellipticity  $b/a$  of the faint outer component increases to 0.6.

In Fig. 2.13 we plot the  $V - i$  and  $i - z$  colours along the major (black solid line) and minor axes (red points) as obtained from combining the surface brightness profiles shown in Figures 2.11 and 2.12. The major axis profile represents the average of the eastern and western axes in regions where  $S/N > 2$ . Error bars are attached using the standard propagation of the errors on the surface brightness measurements. The profiles along the major axis display a clear blue gradient in  $V - i$  within  $\sim 2.5$  arcsec, where the bright disc dominates. Beyond  $\sim 3$  arcsec, where the exponential slope significantly steepens, the gradient in this colour is inverted. The  $i - z$  profile is significantly flatter, slowly varying from 0.3–0.35 in the inner 1 arcsec, to 0.15 at 4 arcsec. For the minor axis, the north and south sides are shown separately as filled circles and open diamonds respectively. Along the minor axis we observe a clear blue gradient in  $V - i$  within  $\sim 0.5$  arcsec, while the  $i - z$  profile in this region is very irregular and likely reflects both internal structure as well as dust within the disc. The transition between the disc and power-law regions is characterised by a strong red gradient in  $i - z$ , from 0.4 at 0.5 arcsec to 0.7

## 2 The stellar haloes of disc galaxies

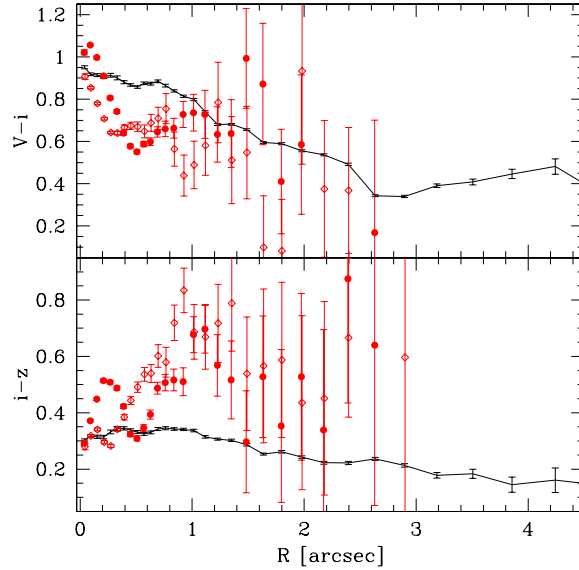


**Figure 2.13:** Colour profiles:  $V - i$  (top),  $i - z$  (bottom). Black solid lines represent the major axis and red points represent the minor axis (filled circles for the northern side, open diamonds for the southern). See text for details.

at 1 arcsec (considering the average of the northern and southern profiles). In the region dominated by the power-law excess ( $R \gtrsim 1.5$  arcsec), the colour measurements are rather noisy due to the very low surface brightness, but still there is evidence for  $V - I \sim 0.6 - 0.7$  and  $i - z \sim 0.5 \pm 0.1$ .

We also estimate the total magnitude of the galaxy, of the disc alone, and of the galaxy excluding the disc in each band (see Table 2.2). The total magnitude is integrated in an ellipse with  $b/a = 0.6$ ,  $a = 8$  arcsec, while for the disc alone we adopt an ellipse with  $b/a = 0.2$ ,  $a = 4.8$  arcsec. The “Total–Disc” magnitude is integrated in the complementary region. Typical uncertainties are of order of 0.05 for the “Total–Disc”, essentially given by count statistics and background uncertainty. In the three reddest bands the contribution of the non-disc component ranges from 4.3 to 5.6 per cent of the total light and displays colours which are significantly redder than those of the disc, namely  $V - i = 0.73 \pm 0.10$  vs. 0.64 and  $i - z = 0.52 \pm 0.10$  vs. 0.33. Reddening due to dust is unlikely to affect the colours at these radii and, in any case, any realistic distribution of dust would lead to bluer colours with increasing distance from the disc instead of redder ones.

## 2.2 A faint red stellar halo around an edge-on disc galaxy in the Hubble Ultra Deep Field

**Table 2.2:** Integrated photometry and colours: the total and disc fluxes are integrated in elliptical apertures, as described in the text. For the “Disc” and “Total–Disc” components, the percentage over the total flux are given as well.

	$V$		$i$		$z$		$V - i$	$i - z$
	mag	%	mag	%	mag	%	mag	mag
Total	21.14		20.50		20.16		0.64	0.34
Disc	21.18	95.7%	20.55	95.4%	20.23	94.4%	0.64	0.33
Total–Disc	24.54	4.3%	23.82	4.6%	23.30	5.6%	0.73	0.52

### 2.2.4 Discussion

Our analysis of the UDF galaxy, COMBO-17 #31611, has yielded the detection of a very low surface brightness structural component in addition to the bright disc. The main evidence for this component is: *i*) excess emission with respect to an exponential profile detected to 3 arcsec ( $\sim 14$  kpc) from the disc plane at the level of  $\mu_{V,i} \sim 29$  mag arcsec $^{-2}$ ; *ii*) the isophotal shape is centrally-concentrated and becomes rounder with increasing radius, reaching  $b/a \sim 0.6$  at the faintest measured isophote; *iii*) colours far from the plane that are distinct from the disc, *i.e.*  $i - z \sim 0.5$  and  $V - i \sim 0.7$  which are 0.2–0.3 and 0.1 mag redder than the disc respectively. Based on these properties, we attribute this component to the stellar halo of the galaxy, making it the most distant detection of a stellar halo yet known. We note the striking resemblance between the halo properties derived here and those of the “mean” halo detected in Z04’s SDSS stacking analysis. As discussed in Z04, these observations are also consistent with the few extant observations of individual stellar haloes.

The surface brightness profile of the halo is consistent with a power-law falling as  $I \propto R^{-2.6}$ . This slope must be considered an upper limit since if there is contaminating outer disc emission within our aperture, it will steepen the observed profiles even beyond 1 arcsec. An  $R^{1/4}$  law provides a poor fit to the data, which display excess emission at the faintest surface brightness levels compared to this profile. Less concentrated Sérsic profiles, which are more appropriate for the small bulges of late-type galaxies, provide even worse fits, thus ruling out the bulge as responsible for the measured emission. The fractional contribution of the halo to the total galaxy light is around 5 per cent, but this should be considered only approximate since we neglect disc contamination in the region where the halo light is integrated and include the inner halo as part of the disc light. Furthermore, we have no handle on internal extinction which could be significant in the inner regions of the galaxy, where the disc contribution is calculated.

## 2 The stellar haloes of disc galaxies

---

In order to conduct a direct comparison between the surface brightness and colours of this distant stellar halo and those of local galaxies, corrections need to be applied for bandpass shifting and surface brightness dimming. Given the photometric redshift of 0.322, the four observed bands,  $BViz$  correspond rather well to the SDSS  $ugri$  bands at redshift zero. Assuming a 9 Gyr,  $Z = 0.4Z_{\odot}$  single stellar population (SSP), we use the Bruzual & Charlot (2003) (hereafter BC03) models to calculate that observed surface brightnesses in  $Viz$  translate into rest-frame values of  $\sim 1.1$  mag arcsec $^{-2}$  brighter in  $gri$ . Our measurements of  $\mu_{V,i,z} \sim 29 - 30$  mag arcsec $^{-2}$  thus correspond to rest-frame equivalents of  $\mu_{g,r,i} \sim 28 - 29$  mag arcsec $^{-2}$ . This is precisely the surface brightness range in which a power-law halo component starts to dominate the minor axis profile in Z04’s SDSS stacking analysis and in which direct detections of individual haloes have been made in nearby galaxies.

We proceed to use the BC03 models to interpret the colours of the halo emission in terms of stellar populations. First, we compare the observed colours with predictions for different SSPs with ages of 2–13 Gyr and metallicities of 0.005–2.5  $Z_{\odot}$  adopting a Chabrier (2003) Initial Mass Function (IMF). We find none of these models can simultaneously reproduce the intermediate  $V - i$  and the very red  $i - z$  colours. Unless a super-solar metallicity is assumed ( $Z = 2.5Z_{\odot}$ ), the measured  $i - z \sim 0.5$  is at least 0.15 mag redder than the models and thus inconsistent at more than the 1.5  $\sigma$  level. Such an anomaly is reminiscent of the finding of a correspondingly high  $r - i \sim 0.6$  by Z04, despite the intermediate  $g - r \sim 0.65$  that could be accounted for by an old population with roughly solar metal enrichment.

Since we have been unable to produce a model that provides a good fit to the observed colours at  $z = 0.32$ , we adopt the following strategy to derive rest-frame colours that can be compared to haloes in the local universe. We adopt a fiducial reference model of an SSP of age 9 Gyr at the redshift of the galaxy, with  $Z = 0.4 Z_{\odot}$ , and a Chabrier IMF (BC03); this model minimises the absolute deviations from the observed colours. We then evolve the spectrum to  $z = 0$  and derive the rest-frame colours that would be observed through SDSS  $gri$  passbands. These colours can then be directly compared to the measurements of Z04 for the “mean” halo in their SDSS stack. Not unexpectedly, the evolved colours do not provide a good match to Z04’s observations but interestingly the offset between the model and observations is of the same magnitude and sense at  $z = 0$  as at  $z = 0.32$ . Specifically, while the model predicts a blue colour ( $V - i$  or SDSS  $g - r$ ) that is consistent or just slightly redder than the observations, the predicted red colour ( $i - z$  or SDSS  $r - i$ ) is too blue by  $\sim 0.2$  mag.

This kind of colour anomaly, *i.e.* too much flux in the spectral region around 7500Å with respect to shorter optical wavelengths, was also seen in the stellar

## 2.2 A faint red stellar halo around an edge-on disc galaxy in the Hubble Ultra Deep Field

---

halo of the nearby system NGC 5907 Lequeux et al. (1998). An attempt to directly resolve the population of metal-rich giant stars that would give rise to these red colours was unsuccessful, leading to the suggestion that the stellar halo in NGC 5907 formed with a non-standard IMF that is dominated by  $M \lesssim 0.2M_{\odot}$  stars (Zepf et al. 2000). While such a truncation could account for the lack of halo giant stars, it is unclear whether it could also explain the colours observed here, *i.e.*  $g - r$  typical of G-K stars yet  $r - i$  typical of M stars. Another possibility is that the red colour is contaminated by ionised gas emission. Deep  $H\alpha$  imagery of nearby galaxies often reveals faint extraplanar emission (Ferguson, Wyse, & Gallagher 1996; Miller & Veilleux 2003), however little is known about the extent of these ionised “haloes” at very faint flux levels. Further investigation is clearly required in order to understand the origin of the peculiar halo colours, which have now been measured in three independent studies.

As a final remark, we note that the surface brightness profile of the disc can be fitted by an exponential function that changes scalelength abruptly at 3 arcsec  $\simeq$  14 kpc (corresponding to  $\sim 2.4$  inner scalelengths). This behaviour is consistent with deep imaging studies of both edge-on and face-on discs in the local universe (Kregel et al. 2002; Pohlen et al. 2002) and likely reflects a truncation of the bright inner disc. That this radius also represents the point where the major axis colour gradient reverses and starts to redden is intriguing and suggests that the stellar populations at the far extremity of the disc are of significant age.

### Acknowledgements

We thank the referee, Michael Pohlen, for useful comments. The research of AMNF has been supported by a Marie Curie Fellowship of the European Community under contract number HPMF-CT-2002-01758.

## 2 The stellar haloes of disc galaxies

---

## Bibliography

- Abadi, M. G., Navarro, J. F., Steinmetz, M., & Eke, V. R. 2003, *ApJ*, 597, 21
- Abe F., et al., 1999, *AJ*, 118, 261
- Beckwith S., Somerville R., Stiavelli M., 2003, *STSci Newsletter*, Vol 20, Issue 04, p1
- Bertin E., Arnouts S., 1996, *A&AS*, 117, 393
- Bruzual G., Charlot S., 2003, *MNRAS*, 344, 1000 (BC03)
- Bullock, J. S. & Johnston, K. V. 2004, in proceedings of “Satellites and Tidal Streams”, eds. F. Prada, D. Martinez-Delgado & T. Mahoney, *astro-ph/0401625*
- Chabrier G., 2003, *PASP*, 115, 763
- Dalcanton J. J., Bernstein R. A., 2002, *AJ*, 124, 1328
- Ferguson, A. M. N., Wyse, R. F. G., & Gallagher, J. S. 1996, *AJ*, 112, 2567
- Ferguson A. M. N., Irwin M. J., Ibata R. A., Lewis G. F., Tanvir N. R., 2002, *AJ*, 124, 1452
- Fry A. M., Morrison H. L., Harding P., Boroson T. A., 1999, *AJ*, 118, 1209
- Kregel M., van der Kruit P. C., de Grijs R., 2002, *MNRAS*, 334, 646
- Lequeux J., Combes F., Dantel-Fort M., Cuillandre J.-C., Fort B., Mellier Y., 1998, *A&A*, 334, L9
- Miller, S. T. & Veilleux, S. 2003, *ApJS*, 148, 383
- Morrison H. L., Miller E. D., Harding P., Stinebring D. R., Boroson T. A., 1997, *AJ*, 113, 2061
- Pohlen M., Dettmar R.-J., Lütticke R., Aronica G., 2002, *A&A*, 392, 807

## 2 The stellar haloes of disc galaxies

---

Sackett P. D., Morrison H. L., Harding P., Boroson T. A., 1994, *Nature*, 370, 441

Schlegel D. J., Finkbeiner D. P., Davis M., 1998, *ApJ*, 500, 525

Wolf, C., et al. 2004, *A&A* submitted, astro-ph/0403666

Zepf S. E., Liu M. C., Marleau F. R., Sackett P. D., Graham J. R., 2000, *AJ*, 119, 1701

Zheng Z., et al., 1999, *AJ*, 117, 2757

Zibetti S., White S. D. M., Brinkmann J., 2004, *MNRAS*, 347, 556 (Z04)

*If a man will begin with certainties, he shall end  
in doubts; but if he will be content to begin with  
doubts he shall end in certainties.*

Sir Francis Bacon

# 3

## The optical emission from intracluster stars at $z \sim 0.25$

### Intergalactic stars in $z \sim 0.25$ galaxy clusters: systematic properties from stacking of Sloan Digital Sky Survey imaging data

Zibetti, S., White, S.D.M., Schneider, D.P., and Brinkmann, J., MNRAS  
submitted

#### Abstract

We analyse the spatial distribution and colour of the intracluster light (ICL) in 683 clusters of galaxies between  $z = 0.2$  and  $0.3$ , selected from  $\sim 1500 \text{ deg}^2$  of the first data release of the Sloan Digital Sky Survey (SDSS-DR1). Surface photometry in the  $g$ ,  $r$  and  $i$  bands is conducted on stacked images of the clusters, after rescaling them to the same metric size and masking out resolved sources. We are able to trace the average surface brightness profile of the ICL out to  $700 \text{ kpc}$ , where it is less than  $10^{-4}$  of the mean surface brightness of the dark night sky. The ICL appears as a clear surface brightness excess with respect to an inner  $R^{1/4}$  profile which characterises the mean profile of the brightest cluster galaxies (BCG). The surface brightness of the ICL ranges from  $27.5 \text{ mag arcsec}^{-2}$  at  $100 \text{ kpc}$  to  $\sim 32 \text{ mag arcsec}^{-2}$  at  $700 \text{ kpc}$  in the observed  $r$ -band. This corresponds SB in the range  $26.5$  to  $31$  in the rest-frame  $g$ -band. We find that, on average, the ICL contributes only a small

fraction of the total optical emission in a cluster. Within a fixed metric aperture of 500 kpc, this fraction is  $10.9 \pm 5.0$  per cent for our clusters. A further  $21.9 \pm 3.0$  per cent is contributed on average by the BCG itself. The radial distribution of the ICL is more centrally concentrated than that of the cluster galaxies, but the colours of the two components are identical within the statistical uncertainties. In the mean the ICL is aligned with and *more flattened* than the BCG itself. This alignment is substantially stronger than that of the cluster light as a whole. We find the surface brightness of the ICL to correlate both with BCG luminosity and with cluster richness, while the fraction of the total light in the ICL is almost independent of these quantities. These results support the idea that the ICL is produced by stripping and disruption of galaxies as they pass through the central regions of clusters. Our measurements of the diffuse light also constrain the faint-end slope of the cluster luminosity function. Slopes  $\alpha < -1.35$  would imply more light from undetected galaxies than is observed in the diffuse component.

**Keywords:**

galaxies: clusters: general; galaxies: elliptical and lenticular, cD; diffuse radiation; galaxies: interactions; galaxies: evolution; galaxies: formation

## 3.1 Introduction

Firstly proposed by Zwicky (1951), the presence of a diffuse population of intergalactic stars in galaxy clusters is now a well established observational fact. After pioneering work in the 1970s based on photographic plates (e.g. Welch & Sastry 1971) and photoelectric detectors (Melnick, Hoessel, & White 1977), CCD detectors have made it possible to conduct deep surveys in nearby galaxy clusters and to detect unambiguously the intracluster light (ICL) (e.g. Bernstein et al. 1995; Gonzalez et al. 2000; Feldmeier et al. 2002, 2004b; Gonzalez, Zabludoff, & Zaritsky 2004). Parallel searches for resolved intracluster stars (Durrell et al. 2002) and planetary nebulae (e.g. Arnaboldi et al. 1996; Feldmeier et al. 2004c) have confirmed the presence of a population of stars which are not dynamically bound to any individual galaxy, but orbit freely in the cluster potential. The ICL contributes a substantial fraction of the optical emission in a cluster. Estimates range from approximately 50 per cent in the core of the Coma cluster (Bernstein et al. 1995, although an upper limit of 25 per cent was found over a larger region by Melnick, Hoessel, & White 1977), to 10–20 per cent in less massive clusters (Feldmeier et al. 2004b). Arclets and other morphologically similar low surface brightness features have been identified by several authors in the Coma and Centaurus clusters (Gregg & West 1998; Trentham & Mobasher 1998; Calcáneo-Roldán et al. 2000), suggesting that at least part of the ICL is contributed by dynamically young tidal

features. This supports the commonly accepted idea that this stellar population is made up of disrupted dwarf galaxies and of stars stripped from more massive galaxies.

We are still far from a complete understanding of the physical mechanisms that produce the ICL. Several mechanisms can act to remove stars from individual galaxies and to fling them into intergalactic space. The relative importance and effectiveness of these mechanisms can vary during the evolutionary history of a cluster and from place to place within the cluster. Tides generated by the cluster potential (Merritt 1984) and repeated high speed encounters between galaxies (Richstone 1976) are the dominant stripping mechanisms in a fixed cluster potential, as demonstrated graphically by the simulations of Moore et al. (1996). However, when the evolution of the cluster and the presence of substructures is taken into account, two other mechanisms become relevant (Gnedin 2003). Preprocessing of the ICL occurs during low velocity encounters between galaxies within the groups which eventually merge into the cluster, and galaxies are dynamically heated by encounters with substructures. As stressed by Mihos (2004), the tidal tails and the heated structures preprocessed within groups are subsequently easily removed by the cluster potential.

In order to encompass all these processes in a cosmologically motivated framework, many groups in recent years have addressed the ICL problem using high resolution N-body simulations (Napolitano et al. 2003), some including smoothed particle hydrodynamics (SPH) to take gas processes into account (Murante et al. 2004; Willman et al. 2004; Sommer-Larsen, Romeo, & Portinari 2004). Although many issues still have to be clarified and agreement between the different models is far from complete, these simulations show how the ICL may be produced over the entire history of the clusters from continuous stripping of member galaxies and through contributions from merging groups. Unfortunately the degree to which they correctly represent the internal structure of cluster galaxies and their dark matter haloes is too uncertain for their prediction for the amount of ICL to be reliable.

Although the number of observations of the ICL in individual clusters has increased rapidly in recent years, we still lack a large sample that allows generalisation of the properties of the ICL and an understanding of how they depend on global cluster properties, particularly on richness and on the luminosity of the first ranked galaxy. Given the very low surface brightness of the ICL, typically less than 0.1 per cent of that of the night sky, observations are extremely challenging. Not only are long exposure times required in order to obtain acceptable signal-to-noise (S/N) ratios, but many subtle instrumental

### 3 The optical emission from intracluster stars at $z \sim 0.25$

---

effects, such as flat fielding inhomogeneities and scattered light within the camera, must be kept under tight control.

An alternative approach, which exploits the wealth of imaging data made available by the Sloan Digital Sky Survey (SDSS, York et al. 2000), has been proposed and successfully applied to the study of stellar haloes around galaxies by Zibetti, White, & Brinkmann (2004). By stacking several hundreds of images, mean surface brightnesses of the order of  $\mu_r=29\text{--}30$  mag arcsec $^{-2}$  can be reliably measured. In fact, not only is the S/N enhanced, but also inhomogeneities in the background signal and in flat fielding are averaged out. A further advantage comes from the fact that the SDSS images are obtained in drift-scan mode (Gunn et al. 1998). As opposed to the ‘staring’ mode, in which the intensity of each pixel in the image is measured by the corresponding pixel on the CCD array, in drift-scan mode the signal is integrated over an entire column of the CCD while the target drifts in the field of view. Therefore, sensitivity variations can occur only in one dimension (i.e. perpendicular to the drift direction) instead of two; this strongly reduces the flat-field inhomogeneities in the frames.

The stacking analysis is statistical in its nature, providing mean results for large samples of galaxy clusters, which can be compared in principle to similar properties derived from cosmological simulations. An appropriate choice of subsamples makes it possible to study the influence of different parameters on the properties of the ICL. Although high statistical significance is the main advantage of the stacking method, individual features (tidal streams and arclets, for instance) and real cluster-to-cluster variations are lost in the averaging. The stacking method is therefore complementary to imaging of individual clusters, from which detailed information about small scale structures and stochastic phenomena can be derived.

In this paper we present an analysis of the stacking of 683 clusters imaged in the  $g$ ,  $r$ , and  $i$  bands in the SDSS. They were selected over  $\sim 1500$  deg $^2$  between  $z = 0.2$  and  $0.3$ , using the maxBCG method (Annis et al., in preparation). Details on the sample selection and on sample properties are given in Sec. 3.2. The image processing and the stacking technique are described in Sec. 3.3. In Sec. 3.4 we describe how the relevant photometric quantities are derived. We present the results of our analysis in Sec. 3.5. Possible sources of systematic uncertainties on the derived quantities are discussed in Sec. 3.6. Our results are compared to other extant observations and model predictions in Sec. 3.7, and some possible implications for theories of the formation of the ICL during cluster evolution are presented. Conclusions and future perspectives are outlined in Sec. 3.8.

Throughout the paper we adopt the ‘‘concordance’’ cosmology,  $H_0 = 70$  km

$\text{sec}^{-1} \text{Mpc}^{-1}$ ,  $\Omega_0=1$ ,  $\Omega_\Lambda=0.7$ .

## 3.2 The sample

The imaging data utilised in this work are derived from the SDSS (York et al. 2000; Stoughton et al. 2002; Abazajian et al. 2003, 2004). The SDSS is imaging about a quarter of the sky in the  $u$ ,  $g$ ,  $r$ ,  $i$ , and  $z$  bands, with a  $\sim 54$  sec exposure in drift scan mode at the dedicated 2.5 m Apache Point Observatory telescope (Fukugita et al. 1996; Gunn et al. 1998; Hogg et al. 2001; Smith et al. 2002; Pier et al. 2003), reaching  $\sim 25$  mag arcsec $^{-2}$  at  $S/N \sim 1$  for a single pixel in the  $r$ -band. The SDSS spectroscopic galaxy samples (Blanton et al. 2003a) consist of all galaxies brighter than  $r = 17.77$  mag (Strauss et al. 2002) and of a sample of Luminous Red Galaxies (Eisenstein et al. 2001) extending at  $r < 19.2$  mag.

To reach surface brightnesses as low as 29–30 mag arcsec $^{-2}$  stacking of several hundreds of images is required. We have focused our sample selection on clusters in the redshift range 0.2–0.3 in order to satisfy the requirement of homogenous imaging coverage within each cluster. Along the scan direction the main limitation is given by the sky background fluctuations, whereas in the perpendicular direction the limit is given by the width of the SDSS camera columns (Gunn et al. 1998), which corresponds to  $\sim 13.5$  arcmin. For practical convenience we use only the SDSS fpC frame ( $13.5 \times 9.8$  arcmin $^2$ ) in which the cluster centre is located and require that a significant fraction of “background” beyond 1 Mpc projected distance from the cluster centre be included. Given that 1 Mpc=5.05 arcmin at  $z = 0.2$ , this turns out to be a good lower redshift limit. On the other hand, we prefer to avoid extending the sample to much higher redshift, both because cosmological dimming acts to reduce the apparent surface brightness by  $(1+z)^4$ , and because resolving individual galaxies in the clusters becomes increasingly difficult. Moreover, K-corrections for band shifting would have to be taken into account in order to interpret a stack of objects in a wide range of  $z$ . Since we do not know *a priori* the spectral energy distribution (SED) of the ICL, this would add considerable uncertainty to results. The 4000Å-break is probably the main feature in the SED of the ICL, so we have chosen  $z = 0.3$  as upper limit; the break is then almost homogeneously bracketed by the  $g - r$  colour over the whole sample.

Cluster identifications over an area of  $\sim 1500$  deg $^2$  in the SDSS DR1 (Abazajian et al. 2003) have been kindly provided by J. Annis, based on the maxBCG method (see Annis et al., in preparation, Bahcall et al. 2003, for details). This

### 3 The optical emission from intracluster stars at $z \sim 0.25$

---

method is based on the fact that (i) the BCGs lie in a narrow region of the  $(g-r)$ - $(r-i)$ - $M_i$  space, and (ii) the early type galaxies in a cluster define a ridge-line in the colour-magnitude diagram. The likelihood of a galaxy being the BCG of a cluster is calculated for a grid of different redshifts taking into account the “distance” of the galaxy from the predicted BCG locus and the number of galaxies  $N_{\text{gal}}$  within  $1 h^{-1}$  Mpc which lie less than  $2 \sigma$  away from the early-type colour-magnitude relation ( $\sigma$  being the average scatter of the relation). The redshift which maximises the likelihood is taken as the fiducial redshift of the cluster; only clusters whose probability is greater than a certain threshold are considered. In addition to the identification of the BCG and the photometric redshift of the cluster, the maxBCG method produces the number of red-sequence galaxies within  $1 h^{-1}$  Mpc,  $N_{\text{gal}}$ , their total luminosity,  $L_{\text{RG}}$ , and the number of red-sequence galaxies within  $0.33 h^{-1}$  Mpc,  $N_{\text{gal},3}$ . Based on the analysis conducted by Hansen et al. (2002) and Hansen et al. (in preparation) on the galaxy count overdensity around 12830 BCGs in the redshift interval  $0.07 \leq z < 0.3$ , an estimate of  $R_{200}^1$  is given using the empirical relation found by these authors between  $N_{\text{gal}}$  and  $R_{200}$ .

From the maxBCG catalogue we have selected all the clusters with:  $0.15 \leq z_{\text{maxBCG}} \leq 0.35$ ;  $N_{\text{gal}} \geq 15$ ;  $N_{\text{gal},3} \geq 5$ . This preliminary selection uses a broader redshift range to include those BCGs whose spectroscopic  $z$  is within the 0.2–0.3 interval, although the maxBCG  $z$  is not (see below). The constraints on the number of galaxies within 1 and  $0.33 h^{-1}$  Mpc should ensure that we select clusters with richness similar to those listed in the Abell catalogue (Abell 1958; Abell, Corwin, & Olowin 1989). The positions of the BCG that passed this first selection has been matched to objects in the SDSS spectroscopic database. Whenever available, the spectroscopic redshift of the BCG has been assigned as the fiducial redshift of the entire cluster (see Annis et al., in preparation, for details on the precision achieved by the maxBCG in the redshift determinations). All selected clusters with  $0.195 < z < 0.3$  have been inspected using RGB composite images ( $g-r-i$ ) in order: *i*) to exclude the images affected by evident defects, such as strong background gradients, and scattered light from very bright stars; *ii*) to check that the selected BCG is actually the brightest member (the maxBCG algorithm sometimes selects the second or third ranked member), and, if not, to assign the position of the new BCG; *iii*) to exclude candidate clusters where no clear enhancement of the galaxy number density is visible toward the centre. This final step prunes the sample of roughly 10 per cent of poor cluster candidates, with a very low

---

<sup>1</sup> $R_{200}$  is the radius that encloses an average mass density which is 200 times the density of the background.

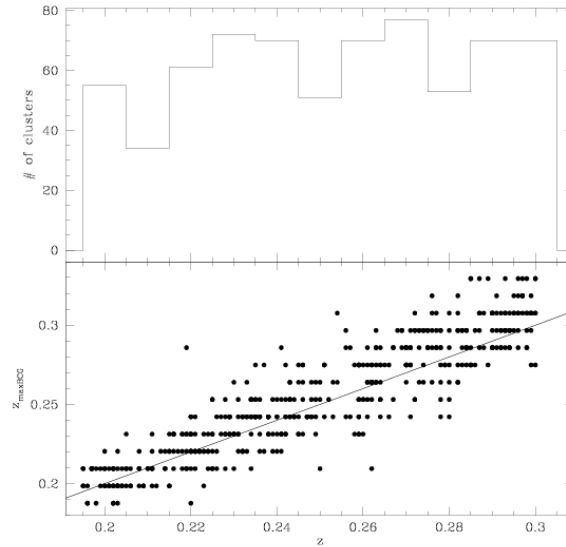


**Figure 3.1:** The redshift distribution of the galaxy clusters in our main sample (upper panel). In the bottom panel we show the comparison between the spectroscopic (abscissa) and the photometric maxBCG redshifts (ordinates) for the 464 clusters whose BCG has been spectroscopically observed. The  $z = z_{\text{maxBCG}}$  relation is shown by the straight line.

spatial concentration. These are likely just chance superposition of galaxies, rather than physically bound associations. A total of 683 clusters satisfy all these requirements and constitute our main sample.

### 3.2.1 Sample properties

The distribution in redshift of the main sample is almost uniform between 0.2 and 0.3, as shown in the top panel of Fig. 3.1, and we will therefore use 0.25 as the reference redshift of the sample. In the bottom panel of the same figure we plot the spectroscopic (in abscissa) and the photometric maxBCG redshifts (in ordinates) for the 464 clusters whose BCG has been spectroscopically observed. The typical error of the photometric redshift is 0.015. Note that 49 of these clusters would have been excluded based on the photometric redshift, as located beyond  $z = 0.3$ . Considering that among the 219 clusters, for which no spectroscopic redshift is available, only 69 are at  $z_{\text{est}} > 0.28$ , we conclude that fewer than 15-20 clusters of  $z$  significantly larger than 0.3 contaminate our sample.

### 3 The optical emission from intracluster stars at $z \sim 0.25$

---

The distributions of the other fundamental properties derived from the maxBCG analysis and from the photometry of the BCG are reported in Fig. 3.2. In the first three panels (a, b and c), we show histograms of the number of clusters as a function of the luminosity of the red sequence galaxies, of the number of red galaxies, and of the luminosity of the BCG, respectively. The total luminosity and the number of red galaxies are in principle equivalent proxies for the richness of clusters. However, due to the small number of galaxies in the poorest clusters, the luminosity provides a smoother distribution at the poor end. The three distributions are peaked around the average values, with roughly 50 per cent of the sample sharing very similar properties, namely 16–24 red galaxies or  $L_{\text{RG}} = 15\text{--}25 L_{i,-21.0}$ ,<sup>2</sup> and  $m_{r,0.25}(\text{BCG})$  between 17.2 and 18. The well known correlation between richness and luminosity of the BCG is present in our sample as visible in panel d). Nevertheless, the scatter is conspicuous and different BCG luminosities can correspond to very different richness.

Unfortunately the redshift range of our sample makes its overlap with the Abell cluster catalogue quite small: although 130 clusters catalogued by Abell, Corwin, & Olowin (1989) as distance class 6 are included in the area of sky covered by our sample, only 43 match the position of our clusters within 6 arcmin, and have Abell richness ranging from 0 to 4. Most (95 per cent) of the remaining 87 are excluded because of their low redshift, and just 5 per cent are rejected because of defects in the imaging data.

In Section 3.5.5 we will analyse the properties of the ICL in different cluster subsamples. In particular we will refer to “poor” (“P”) and “rich” (“R”) clusters as those having less than 17 red galaxies and more than 22,<sup>3</sup> respectively; “luminous-BCG” (“L”) and “faint-BCG” (“F”) clusters are classified according to the luminosity of the BCG, brighter than  $m_{r,0.25} = 17.35$  or fainter than 17.75. These boundaries are marked with arrows in panels b and c of Fig. 3.2. In order to illustrate the differences, we show in Fig. 3.3 the  $r$ -band images of four typical clusters in the “rich”, “poor”, “luminous-BCG” and “faint-BCG” subsamples (panels a, b, c and d respectively). It is particularly instructive to see how richness and BCG luminosity do not always correspond, despite their general correlation. Although the BCG of the “rich” cluster is more luminous than the BCG of the “faint-BCG” one, it is not significantly brighter than the BCG of the “poor” cluster. Vice versa, although the “luminous-BCG” cluster is richer than the “poor” one, it is not significantly richer than the

---

<sup>2</sup> $L_{i,-21.0}$  is the luminosity corresponding to  $-21.0$  absolute  $i$ -band mag in the rest-frame.

<sup>3</sup>Note that of the 178 clusters that make up the ‘rich’ subsample, 31 are catalogued by Abell, Corwin, & Olowin (1989), corresponding to 17.4 per cent.

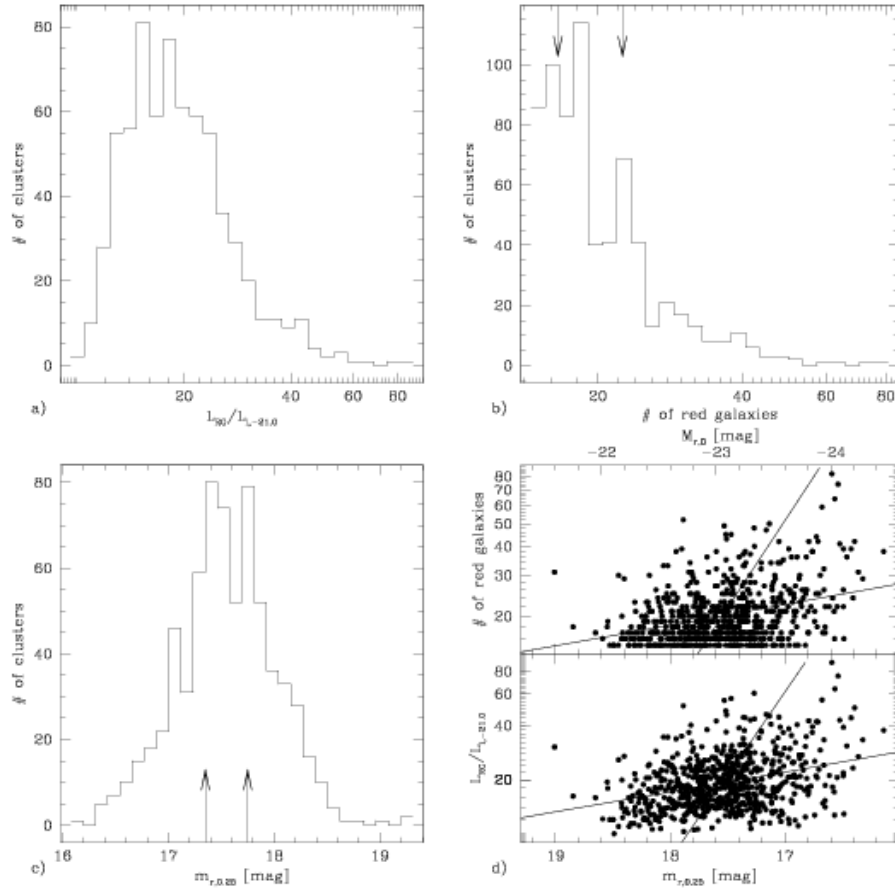


**Figure 3.2:** Properties of the main sample of galaxy clusters. a) distribution of the total luminosity of the red sequence galaxies. The luminosity is expressed in units of the luminosity corresponding to  $M_i = -21.0$ . b) distribution of the number of red sequence galaxies. Arrows indicate the upper and lower limits for the “poor” and “rich” subsamples respectively. c) Distribution of BCG luminosities, in units of  $r$ -mag in the observer frame for  $z = 0.25$ . Arrows indicate the upper and lower limits for the “luminous-BCG” and “faint-BCG” subsamples respectively. d) Correlations of the BCG luminosity with the luminosity of the red sequence galaxies (bottom) and with the number of red sequence galaxies (top). Solid lines show the direct (y vs. x) and inverse (x vs. y) regression lines from the least squares linear fitting to the points. The scale on the upper axis reports the rest-frame  $r$ -band absolute magnitudes, using the K-corrections calculated for a 13 Gyr old, solar metallicity SSP with the code of Bruzual & Charlot (2003).

“faint-BCG” cluster.

### 3.3 The image processing and stacking

Our stacking technique consists in averaging the images of a large number of galaxy clusters after masking all the unwanted sources. Since we are interested both in the diffuse emission from intracluster stars and in the overall cluster luminosity, including galaxies, two different masks must be utilised. In the first case we mask all the detectable sources excluding the BCG (masks “A”), while the foreground stellar sources only are masked when studying the total emission (masks “B”). In this second case, contamination from galaxies not belonging to the clusters is significant. However, thanks to the large number of fields that are stacked, their light is almost uniformly distributed in the stacked frame and their contribution to the surface brightness can be reliably estimated sufficiently far from the centre of the cluster. Detection limits and surface brightness thresholds in building the “A” masks are expected to have an important influence on the estimated amount of diffuse light: we will thoroughly discuss this issue in Sections 3.4.1 and 3.6.2.

A big advantage of the stacking approach with respect to traditional imaging of individual clusters resides in the possibility of applying very conservative masking to the foreground (stellar) sources, without any significant loss in the measured signal. Combined with the uniform distribution of contaminating foregrounds in the resulting stacked image, this masking makes a careful modelling of the point spread function (PSF) unnecessary in order to subtract foreground stars.

The SDSS imaging data are available as bias subtracted, flat-field corrected frames; adopting the standard SDSS terminology, we will refer to these as “corrected frames” in the following. We use only the three most sensitive SDSS pass-bands,  $g$ ,  $r$  and  $i$ . Before images can be actually stacked, background subtraction, geometric transformation and intensity rescaling must be applied. For each cluster we estimate the sky background in an annulus with inner radius corresponding to 1 Mpc, 100 kpc thick, centred on the BCG. Sources lying in that area were masked using the segmentation image obtained by running SExtractor (Bertin & Arnouts 1996)<sup>4</sup> with a Gaussian smoothing kernel (FWHM = 4.0 pixels), and a detection threshold of 0.3 times the local rms and 5 pixels as minimum area.

We extract  $1600 \times 1600$  pixel<sup>2</sup> ( $\approx 634 \times 634$  arcsec<sup>2</sup>) frames centred on the BCG, using the standard IRAF task `geotran`. Pixels are resampled using

---

<sup>4</sup>We use SExtractor version 2.3 throughout the present work.

### 3.3 The image processing and stacking

---

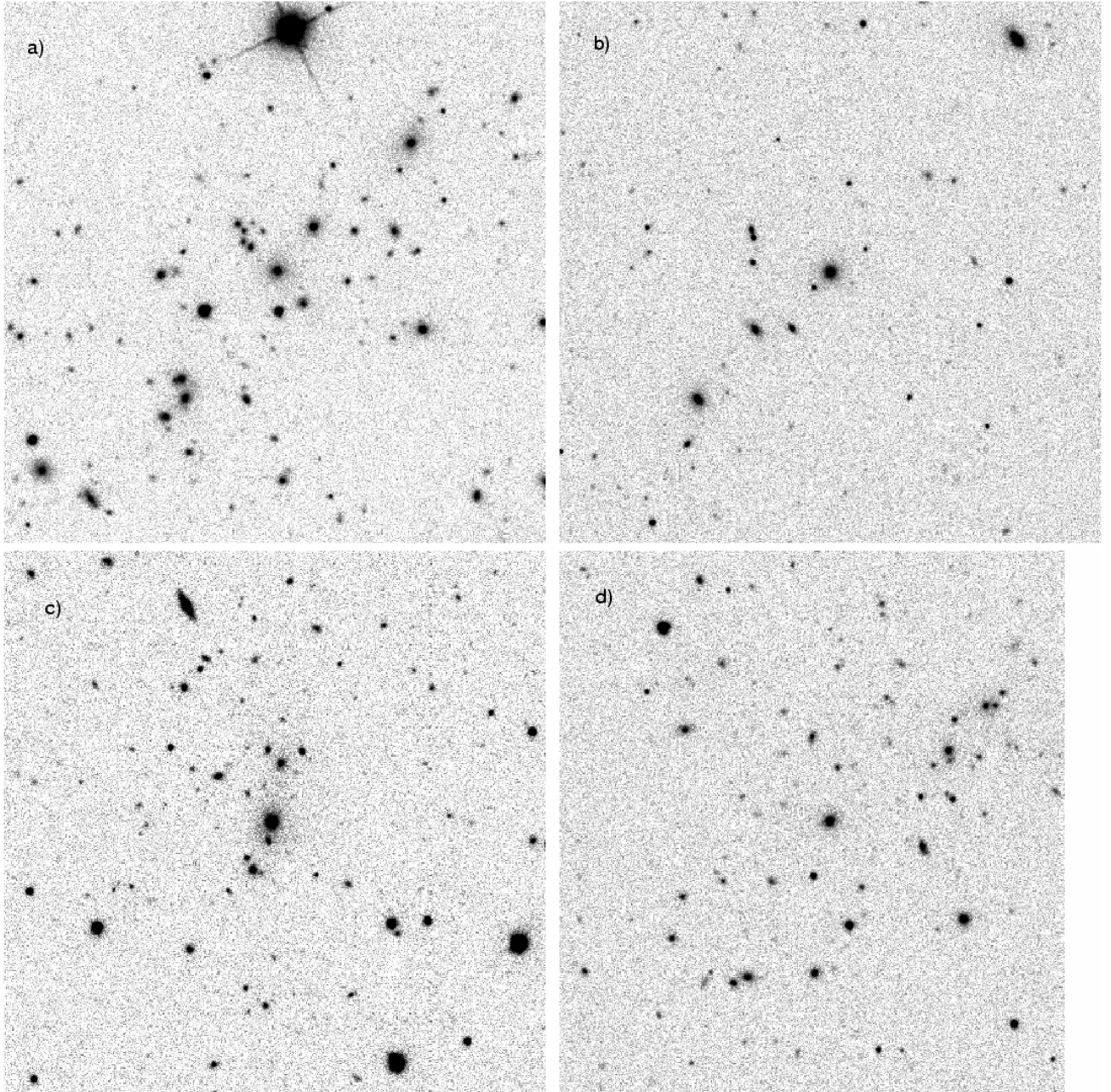


**Figure 3.3:**  $r$ -band images of four typical clusters in the “rich”, “poor”, “luminous-BCG” and “faint-BCG” subsamples (panels a, b, c and d respectively). Each frame is  $500 \times 500$  pixel<sup>2</sup>, corresponding to 3.3 arcmin side,  $\sim 0.8h_{70}^{-1}$  projected Mpc.

### 3 The optical emission from intracluster stars at $z \sim 0.25$

---

linear interpolation and all images are rescaled to the same metric length at the redshift of the cluster. Considering the redshift distribution of the sample, we rescale the images such that  $1 \text{ Mpc} = 629.3 \text{ pixels}$ , thus minimising the average rescaling. In addition we either apply a random rotation before stacking, or we align the images based on the BCG orientation. The first method is more appropriate to study the radial surface brightness profiles, since it ensures the perfect central symmetry of the stacked images. Aligning the images to the BCG is most suitable in order to study the correlation between the 2-dimensional shapes of different luminous components, as will be shown in Sec. 3.5.3.

Pixel counts are then rescaled in order to remove the effects of the variation of Galactic extinction and cosmological surface brightness dimming  $(1+z)^4$  between different clusters, and to homogenise the photometric calibration (Fukugita et al. 1996; Hogg et al. 2001; Smith et al. 2002). This was done according to the following equation:

$$c' = c \times \frac{f_{20,\text{ref}}}{f_{20}} \times 10^{0.4 \times A_\lambda} \times \left( \frac{1+z}{1+z_{\text{ref}}} \right)^4 \quad (3.1)$$

where  $c'$  and  $c$  are the counts in a pixel after and before intensity rescaling, respectively;  $f_{20,\text{ref}}$  and  $f_{20}$  are the counts corresponding to 20 mag in the arbitrary reference calibration system and in the frame calibration system respectively;  $A_\lambda$  is the Galactic extinction as reported in the SDSS database, according to Schlegel, Finkbeiner, & Davis (1998);  $z$  and  $z_{\text{ref}}$  are the redshift of the cluster and the reference redshift, that has been chosen to be close to the median redshift of the sample, that is 0.25. This calculation ignores K-corrections as they are unknown for the ICL and given the small redshift range probably have negligible effects on our results. In the following we will always use the subscript “0.25” to refer to magnitudes and surface brightness in the photometric system defined by Equation 3.1.

Masks “A” and “B” are built for each cluster from an analysis of the original corrected frames, and then geometrically transformed to match the corresponding images. First we build the “B” mask for the saturated sources and the stars in the field. Relying on the SDSS photometric database, we select all objects which are flagged as saturated and lie within 10 arcmin of the BCG. These are masked out to an extent of three times the maximum isophotal radius in the three bands, in order to avoid including scattered light or their bright extended haloes in the stack. All stars brighter than 20 mag in  $r$ -band, with isophotal radius measured in at least two bands, are identified and masked out to their maximum isophotal radius in the three bands. The

### 3.4 The photometric analysis

---

magnitude limit is chosen such that less than 1 per cent of objects classified as stars by the photometric pipeline are likely to be misclassified galaxies (see Ivezić et al. 2002). This allows us to minimise the foreground signal, while losing a negligible fraction of light from cluster galaxies. However, a small fraction (less than 10 per cent) of bright non-saturated stars are left unmasked because they do not have good isophotal measurements. Since these stars are randomly located in the frames, no systematic effects on our measurements are expected, although this failure increases the noise in the foreground signal.

To obtain the “A” mask we run SExtractor on the frames in the three bands, using a Gaussian smoothing kernel (FWHM = 4.0 pixels), a minimum detection area of 10 pixels and detection thresholds corresponding to  $\mu_{r,0.25} = 24.5$ ,  $\mu_{g,0.25} = 25.0$  and  $\mu_{i,0.25} = 24.0$  mag arcsec<sup>-2</sup>. We blank the segment corresponding to the BCG in the segmentation images and OR-combine them with the “B” mask previously generated to get the final “A” mask. Note that both the “A” and the “B” masks are the same for all the three bands, thus allowing a consistent measurement of the colours.

The stacking of the images is performed using the standard IRAF task `imcombine`. The images in each (sub)sample are combined with a simple average of the pixel counts, excluding the masked pixels. We do not apply any kind of statistical rejection to the pixel count distributions, since we cannot assume that the light follows the same distribution in all clusters on a few pixel scale. This is obviously not the case when considering the total light which is dominated by the galaxies, but even for the diffuse component significant substructure can be present as well (see e.g. Gregg & West 1998; Trentham & Mobasher 1998; Calcáneo-Roldán et al. 2000).

### 3.4 The photometric analysis

In Fig. 3.4 we present the central  $\sim 600$  kpc of the stacked images in the total sample, for the diffuse component plus BCG (“A” masks, left panel) and for the total emission (“B” masks, right panel). In order to increase the  $S/N$ , the  $r$  and  $i$  bands have been combined in these plates using a weighted average of the intensities, where the weights are given by the inverse square of the rms of the intensity in each stacked pixel. The combined intensities are translated into AB mag for a combined  $r + i$  pass-band, whose effective response function is given by the sum of the two filter responses. Scales are marked in kpc. In panel a) we superpose the isophotal contours corresponding to 26, 27, 28, 29 and 30 mag arcsec<sup>-2</sup> in the  $r+i_{0.25}$  band, obtained smoothing the original image with kernels of increasing size, as described in the caption.

### 3 The optical emission from intracluster stars at $z \sim 0.25$

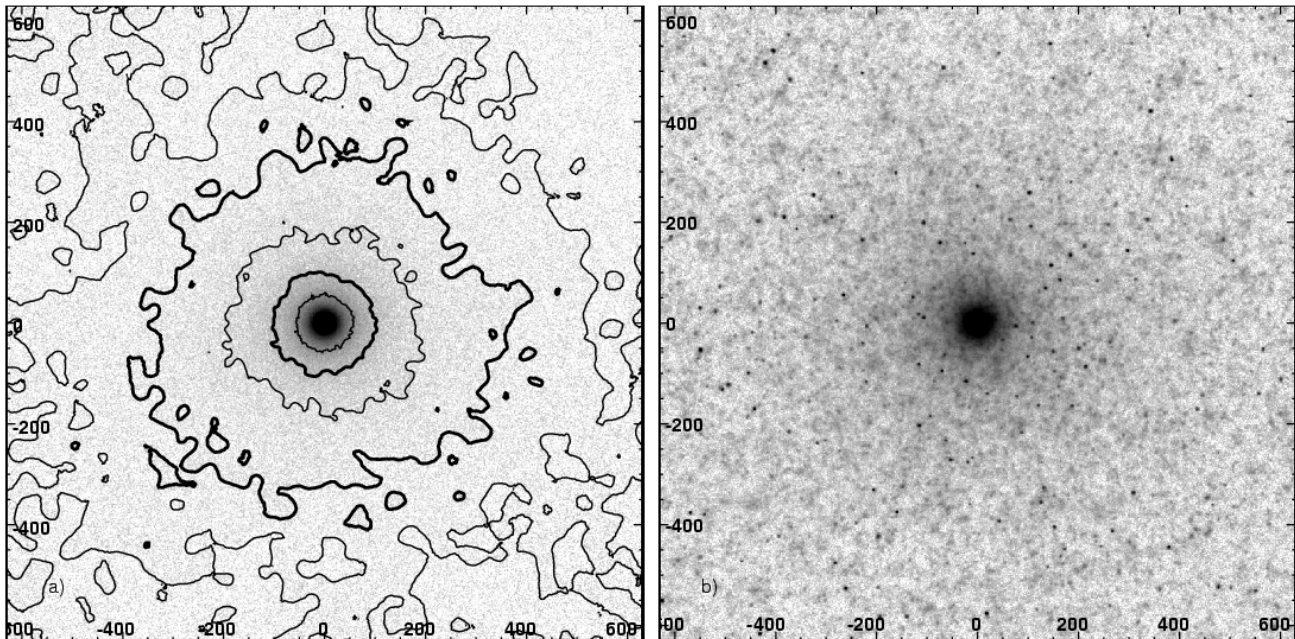


**Figure 3.4:** The  $r + i$  composite images resulting from the stacking of the main sample: the diffuse component plus BCG is in panel a), the total light in panel b). The same logarithmic grey scale is adopted in both images. Side-scale tickmarks display the distance in kpc from the centre. Isophotal contours corresponding to  $\mu_{(r+i),0.25}$  of 26, 27, 28, 29 and 30 mag arcsec<sup>-2</sup> for the diffuse component are overplotted on panel a). Smoothing kernels of 3, 7, 11, 17, and 21 pixels respectively are used. Corresponding SB values in  $r$ -band are  $\sim 0.3$  mag brighter. Note the point-like sources in panel b), that are the stars left unmasked due to the failure in the measurements of their isophotal radii, as mentioned in Section 3.3.

Corresponding SB values in  $r$ -band are  $\sim 0.3$  mag brighter.

In both panels the central region ( $R \lesssim 100$  kpc) is dominated by the BCG, which has not been covered by either the “A” or “B” masks. Given the circular symmetry of the stacked images and the need to integrate over large areas to increase the  $S/N$ , we perform the photometric analysis in circular apertures. The stacked image is first divided into a number of circular annuli, centred on the BCG and logarithmically spaced. Within each annulus, the average surface brightness is computed simply by summing the intensity in the pixels and dividing by the total number of pixels. The logarithmic spacing ensures that a larger area is summed at large radii, where the signal is lower. In order to evaluate the statistical uncertainty on the computed SB, we further divide each annulus into a number of sectors with aperture angle  $\theta \simeq \frac{\Delta R}{R}$ , where  $\Delta R$

is the thickness of the annulus and  $R$  its average distance from the centre. The rms of the SB among the sectors is thus representative of the SB fluctuations on the typical spatial scale covered by the annulus; the statistical error on the average SB is then just given by the rms divided by  $\sqrt{N-1}$ ,  $N$  being the number of sectors in the annulus.

Background estimation is a critical issue when attempting to measure very low surface brightnesses, which are just a few sigma above the noise. In particular, when integrated fluxes over large areas are estimated, the uncertainty on the background level dominates the measurement error.

Due to the limited spatial coverage provided by the individual SDSS frames, at  $R \gtrsim 1$  Mpc and beyond, the fraction of stacked images which contribute to the intensity of each pixel drops below 50 per cent. Given the average  $R_{200}$  of 1.1 Mpc for the clusters in the main sample,<sup>5</sup> we cannot directly estimate the background level around the stacked cluster images. Since the mean galaxy profile of clusters is known to follow the analytical profile proposed by Navarro, Frenk, & White (1995) (NFW, see, for example, Carlberg et al. 1997), we estimate the background SB level in the stacked images by fitting a projected NFW profile (see Bartelmann 1996) plus a constant to the SB profiles extracted before. The fitting is performed between 100 and 900 kpc, the innermost 100 kpc being excluded because of the predominance of the de Vaucouleurs profile (de Vaucouleurs 1948) of the BCG in these central regions. The best fitting value of the constant is used as the residual background level, which may be positive or negative, since a sky background has already been subtracted from each individual cluster image based on the mean sky surface brightness 1 Mpc away from the BCG. The corresponding uncertainty is given by the square root of its variance as determined from a set of Monte Carlo realizations of the measured profile, where the intensity in each point is randomly varied according to the associated error. In Section 3.7 we will discuss in further detail the validity of this method.

#### 3.4.1 Definition of the ICL and corrections for mask incompleteness

A measurement of the intracluster light, conventionally defined as the luminous emission from stars which are unbound to any individual galaxy, would require a fully dynamical characterisation of such stars. This is completely beyond our observational capabilities. Based on purely photometric properties, the most sensible and robust definition of the ICL is the emission coming from outside the optical boundaries of individual galaxies. Given the properties of

<sup>5</sup>This is consistent with a mean mass of  $7-8 \times 10^{13} M_{\odot}$ .

### 3 The optical emission from intracluster stars at $z \sim 0.25$

---

our dataset, we define the optical boundary as the  $\mu_{r,0.25} = 25.0$  mag arcsec<sup>-2</sup> isophotal contour. This does not encompass the low surface brightness emission from the outermost parts of galaxies, so a fraction of what we define as ICL will actually come from stars bound to galaxies, as we will argue more quantitatively in Sec. 3.5.4.

In addition to this contribution which is inherent to our definition of the ICL, contamination arises also from incomplete masking (i.e. from masks failing to cover the entire optical extent of a galaxy) and from undetected galaxies. We have tested the efficiency of our masking algorithm on a mock dataset of  $\sim 650$  simulated clusters. In order to reproduce the observational properties of the real sample, we use the same redshift, Galactic extinction, background noise properties, point spread function (PSF) and photometric calibration parameters as in the real cluster sample.

For each simulated cluster, we generate 1,000 random galaxies whose photometric properties are assigned as follows. First we draw their absolute  $r$ -band luminosity from a Schechter luminosity function (LF), using the fitting parameters of Mobasher et al. (2003) ( $\alpha = -1.18$ ,  $M_R^* = -21.79 + 5 \log h_{65}$ )<sup>6</sup>, who studied the LF of the Coma cluster down to  $M_R = -16 + 5 \log h_{65}$ . Using the data in Blanton et al. (2003b), we have computed the two-dimensional conditional probability function  $P(n, \mu_e | L)$  of the Sérsic index  $n$  and  $\mu_e$  for a given luminosity  $L$ . According to this, we assign random  $n$  and  $\mu_e$  to each galaxy. A projected axial ratio is randomly drawn from a Gaussian distribution centred at 0.7 and with  $\sigma = 0.25$  (we assume that clusters are dominated by early-type galaxies and use the results in Lambas, Maddox, & Loveday 1992), the orientation is random.

The model SB distribution in the  $r_{0.25}$ -band is then computed *out to the optical radius* (as defined above). Size and intensity are rescaled according to the redshift<sup>7</sup>, Galactic extinction and photometric calibration of the corresponding observed cluster. The model distribution is sampled on the pixel array. The resulting image array is then convolved with the PSF and the sky background is added. Finally we add Poisson noise, using the actual electron-to-ADU conversion factor of each frame. We use the average colours of the total light in the stacked images to derive from the  $r_{0.25}$ -band model image the corresponding mock frames in the  $g$  and  $i$  bands.

The mock images are processed with the same codes and algorithms used for

---

<sup>6</sup>This corresponds to  $M_r^* = -21.37 + 5 \log h_{70}$  using the photometric conversion provided by the Bruzual & Charlot (2003) code for a 13 Gyr old, solar metallicity SSP.

<sup>7</sup>We adopt a uniform K-correction within each cluster, namely the one for a spectral energy distribution of a simple stellar population formed 10 Gyrs ago with solar metal enrichment (Bruzual & Charlot 2003).

the real ones, and stacked. We find that roughly 15 per cent of the light in the  $r$ -band within the optical radius of the simulated galaxies fails to be blocked by our masking algorithm, because of partial or complete non-detections. Very similar amounts are missed in  $g$  and  $i$ . These results clearly are expected to depend on the shape of the luminosity function of the cluster galaxies, and particularly on the slope at the faint end. In fact a steeper faint-end and/or a fainter  $M^*$  can produce significantly higher contaminating fractions, and *vice versa*. We will discuss the systematic uncertainty deriving from the choice of the LF in further detail in Sec. 3.6.2. Throughout the rest of the paper we will adopt the corrections based on the Mobasher et al. (2003) LF as our fiducial corrections.

Assuming that the fraction  $f$  of unblocked galaxy luminosity is roughly independent of clustercentric distance, we can compute the corrected surface brightness of the ICL:

$$\Sigma_{\text{ICL}} = \frac{1}{1-f} \times \Sigma_{\text{diffuse}} - \frac{f}{1-f} \times \Sigma_{\text{total}} \quad (3.2)$$

where  $\Sigma_{\text{diffuse}}$  and  $\Sigma_{\text{total}}$  are the surface brightness as derived from the stacked images masked with the “A” and “B” masks respectively.

## 3.5 Results

### 3.5.1 Surface brightness profiles

We present the results of our photometric analysis for the main sample in Fig. 3.5. In the first three panels (a) to (c) we show surface brightness profiles for various cluster components (lower plots) as well as the local ratio of  $ICL + BCG$  to the total cluster light (upper plots) for the  $g$ -,  $r$ - and  $i$ -band. The radial coordinate is scaled to  $R^{1/4}$ . In the SB profile plots, red triangles with error bars represent the average *total* SB, including all cluster components, whereas black open circles are the SB of the *diffuse* component ( $ICL + BCG$ ). The SB of the  $ICL+BCG$  component after correcting for the contamination due to mask incompleteness is shown by black filled circles with error bars. For the *total* SB error bars represent the maximum range of variation when allowing for  $1-\sigma$  uncertainties in the background level and in the local estimate of the SB. For the  $ICL+BCG$  component the analogous maximum range of variation is computed taking errors on both *total* and *diffuse* light measurements into account, after combining them with the standard error propagation formulae applied to Equation 3.2. The two horizontal lines display the SB corresponding to  $1-\sigma$  background uncertainty, for the *total* light (red dashed line), and for the *diffuse* light (black solid line).

### 3 The optical emission from intracluster stars at $z \sim 0.25$

---

The profiles can be reliably traced out to  $\sim 700$  kpc at the level of  $\mu_{r,0.25} \sim 32$  for the ICL ( $\mu_{r,0.25} \sim 31$  for the uncorrected *diffuse* component) and  $\mu_{r,0.25} \sim 29$  mag arcsec $^{-2}$  for total light (5- $\sigma$  detections are obtained at 500 kpc in all bands).

As apparent from the straight-line behaviour in all three bands, in the inner 40–50 kpc the SB profile of the *ICL+BCG* component closely follows a de Vaucouleurs’ law. We fit this law to the inner points of the profiles using an iterative procedure based on standard least squares. We start fitting between 10 and 20 kpc to ensure that we exclude the innermost region, where the seeing (FWHM  $\sim 5$  kpc at the average redshift of the clusters) is likely to significantly affect the measured profile. Outer points are added iteratively until the error on the slope is increased by more than 10 per cent with respect to the previous step. The last two points are then discarded and the fitting parameters are recomputed.

The best fitting de Vaucouleurs’ law to the inner *ICL+BCG* profile is plotted as a dotted line in the lower section of panels a) to c) of Fig. 3.5. The effective radius  $R_e$  is marked with a vertical dashed line and fitting parameters are reported nearby. Typical errors are  $\sim 10$  per cent on  $R_e$  and  $\sim 0.1$  mag arcsec $^{-2}$  on  $\mu_e$ . We note that, while the effective radii are consistent in  $r$  and  $i$ , in the  $g$ -band  $R_e$  is significantly larger by some 5 per cent. This is consistent with a significant colour gradient in the expected sense within the BCG itself.

Beyond 50 kpc the profiles clearly flatten, both in the *ICL* component and in the *total* light. Still, there is evidence for the *ICL* component being more centrally concentrated. The  $R^{1/4}$  slope of the *ICL* component stays roughly constant between 150 and 500–600 kpc, with an equivalent  $R_e$  of 250–300 kpc in all three bands. The *total – diffuse* light is also quite well fit by an  $R^{1/4}$  law, but here the equivalent  $R_e$  is  $\sim 2$  Mpc in all three bands.

The higher concentration of the *ICL* component with respect to the *total* light is confirmed by the upper sections of the plots in Fig. 3.5, where we plot the local ratio of the *ICL+BCG* to the *total* light using black filled circles with error bars. Error bars are computed by combining the errors on the fluxes derived as described above. Empty circles represent the fraction of uncorrected *diffuse* light, that is the upper limit to the ICL fraction when one allows for different choices of the LF.

Excluding the central  $\sim 50$  kpc, where the BCG dominates, a smooth monotonic decrease of the *ICL* fraction is observed all the way out to the limit of significant detections, from  $\sim 50$  per cent at 50 kpc down to  $\lesssim 5$  per cent at 600–700 kpc for our preferred faint galaxy correction. By comparing the two fractions, we see that the *ICL* is the main component of the *diffuse* light out to  $\sim 300$  kpc. Outside this radius we must expect that the *diffuse* emission reflects more and more the properties of faint cluster galaxies rather than those

of the ICL.

### 3.5.2 Colours of the ICL

In panel 3.5(d) we show the  $g - r$  and  $r - i$  colour profiles for the ICL+BCG (black thick solid lines) and for the total light (red thin solid lines). Dashed lines show the  $1-\sigma$  confidence interval derived from the errors on the fluxes in the different bands. Only data-points for which the confidence interval is smaller than 0.5 mag are connected, in order to avoid confusion arising from noisy measurements. We observe a striking consistency between the colours of the *total* emission and those of the *ICL+BCG* in both  $g - r$  and  $r - i$  out to 300 kpc, where the light from bound stars in galaxies dominates the *total* emission. There is marginal evidence for slightly redder  $r - i$  (+0.03 mag) in the ICL at  $R > 100$  kpc, but its significance is low, less than  $1-\sigma$ .

In agreement with the above determinations of  $R_e$ , within 80–100 kpc we find a clear gradient in  $g - r$ , from 1.4–1.5 in the centre to  $\sim 1.20$  at 80 kpc, whereas the  $r - i$  profile is consistent with being flat over this radius range, within the errors, with an average value  $\sim 0.60$ . Outside 80 kpc the  $g - r$  profile flattens too, both for *ICL+BCG* and for the *total* light.

### 3.5.3 Isophotal ellipticity

We now investigate possible relationships between the shape of the BCG and those of the ICL and of the cluster galaxy distributions. We study the isophotal shapes of the ICL and of the galaxy light for two subsamples of clusters in which the BCGs exhibit a clear elongation. The stacking in this case has been performed after aligning the images along the major axis of the BCG. The selection is from the main sample clusters after requiring  $m_{r,0.25}(\text{BCG}) < 17.90$  to ensure a more reliable estimate of the parameters of the best fitting 2-dimensional de Vaucouleurs model, as provided by the SDSS `photo` pipeline (Lupton et al. 2001). We choose an axial ratio limit of  $b/a_{\text{BCG}} < 0.85$ , for the first subsample, and a more restrictive limit of  $b/a_{\text{BCG}} < 0.70$ , for the second one. The images are aligned according to the position angle provided by `photo`. A few clusters, for which the fitting algorithm clearly failed to provide a sensible description of the shape of the BCG, have been rejected after visual inspection. The two final samples contain 355 and 112 clusters.

The analysis of the resulting *diffuse* light image is performed by fitting elliptical isophotes. Such isophote fitting cannot be used for the galaxy light,

### 3 The optical emission from intracluster stars at $z \sim 0.25$

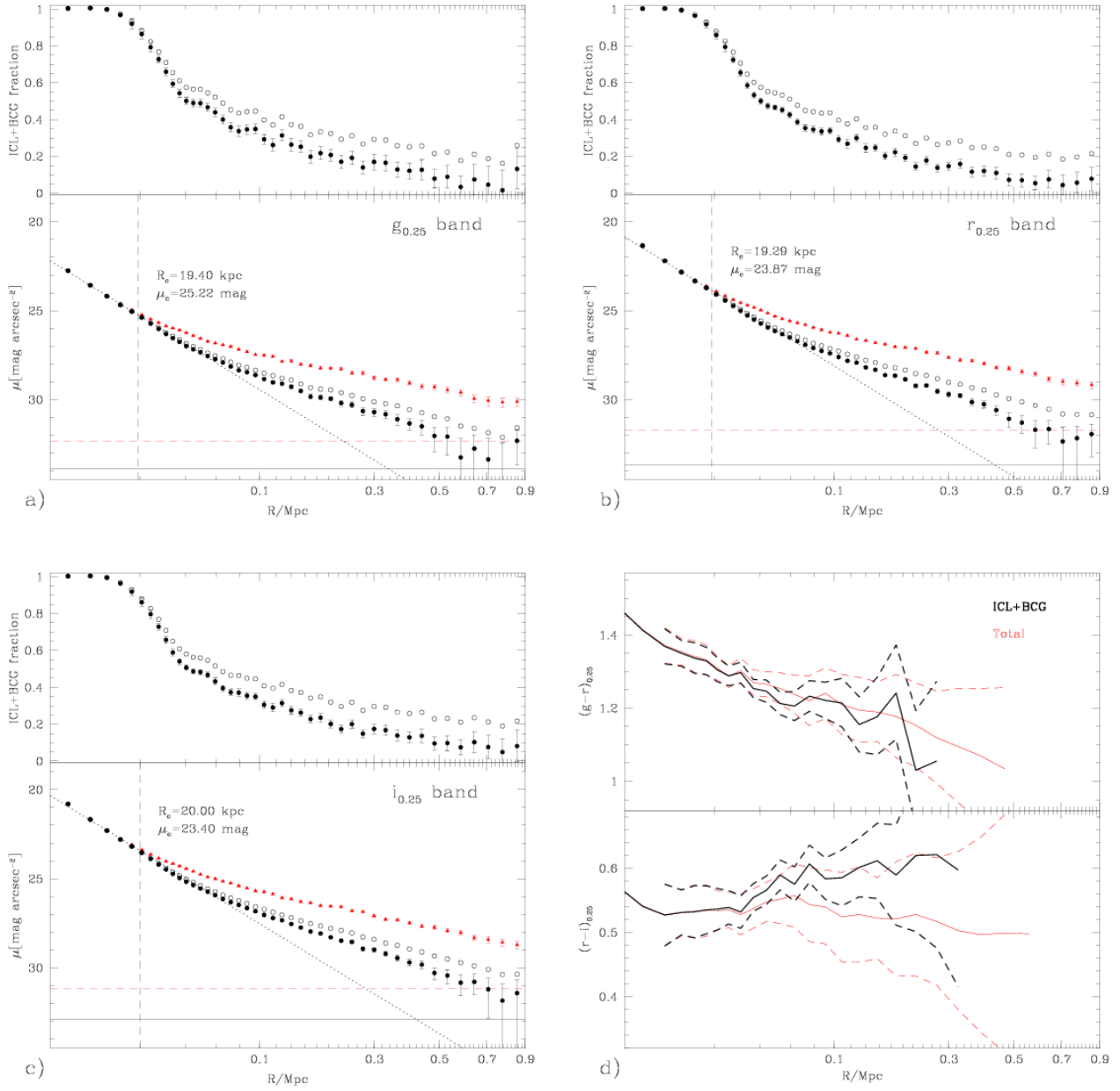


**Figure 3.5:** Surface photometry of the main sample. Panels a) to c) show the surface brightness profiles and the local ratio of  $ICL+BCG$  and uncorrected *diffuse* light to the *total* cluster light in the  $g$ ,  $r$ ,  $i$  bands respectively; in panel d) the  $g-r$  and  $r-i$  colour profiles are plotted. The  $R$  axis is linear in  $R^{1/4}$ . Panels a)-c), lower section: the SB is expressed in  $\text{mag arcsec}^{-2}$  in the  $z = 0.25$  observer frame. Red triangles with error bars represent the total cluster light, open circles with error-bars display the SB of the  $ICL+BCG$ , corrected for masking incompleteness adopting the LF given by Mobasher et al. (2003). Horizontal red dashed and black solid lines display the SB corresponding to the  $1-\sigma$  uncertainties on the background determination for the total light and for the  $ICL+BCG$  respectively. The dotted lines represent the best de Vaucouleurs fits to the inner regions (see text for the details): the effective radii of the best fitting models are indicated with vertical dashed lines and the corresponding parameters are reported nearby. Panels a)-c), upper section: the local ratio of  $ICL+BCG$  (filled dots with error-bars) and uncorrected *diffuse* light (open circles) to *total* cluster light. Panel d):  $g-r$  (upper section) and  $r-i$  (lower section) colour profiles. Red thin lines are used for the *total* light, black thick lines for the  $ICL+BCG$  component, corrected according to the Mobasher et al. (2003) LF. Dashed lines represent the  $1-\sigma$  confidence intervals.

because of the shot noise arising from galaxy discreteness. We therefore characterise the shape of the galaxy distribution by means of moments of the *total – diffuse* light image. We use  $r+i$  band composite images derived from the weighted average of the two single bands (cf. Fig. 3.4), to enhance the  $S/N$ .

In the central 50 kpc of the *diffuse* light image the fitting is done using the standard IRAF task `ellipse`. Outside this radius the  $S/N$  is too small to make the fitting method implemented in `ellipse` applicable. In fact, this method (see Jedrzejewski 1987) consists in minimising the variance of the intensity along 1-pixel wide elliptical paths by varying the geometrical parameters of the ellipse. In our fitting code the elliptical paths are replaced with elliptical annuli, which are several pixel wide, and the intensity variance is computed not on single pixel basis, but using approximately square (side~annulus width), non-overlapping contiguous regions along the annulus. For each given semi-major axis  $a$  the width of the elliptical annulus  $\Delta a$  is fixed as  $a \times 0.2$ . The ellipse is aligned with the BCG. We compute the axial ratio  $b/a$  that minimises the intensity variance using the standard golden section search algorithm, as implemented in Press et al. (1992).

The results of this analysis are shown in Fig. 3.6, where the two panels display the average SB of the isophotes (upper panel) and the axial ratio  $b/a$  of the isophotal ellipses (lower panel). Solid lines are for the sample with  $b/a_{\text{BCG}} < 0.85$ , while dashed lines are for  $b/a_{\text{BCG}} < 0.70$ . Typical errors for  $b/a$  range from 0.05 to  $\gtrsim 0.10$  going from the centre to 700 kpc. The two samples display very similar behaviour, except for a lower  $b/a$  in the sample with flatter BCGs, as expected. We note a progressive flattening of the isophotes from the centre out to  $a \sim 150$  kpc. While the smearing effect of the PSF (FWHM  $\sim 5$  kpc) is certainly biasing the measurements in the central 10–20 kpc, at larger distances this flattening must be considered real. At  $a \gtrsim 500$  kpc, large  $b/a$  uncertainties ( $\gtrsim 0.1$ ) do not allow us to establish whether the apparent increasing trend is real or not. As noted above, however, the *diffuse* light is expected to be dominated by unmasked galaxy light at these distances, and therefore does not provide reliable information on the distribution of the ICL.

The flattening of the cluster galaxy distribution is derived from first order moments of the (*total – diffuse*) light image,  $S_x = \sum_i |x_i| F_i$  and  $S_y = \sum_i |y_i| F_i$ , where the  $x$  and  $y$  coordinates are aligned with and perpendicular to the BCG orientation respectively,  $F_i$  is the fraction of light in pixel  $i$ , and the sums are within an ellipse having 700 kpc semi-major axis and axial ratio  $b/a$ . The  $b/a$  that best fits the flattening of the galaxy light distribution is obtained

### 3 The optical emission from intracluster stars at $z \sim 0.25$

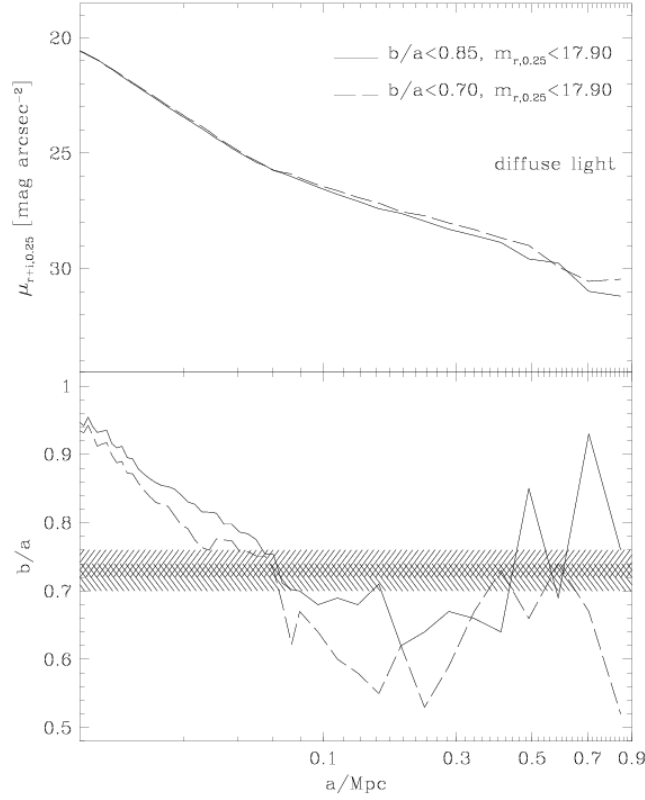


**Figure 3.6:** Elliptical isophote analysis of the diffuse light of two subsamples of clusters, whose images have been aligned along the position angle of the best-fitting de Vaucouleurs model for the BCG. Only clusters with luminous BCG ( $m_{r,0.25}(\text{BCG}) < 17.90$ ) have been stacked. As a function of the semi-major axis  $a$  we show the isophotal SB in the  $r + i$  composite band (upper panel) and the axial ratio  $b/a$  (lower panel). Solid lines are used for the sample with  $b/a_{\text{BCG}} < 0.85$ , dashed lines for  $b/a_{\text{BCG}} < 0.70$ . The shaded regions indicate the mean ellipticity value (plus uncertainty) of the galaxy distribution, with the two different slants representing the two subsamples.

by requiring  $\frac{S_y}{S_x} = b/a$ . For our two subsamples we obtain  $b/a = 0.74 \pm 0.02$  and  $b/a = 0.72 \pm 0.02$ . These results do not change appreciably for variations of the semi-major axis  $a$  in the range 700 to 350 kpc. The galaxy distribution is thus significantly rounder than that of the ICL between 100 and 400 kpc. In fact, by using the *diffuse* light as proxy for the ICL, we are probably underestimating the real effect. Unless the faint galaxy population that contaminates the *diffuse* light has significantly higher degree of alignment with the BCG than

the bright one, the ellipticity we measure in the *diffuse* image should be smaller than in the real ICL.

It is interesting to note that the semi-major axis at which the maximum flattening of the isophote is first reached,  $a \sim 100$  kpc, lies somewhat outside the radius where the outer shallower SB profile takes over from the inner de Vaucouleurs and the galaxy component starts dominating the total light.

### 3.5.4 ICL–galaxy connection

We further investigate the connection between the galaxy distribution and the ICL by studying the photometric properties of the ICL in regions at different projected distances from bright galaxies. First we select all the galaxies more luminous than  $M_r^* + 2.0$  mag in the SDSS database; this corresponds to  $m_{r,0.25} < 21.23$  assuming the Mobasher et al. (2003) LF. All pixels contributing to the *diffuse* light image (i.e. not masked according to type “A” masks) are partitioned into 4 different classes according to their distance  $l$  from the nearest bright galaxy, namely  $l < 15$  kpc,  $15 \leq l < 25$ ,  $25 \leq l < 40$ , and  $l > 40$  kpc. We further distinguish between 4 different ranges in clustercentric distance: from 100 to 200 kpc, from 200 to 400, from 400 to 750 and from 800 to 900 kpc, this last one being roughly representative of the background. Fluxes in each class of  $l$  and clustercentric distance are stacked separately. As the best estimate of the background level we adopt in this case the average surface brightness of pixels in the 800–900 kpc annulus with  $l > 40$  kpc.

The results of this stacking are reported in Table 3.1. The clustercentric distance  $R$  (in kpc) is given in column (1); column (2) reports the projected distance  $l$  to the nearest bright galaxy (in kpc); the average SB of these pixels is given in column (3), while column (4) displays the fraction of ICL in each annulus contributed by pixels in the specific  $l$ –range. For the first three classes of  $l$  we compute the difference between the mean flux actually measured and the flux that would be measured if those pixels had the same SB as the ones at  $l > 40$ . The ratio of this flux excess to the *total* ICL flux in the annulus of clustercentric distance  $R$  is reported in column (5). Finally, the fraction of pixels with projected distance  $l$  to the nearest bright galaxy is given in column (6). The fractions in the last three columns are given in per cent.

In Fig. 3.7 we plot, with solid lines, the SB of the *diffuse* light in the four classes of  $l$  as a function of the clustercentric distance. For the three nearest  $l$  bins, the dashed lines represent the SB of the excess with respect to the SB at  $l > 40$ . We note immediately that the SB around luminous galaxies depends very weakly on the clustercentric distance. This is even more evident if one considers the surface brightness excess plotted with dashed lines in Fig. 3.7. This light can therefore be seen as representing the stars in the unmasked

### 3 The optical emission from intracluster stars at $z \sim 0.25$

**Table 3.1:** ICL–galaxy connection: SB and relative flux and flux excess of the diffuse light at different distance from bright galaxies.

$R$ kpc (1)	$l$ kpc (2)	$\mu_{r,0.25}$ mag arcsec $^{-2}$ (3)	$F$ (4)	$F_{\text{excess}}$ per cent (5)	Area (6)
100–200					
	0–15	25.85	5.7	5.0	0.8
	15–25	26.53	13.4	10.6	3.7
	25–40	27.29	16.7	9.8	9.3
	> 40	28.24	64.2	–	86.2
200–400					
	0–15	25.96	10.0	9.7	0.6
	15–25	26.77	20.2	18.8	2.6
	25–40	27.76	20.6	17.0	6.6
	> 40	29.65	49.2	–	90.2
400–750					
	0–15	26.07	19.4	19.3	0.5
	15–25	26.97	33.4	33.1	1.9
	25–40	28.13	29.5	28.6	4.9
	> 40	31.89	17.7	–	92.7
800–900					
	0–15	26.08	–	–	–
	15–25	27.01	–	–	–
	25–40	28.13	–	–	–
	> 40	–	–	–	–

outer regions of individual galaxies.

The SB excess around galaxies is about a quarter of the total diffuse light in the 100–200 kpc annulus. For 200–400 kpc it is almost half of the *diffuse* light. At 400–750 kpc it accounts for more than three quarters of the ICL. However, a comparison with the total flux including galaxies, shows that the excess flux within 25 kpc represents a fraction between 2 and 7 per cent of the galaxy emission, and thus is well accounted for by the corrections for masking incompleteness described in Sec. 3.4.1. The contribution from SB excesses in pixel with  $25 \text{ kpc} < l < 40 \text{ kpc}$  cannot be accounted for by masking incompleteness, both because it is inconsistent with the estimated corrections and because of the relatively large distance from the galaxies. We therefore conclude that our measurements are consistent with the ICL being dominated by a diffuse emission concentrated in the inner  $\sim 300\text{--}400$  kpc plus a fraction

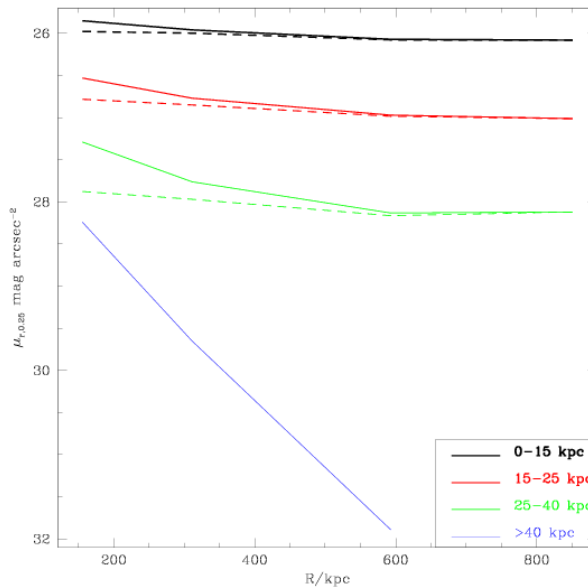


**Figure 3.7:** SB profiles of regions at different distances from bright galaxies. Colours correspond to four distance bins, as indicated in the legend. Dashed lines represent the SB excess with respect to regions at distance  $l > 40$  kpc.

of light clustered around bright galaxies, that dominates in the outer parts.

### 3.5.5 Dependence on cluster properties: SB profiles

In this section and in the following one we analyse the dependence of the distribution and integrated amount of the ICL on global cluster properties. The description of the subsamples is given in Sec. 3.2.1. In order to compensate for the decrease of  $S/N$  due to the smaller number of clusters stacked in each subsample, we utilise the  $r + i$  composite images, obtained as the weighted average of the final stacked images in the two bands; the weights are given for each pixel by the inverse variance of the intensity of the corresponding pixels in the images to be stacked.

In the two graphs of Fig. 3.8 we compare the SB profiles and the ICL fractions of two pairs of subsamples with those of the main sample. In the bottom panels we plot the SB of the *total* light. The panels in the middle display the corrected SB of the *ICL+BCG* component; the dashed lines represent de Vaucouleurs fits to the inner profiles, derived as explained in the previous section. In the top panels we show the local ratio of *ICL+BCG* to the *total* light (solid

### 3 The optical emission from intracluster stars at $z \sim 0.25$

---

lines) and the same quantity after subtracting the de Vaucouleurs fit to the inner profiles (dashed lines). Black lines are used for the main sample (“All”).

On the left we compare clusters with luminous (“L”) and faint (“F”) BCGs, using red thick lines and blue thin lines respectively. The SB profiles are very similar outside 100 kpc, but they are offset, the “L” clusters being brighter than the main sample, and the “F” being fainter. Except for the central regions, the offset is similar in the *ICL* and in the *total* light: “L” and “F” clusters therefore appear to have similar relative amount of ICL with respect to the total emission. However, we note a systematic enhancement of the ICL fraction by a few per cent in the “L” relative the to “F” clusters. The largest differences are observed in the central regions, where the emission is dominated by the BCG: the most luminous BCGs have larger effective radii ( $R_e \sim 23$  kpc) than the mean ( $R_e \sim 19$  kpc), whereas faint BCGs have smaller effective radii ( $R_e \sim 11$  kpc). The difference in luminosity of the de Vaucouleurs fits to the two classes is a factor of 2.3.

The comparison between clusters of different richness, as determined from the number of red-sequence galaxies, is illustrated by the graphs on the right. Here red thick lines represent rich clusters ( $N_{\text{gal}} > 22$ ), while blue thin lines are used for poor clusters ( $N_{\text{gal}} < 17$ ). Again we observe a great similarity between the profiles. As expected, richer clusters are brighter than the mean, and poor clusters are fainter, both in the *total* emission and in the *ICL*. Within 700 kpc the ratio of the *total* luminosities of the two classes is 1.8 (1.7 for the *ICL*). The effective radius of the central  $R^{1/4}$  profile is somewhat larger in the rich clusters ( $R_e \sim 23$  kpc, similar to “L” clusters), than in the poor ones ( $R_e \sim 16$  kpc, close to the average value, and significantly larger than in “F” clusters). At  $R > 100$  kpc the rich clusters exhibit significantly higher SBs with respect to the mean, whereas the poor ones are only slightly fainter. Considering the large uncertainties in the profile of the poor clusters beyond 400 kpc, the fractions of ICL appear to be fully consistent between the different richness subsamples, ranging from 20 to 5 per cent approximately over the radius range 150 to 500 kpc.

In Fig. 3.9 we compare the same four subsamples, by plotting the difference in SB with respect to the mean profile, for the *total* light (bottom panel) and for the *ICL+BCG* component (top panel). Different samples are represented with different lines as indicated in the legend. In the inner 100 kpc we clearly see that the largest differences are observed between the “L” and “F” subsamples. This is not surprising, since this is the region where the BCG dominates. Although the cluster richness correlates with the luminosity of the BCG, clusters in the same richness class can have different BCG luminosity, thus making the separation between rich and poor clusters relatively small

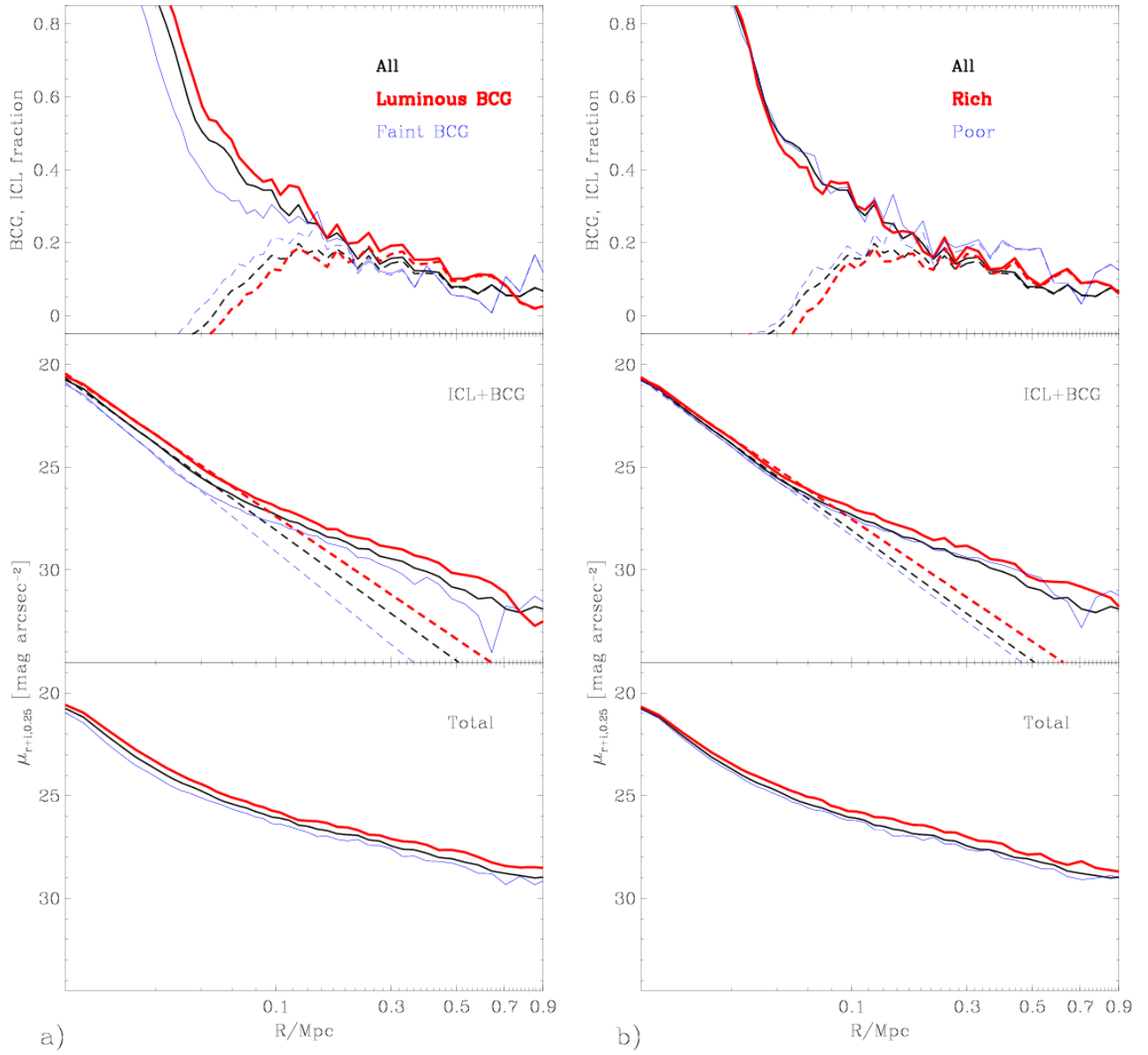


**Figure 3.8:** Comparison between different subsamples. Black lines represent the main sample, here shown as reference. Panel a): clusters with a luminous BCG (red thick lines) vs. clusters with a faint one (blue thin lines). Panel b): Rich (red thick) vs. poor (blue thin) clusters. In the three sections of each panel we plot, from the bottom to the top, the total light SB profile, the ICL+BCG SB profile, with dashed lines representing the de Vaucouleurs fitting to the inner data-points, and the ICL+BCG fraction, with dashed lines displaying the ICL fraction after subtracting the inner de Vaucouleurs fitting.

### 3 The optical emission from intracluster stars at $z \sim 0.25$

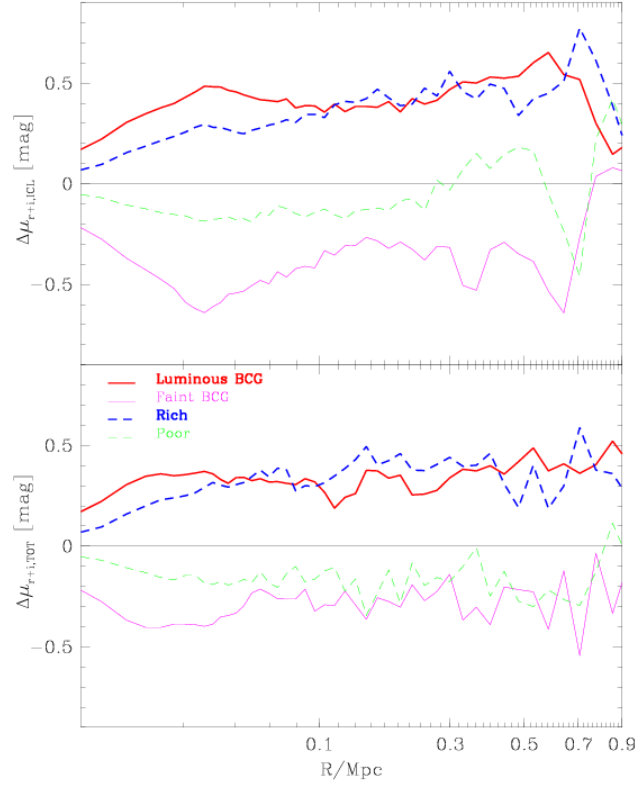


**Figure 3.9:** Comparisons between different subsamples: SB difference between the subsamples and the main sample. Red thick solid lines are used for clusters hosting a luminous BCG, magenta thin solid for faint BCG, dashed thick blue for rich clusters, and dashed thin green for poor clusters. The bottom panel displays the SB differences as a function of the radius for the *total* light, the top panel those for the corrected *ICL+BCG* component alone.

in the centre. At larger radii the influence of the BCG is smaller, and the total SB is almost equally affected by the richness parameter and by the BCG luminosity. Nevertheless, the SB of the ICL appears more strongly suppressed in “F” clusters than in the poor ones.

#### 3.5.6 Dependence on cluster properties: integral photometry

We further investigate the dependence of the relative luminosity of the cluster components on the BCG luminosity and on the richness by analysing the inte-

grated photometry of the stacked  $r + i$  images of a set of smaller subsamples. The main sample is thus divided into 5 subsamples according to  $m_{r,0.25}(\text{BCG})$ , and 5 subsamples in  $L_{RG}$ . The  $m_{r,0.25}(\text{BCG})$  subsamples comprise roughly 140 clusters each, while those in  $L_{RG}$  have 170 clusters each in the three lower luminosity classes, and 110 and 60 clusters each in the two bins at the highest luminosities (these different numbers derive from the skewness of the  $L_{RG}$  distribution). The total luminosity of the red-sequence galaxies  $L_{RG}$  is used here as a proxy to the richness instead of the number of red galaxies, because of its property of being a continuous rather than a discrete variable (see Sec. 3.2.1). In each subsample and for each cluster component (galaxies, BCG, ICL) we measure the integrated flux within 500 kpc, and express this as a fraction of the total. The total flux is obtained directly from the *total* light images. The corrected *ICL+BCG* flux is split into a BCG component and the ICL. The BCG flux is given by the integrated flux within the radius out to which the inner de Vaucouleurs' profile is fitted plus the integral of the fitting profile extrapolated to the outer boundary, while the remaining corrected *ICL+BCG* flux is attributed to the "pure" ICL. Finally, the galaxy flux is just given by the difference between the *total* and the corrected *ICL+BCG* flux.

The same analysis for the complete main sample yields a ratio galaxies:BCG:ICL of 67.2:21.9:10.9 (uncertainty about  $\pm 1.0$ ). Note the small size of the errors here, which is a consequence of our very large sample.

The results for the subsamples are reported in Fig. 3.10, as a function of  $m_{r,0.25}(\text{BCG})$  (left panel) and  $L_{RG}$  (right panel). The vertical error bars on the fluxes and fractions take into account background uncertainties and surface brightness fluctuations within the apertures; no error on the de Vaucouleurs' fit to the BCG is included. We caution that such error bars must be regarded as representing the formal photometric errors in the stacked images, and do not reflect a fully realistic estimate of the total uncertainties. These can be inferred approximately from the scatter of values from our 5 independent subsamples around any smooth trend. The horizontal error bars cover the range of luminosity included in each subsample, while the point is plotted at the average value.

Starting with the flux enclosed within 500 kpc as a function of  $m_{r,0.25}(\text{BCG})$  (Fig. 3.10, left panel), we note that the luminosity of the galaxy component displays a weak correlation with the luminosity of the BCG, whereas only the clusters with the most luminous BCGs have significantly higher ICL luminosity. The fraction of light provided by the BCG increases from 15 to 25 per cent from the lowest bin to the highest ones, whereas the fraction contributed by galaxies decreases from 75 to 63 per cent. The ICL percentage, instead, is almost constant around 10 per cent.

### 3 The optical emission from intracluster stars at $z \sim 0.25$

---

As a function of the luminosity on the red sequence (Fig. 3.10, right panel), we observe weak trends in the total luminosity and in the galaxy and BCG emission. Although the brightening of  $\sim 1.1$  mag in the galaxy component is roughly consistent with the increase of 0.5 dex in  $L_{RG}$  over our 5 bins, a very weak correlation is seen in the four lowest bins. The richest clusters display substantially higher total and galaxy luminosities. Though shallow, a clear correlation between BCG luminosity and richness is present. The richest clusters appear also to have the most ICL. Focusing on the relative fractions, we observe no significant trend in all components in the 4 lowest bins: the BCG component represents  $\sim 23$  per cent of the total luminosity, the galaxies  $\sim 67$  per cent and the ICL  $\sim 10$  per cent. In the richest clusters the contribution of galaxies grows to 73 per cent, that of the BCG decreases to 16 per cent, while the ICL is responsible for  $\sim 11$  per cent of the total flux, as in the other bins.

In both these plots it is consistent to interpret all variations about the mean ICL fraction of 10.9 per cent just as due to sampling error, that we can estimate around 3–5 per cent.

## 3.6 Systematic uncertainties

The results presented in the previous sections are affected by systematic uncertainties that arise from the methods adopted to estimate the background level and the contamination from galaxy light that fails to be masked. In this section we address these issues by analysing the origins and quantifying the possible amount of such systematic errors.

### 3.6.1 Background subtraction

As explained above, the background subtraction is based on fitting an NFW profile plus a background constant to our raw SB profiles. From previous studies (e.g. Carlberg et al. 1997) we know that the NFW profile fits well the mean number density profile for galaxies in clusters. Thus our method appears rigorously justified as far as the galaxy light is concerned, provided one excludes the cuspy profile of the BCG. Given that the galaxy component is dominant, especially at large clustercentric distances, the NFW approximation should hold for the *total* light profile too. On the other hand, there is no reason *a priori* to expect the ICL to follow any particular fitting function. Nevertheless, we find that the NFW profile is a reasonably good approximation to our ICL profile (with an average chi-squared per degree of freedom of  $\sim 1.5$ ). Since we are interested only in a smooth and physically reasonable

### 3.6 Systematic uncertainties

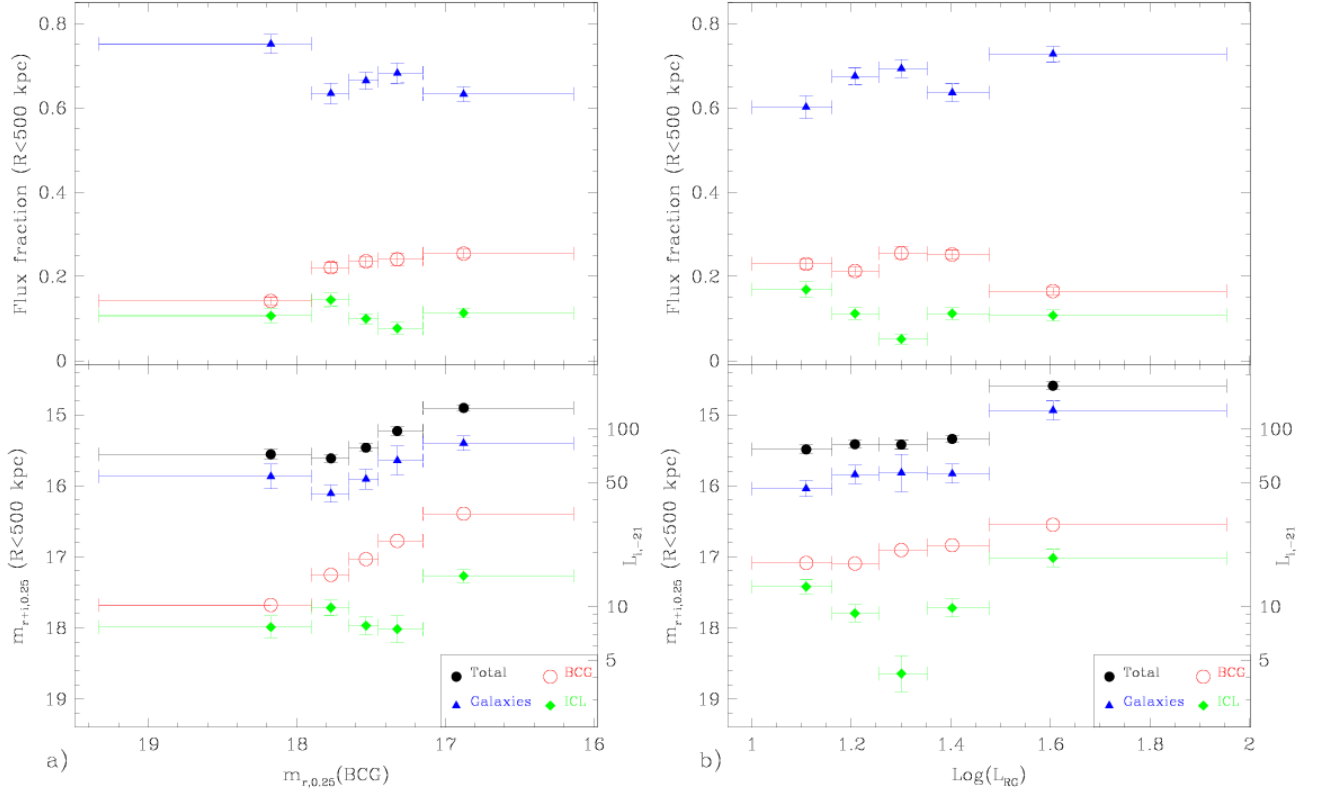


**Figure 3.10:** The dependence of the integrated magnitude within 500 kpc (lower section) and of the relative fraction (upper section) of different cluster components on the luminosity of the BCG (panel a)) and on the total luminosity of the red-sequence galaxies (panel b)). BCG luminosity is expressed as  $z = 0.25$  observer frame  $r$  mag, while the total luminosity of the red-sequence galaxies is given in units of luminosity corresponding to  $-21$  absolute  $i$ -band mag. The integrated luminosities are expressed in  $m_{(r+i),0.25}$  and in units of  $-21$  absolute  $i$ -band mag on the left side and right side axis respectively. Different symbols and colours are used for the different components as indicated in the legend box. Horizontal error bars show the range of luminosity encompassed in each of the four bins, whereas the vertical error bars display the uncertainty due to the background fluctuations.

extrapolation of the SB profile and given that the extrapolation required is tiny (the last measured points are just  $31\text{--}31.5$  mag arcsec $^{-2}$  above the background), the use of the NFW law appears justified for the ICL as well. Note that the background uncertainties used in the previous section just take

### 3 The optical emission from intracluster stars at $z \sim 0.25$

**Table 3.2:** Fraction of unmasked light  $F$  from galaxies of different  $M_r$ .

$M_r$	-22.0	-21.0	-20.0	-19.0	-18.0	-17.0
$f$ (per cent)	2.74	5.02	8.83	18.21	67.40	99.67

statistical uncertainties in the fitted background level into account. Different choices for the background subtraction strategy can yield results differing by up to a few per cent in the integrated fluxes. Considering the SB profiles, the influence of any reasonable systematic shift of the background level is negligible for all the points within 500 kpc. The use of extended image stripes from continuous SDSS scans would, in principle, provide sufficient coverage to directly estimate the background level at large clustercentric distances ( $\gtrsim 2 R_{200}$ ). We will test this possibility in future work.

#### 3.6.2 Corrections for mask incompleteness

In Sec. 3.4.1 we have computed the fraction of galaxy light that escapes our masking algorithm, based on the observed surface brightness profiles of galaxies of different luminosities, and assuming that the number of galaxies as a function of absolute magnitude is well represented by the luminosity function (LF) of the Coma cluster (Mobasher et al. 2003). This is the best studied LF in a rich, massive, regular galaxy cluster, and extends to quite a faint limit  $M_R = -16$ ; thus our choice is justified. However, the LF of a single rich, massive, regular cluster at the present epoch may not be representative of the broad range of luminosities covered by our sample at redshift 0.25 (corresponding to  $\sim 20$  per cent of the cosmic time). Therefore, it is worth investigating how the fraction of light that is missed by our masks changes if a different LF is used and trying to constrain the possible LF with the available photometric data.

First, using images simulated as described in Sec. 3.4.1, we evaluate the fraction of unmasked light as a function of the absolute  $r$  magnitude of a galaxy and analyse which galaxies are the main contributors of unmasked light. We estimate its total relative amount in a range of Schechter’s function parameters and infer the resulting ICL fractions.

The fraction  $f$  of unmasked light for galaxies of different absolute  $r$  magnitude is reported in Table 3.2.

Values are close to 0 for bright galaxies. They smoothly increase up to roughly 0.1 for galaxies of  $-20$ , and then there is a significant upturn at  $-19$ , that leads to most of the light of faint galaxies being missed by our masks. By

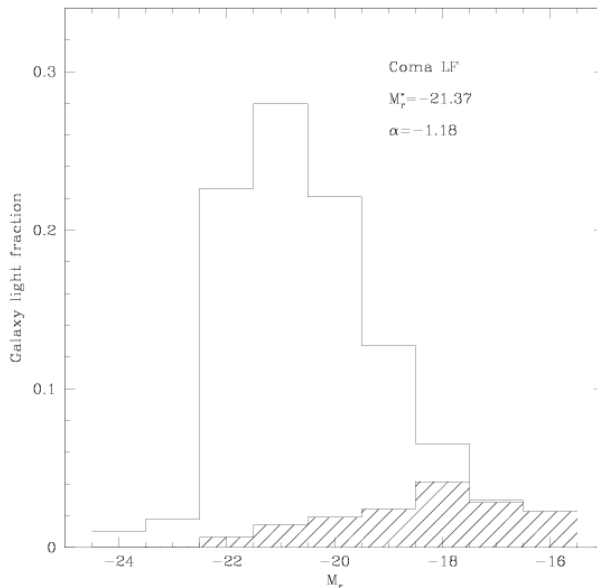


**Figure 3.11:** The fraction of galaxy light contributed by galaxies of different luminosities (empty histograms), and missed by our masking algorithm (shaded histograms) adopting the Schechter fit to the Coma LF.

integrating over the entire LF<sup>8</sup> we are then able to derive the relative galaxy luminosity that contributes to the diffuse component. In Fig. 3.11 the unshaded histogram shows the relative contribution of galaxy light in different bins of absolute  $r$ -band magnitude, according to the Coma LF, while the shaded histogram represents the fraction of unmasked light. The first (last) bin includes also the contribution from all the galaxies brighter (fainter) than the nominal value. While the distribution of galaxy light peaks around the characteristic magnitude  $M^*$  of the luminosity function, we see that most of the unmasked light comes from galaxies that are at least 2.5 mag fainter than  $M^*$ .

Dimming  $M^*$  increases the contribution of unmasked light from near- $M^*$  galaxies, while steepening the faint-end increases the contribution from faint galaxies. Both variations increase the total fraction of unmasked light. These effects are illustrated and quantified in the left panel of Fig. 3.12. For a whole range of  $(\alpha, M^*)$ , the unmasked light fraction is coded by colour-scale

<sup>8</sup>We arbitrarily truncate all the LFs at  $M_r > -14.0$ , in order to make LFs with  $\alpha \leq -1$  integrable. Galaxies fainter than this limit contribute less than 0.1 per cent of the total luminosity in the range of parameters explored.

### 3 The optical emission from intracluster stars at $z \sim 0.25$

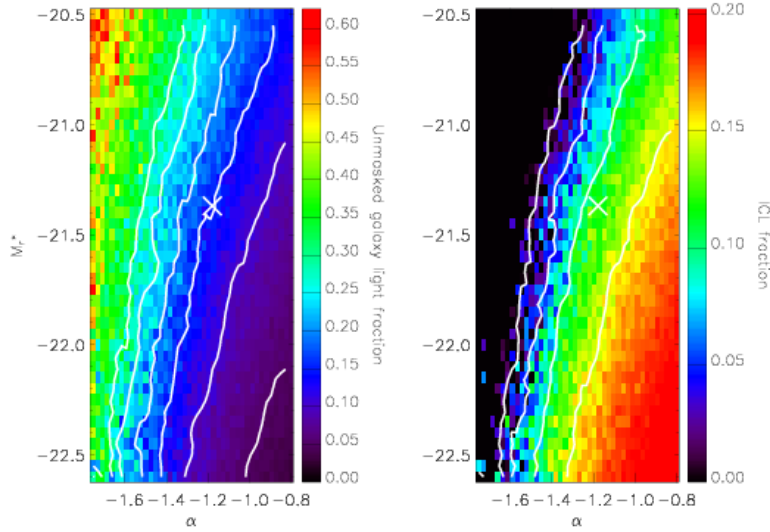


**Figure 3.12:** Fractions of unmasked galaxy light (left panel) and correspondent ICL estimated fraction (right panels) as a function of the assumed LF parameters, coded in colour-scale levels according to the legend bars. Contours show curves of equal fractions in 0.05 intervals, from 0.05 to 0.25 for the unmasked fraction, and from 0 to 0.15 for the ICL. The cross represents the location of the Coma LF.

levels, as indicated. Lines display the curves of constant unmasked fraction, from 0.05 to 0.25 in steps of 0.05, and the cross corresponds to the Coma LF. Taking this point as a reference, we see that steepening the faint-end by 0.2 can dramatically increase the unmasked fraction to  $\sim 25$  per cent, whereas dimming  $M^*$  by 0.4 mag is required to get to 20 per cent. Going to brighter  $M^*$  and less steep slopes, the gradient of unmasked fraction  $f(\alpha, M^*)$  becomes shallower, so that a fraction of 10 per cent requires brightening  $M^*$  by almost 1 mag, or making the slope shallower by 0.15.

These fractions can be translated into estimates of ICL within 500 kpc, based on the *diffuse* light we have measured, as shown in the right panel of Fig. 3.12. Similarly to the previous plot, estimated ICL fractions are represented as gray scale intensities in the  $(\alpha, M^*)$  plane. Lines are curves with the same ICL fraction, from 0 to 0.15 in 0.05 step and the cross corresponds to the Coma LF. The trend is opposite to the previous plot, brighter  $M^*$  and less steep slopes implying higher ICL fraction. The range of variation is between 0 and 20 per cent. A very interesting feature of this plot is the presence of a “zone of avoidance” to the left of the 0 level contour, where the amount of unmasked light would be larger than the *diffuse* light. This excludes all the

LFs with very steep faint-end<sup>9</sup>  $\alpha \lesssim -1.5$ . Applying the same argument to the local fraction of *diffuse* light shown in Fig. 3.5, we conclude that the fraction of unmasked light cannot be larger than 20 per cent. In turn, this implies *i*) that the fraction of ICL integrated within 500 kpc must be at least 6.5 per cent, and *ii*) that a faint-end steeper than  $\alpha = -1.35$  is inconsistent with our data, unless we assume  $M^*$  very different from the reference value for Coma. As an additional piece of evidence against very steep faint-end LF, we note that the colours of the ICL shown in Fig. 3.5 d) are the same as or marginally redder than those of the total light. If the ICL was dominated by dwarf galaxies, any reasonable colour-magnitude relation would imply bluer colours than those of the total light.

The natural upper limit to the ICL fraction is given by the fraction of *diffuse* light, that is 21 per cent, which is obtained in the limit of no unmasked light. On the other hand, if we adopt the “brightest” LF in literature, namely the one by Goto et al. (2002) ( $\alpha = -0.85$ ,  $M_r^* = -22.21$ ) based on 204 SDSS nearby clusters, we obtain an ICL fraction of 17 per cent ( $f = 5$  per cent). This LF has a very bright  $M_r^*$  and a very shallow faint-end in comparison to all other measurements in literature.

Although we cannot go very deep and investigate the faint-end, we have measured the composite LF of our clusters (excluding the BCGs) by using the SDSS photometric catalogues and applying statistical subtractions. Our LF is complete to  $r = 22$  ( $M_r = -18.4$ ) and clearly indicates that  $M^*$  is the same as in Coma within a few 0.01 mag, sufficient to exclude the LF of Goto et al. (2002) as a good description of our clusters and to limit the possible choice of LF parameters.

Adding the fact that, in the light of most of the LF studies in literature,  $\alpha > -1$  seems implausible, we arrive at a tightly constrained region in the space of possible parameters:  $M_r^* = -21.37 \pm 0.1$ ,  $-1.35 < \alpha < -1$ . This translates into an uncertainty of  $\pm 5$  per cent in the estimated fraction of ICL.

### 3.7 Discussion

In previous sections and particularly in Fig. 3.5, we have presented surface photometry from the stacking of 683 clusters of galaxies (our main sample). We have been able to measure SB as deep as  $\mu_{r,0.25} \sim 32$  mag arcsec<sup>-2</sup> for the ICL light and  $\mu_{r,0.25} \sim 29.0$  for the total light, out to 700 kpc from the

<sup>9</sup>This argument rigorously applies only to a Schechter LF. However, the excess of dwarf ellipticals fainter than  $M_R = -15$  found in Virgo (e.g. Trentham & Hodgkin 2002; Sabatini et al. 2003) are unlikely to produce additional contamination larger than 1 per cent.

### 3 The optical emission from intracluster stars at $z \sim 0.25$

---

BCG. Such SBs translate into rest-frame  $g$ -band SBs which are roughly 1 mag arcsec<sup>-2</sup> brighter, as can be easily seen considering the  $(1+z)^4$  cosmological dimming and the fact that the  $r$  band at  $z = 0.25$  is centred at  $\lambda'_{\text{eff}} = \lambda_{\text{eff}}/(1+z) \sim 5000 \text{ \AA}$ .

Looking at the profiles reported in Fig. 3.5 we see that: *i*) the inner  $\sim 50$  kpc are well reproduced by an  $R^{1/4}$  law; *ii*) a significant excess of diffuse light with respect to the inner  $R^{1/4}$  law is clearly seen beyond 100 kpc out to 700 kpc; *iii*) the SB of the ICL decreases faster than the total SB of the cluster, i.e. the ICL is more centrally concentrated than the light of the cluster as a whole. The inner de Vaucouleurs component is comparable in size with the BCGs observed by Schombert (1986). In fact, the average profile obtained from the stacking of our main sample has an effective radius  $R_e \simeq 19$  kpc, which roughly corresponds to the median value of  $R_e$  in his sample.

SB excesses with respect to an  $R^{1/4}$  law at large radii ( $\gtrsim 100$  kpc) from the BCG have recently been observed by Gonzalez, Zabludoff, & Zaritsky (2004) in a sample of 24 clusters at  $0.03 < z < 0.13$ . They represent these excesses as a second  $R^{1/4}$  component with larger  $R_e$ . Parametrising the SB excesses in our data in terms of  $R^{1/4}$  law between 150 and 500 kpc, we find an effective radius  $R_e \sim 250\text{--}300$  kpc, consistent with the range of outer  $R_e$  measured by Gonzalez, Zabludoff, & Zaritsky (2004), although their distribution is peaked at a somewhat lower value, around 100 kpc. However, the ratio of the  $R_e$  of our two components is 0.06–0.07, fully consistent with their results. The ICL is significantly more concentrated than the total light. Uncertainties or bias deriving from background subtraction and from the estimate of contamination are very unlikely to change this result significantly.

In contrast to our own results and those of Gonzalez, Zabludoff, & Zaritsky (2004), Feldmeier et al. (2004c) have recently claimed that the intracluster star density, as measured from planetary nebulae, does not change as a function of radius or projected galaxy density in the Virgo cluster. This may partly be explained by the young dynamical status of this cluster. However, large field-to-field variations in their estimated SB and their sparse sampling of the cluster region prevent us from drawing firm conclusions. In particular, it is noticeable that the fields at the largest distances from M87 are actually close to M49, which is known to be associated with a major sub-cluster: it is no surprise, therefore, that the estimated SB in those fields is much higher than expected from any SB–radius relation.

Numerical simulations published to date make a variety of different predictions for the slope of the outer de Vaucouleurs component, ranging from  $\sim 400$  kpc (Willman et al. 2004) to 70–100 kpc (Sommer-Larsen, Romeo, & Portinari 2004). Our results seem to favour the models with larger  $R_e$ . It is interesting to note that Murante et al. (2004) produce steeper profiles for

the ICL than for the galaxy component in their simulated clusters, and hints of similar behaviour are visible in the simulation of Willman et al. (2004) as well.

Is the measured SB excess contributed by genuine intracluster stars, that is stars orbiting freely in the cluster potential rather than bound to individual galaxies? There are several indications that this is actually the case. The change in slope of the *ICL+BCG* profile and the change in its colour gradient at  $R \sim 70$  kpc suggests strongly that the BCG and ICL components can be considered as distinct stellar populations with different assembly histories. We note that the diffuse light extends continuously well beyond the radius  $R \sim 300$  kpc at which the enclosed stellar mass (as traced by the light) begins to be dominated by galaxies other than the BCG. At larger clustercentric distances the dynamics of the diffuse stellar population must be dominated by the cluster potential, rather than that of the BCG. The fact that we do not see any discontinuity in the diffuse light profile nor any colour gradient going from 100 kpc to the outer regions, lends support to the idea that the stars contributing the SB excess in the inner regions have similar dynamical properties to those at larger distances, and so also orbit freely in the cluster potential.

Based on our analysis of the correlation between the diffuse light and the galaxy distribution, we can exclude the possibility that all or most of the diffuse light is physically linked to individual non-central galaxies, at least at projected radii below 300 kpc. This conclusion is reinforced by the different concentration of the two components.

Surface brightness excesses spatially associated with bright galaxies on scales up to 40 kpc contribute significantly to the ICL. For example, at clustercentric distances of 400–750 kpc, SB excesses surrounding galaxies on this scale sum up to  $\gtrsim 80$  per cent of our total measured ICL. From our analysis alone we cannot argue about the origin of this excess. However, observations of individual clusters reported by several authors (e.g. Trentham & Mobasher 1998; Gregg & West 1998; Calcáneo-Roldán et al. 2000; Feldmeier et al. 2002, 2004b), suggest that tidal structures like plumes and arcs may be good candidates for some of it. In fact, smooth bound low-surface brightness haloes around individual galaxies appear unlikely to account for all the light excess, given the large spatial scale, which is larger than the typical optical size of cluster galaxies (e.g. Binggeli, Sandage, & Tammann 1985) and comparable with or larger than the expected tidal radii of galaxies in clusters (Merritt 1984).

Further support for our identification of the diffuse light as a distinct component comes from our analysis of isophotal shapes for clusters where the

### 3 The optical emission from intracluster stars at $z \sim 0.25$

---

BCG is substantially flattened: in Fig. 3.6 we have shown that the ICL is significantly more flattened both than the BCG “core” itself and than the galaxy distribution. Examples of flattening of the BCG’s outer halo with respect to its inner parts have been known since the late 1970s (Dressler 1979; Porter, Schneider, & Hoessel 1991), as an association with a similar flattening of the galaxy distribution (e.g. Binggeli 1982). Our ellipticities and the corresponding radial dependences are completely consistent with those of Gonzalez, Zabludoff, & Zaritsky (2004). Moreover, extending the observed radial range well beyond 100–200 kpc, we can present evidence for an asymptotic value for this ellipticity, which is only suggested by their data, although predicted by the two-component de Vaucouleurs models which they fit to the BCG+ICL surface brightness distribution. The fact that this asymptotic ellipticity is first reached where the slope of the SB of the diffuse light flattens lends further support to the hypothesis of a distinct second component responsible for the outer profile. In addition to this, it is intriguing that the change in slope and ellipticity occurs where the galaxy component begins to dominate the total SB, apparently establishing a link between the galaxies and the “true” ICL.

During the last decade many attempts have been made to assess the total amount of ICL and its contribution to the total cluster light. Current estimates based on different methods range from less than 10 per cent for poor groups of galaxies (Feldmeier et al. 2004a) to  $\lesssim 20$  per cent for non-cD clusters (Feldmeier et al. 2004b), to 20–40 per cent for cD clusters (Schombert 1988; Feldmeier et al. 2002) and up to  $\sim 50$  per cent for Coma ( $R \lesssim 500$  kpc, Bernstein et al. 1995, but at  $< 25$  per cent according to Melnick, Hoessel, & White 1977). The results presented in Sec. 3.5.6 indicate that in the mean the ICL contributes  $10.9 \pm 1$  per cent of the flux within 500 kpc, while the de Vaucouleurs component of the BCG contributes  $21.9 \pm 1$  per cent. We warn that the uncertainties reflect the measurement errors only, and we expect the overall uncertainty (sampling plus systematic) in this measure to be about 5 per cent for the ICL and 3 per cent for the BCG. Variations between individual clusters are of course likely to be much larger. Our results thus favour a quite low average ICL fraction, compared to previous estimates. This conclusion is not particularly biased by the properties of our sample, where intermediate and low mass clusters dominate: similar fractions are obtained almost independent of cluster richness and BCG luminosity. This apparent discrepancy points to the problem of how estimates of ICL are derived with different methods and to the need to obtain reliable cross calibrations.

In our analysis of different subsamples, binned in luminosity of the BCG and in richness, we found that richer clusters, and those with a more luminous BCG, have brighter ICL than poor clusters or clusters with a faint BCG. If

we consider the local ICL fractions, however, the variations between different classes are no more than  $\pm 5$  per cent, because the total SB varies roughly in the same way as that of the ICL. On the other hand, binning the clusters in finer  $L(\text{BCG})$  and richness classes, we found that a significantly higher ICL luminosity within 500 kpc is measured only in the richest clusters and those having the most luminous BCGs, while no trend is observed in the other classes. As already stated, the fraction of ICL instead is roughly constant, within the uncertainties and the sample variance.

We stress that the quoted luminosities are integrated within fixed metric apertures in all our subsamples. These apertures correspond to different fractions of the virial radius in different clusters and this must be taken into account when comparing our results with fluxes and fractions computed within the virial radius. In fact, a rough extrapolation of the growth curves to the total luminosity  $L_{200}$  within  $R_{200}$  shows that for the poorest clusters  $L_{200}$  is roughly 1.7 times the luminosity within 500 kpc, whereas for the richest clusters  $L_{200}$  is roughly 2.5 times this luminosity. This particularly affects the light fraction contributed by the BCG: although in the fixed 500 kpc aperture the BCG represents an almost constant fraction of the total light, independent of the cluster richness, the same fraction within  $R_{200}$  would show a decreasing trend with richness, as found by Lin & Mohr (2004).

The analysis of the colour profiles in Fig. 3.5 (d) demonstrates that the ICL colours are consistent with (in  $g - r$ ) or marginally redder than (in  $r - i$ ) the average colours of galaxies. This result is compatible with the idea that the ICL originates from stripped stars and disrupted galaxies. Given the relatively large uncertainties in our colour estimates, we cannot test the slightly different predictions obtained by the recent N-body+SPH simulations of Murante et al. (2004), Willman et al. (2004) and Sommer-Larsen, Romeo, & Portinari (2004). In fact, they all agree in predicting that intracluster stars must have roughly the same colours and metallicities as the dominant stellar population in galaxies, but while Murante et al. (2004) and Sommer-Larsen, Romeo, & Portinari (2004) predict slightly larger ages for the intracluster stars, Willman et al. (2004) argue that the typical intracluster stellar population should be similar to those in intermediate luminosity galaxies.

As a final remark, we note that in a scenario where the ICL originates from stripping and galaxy disruption, the galaxies that contribute most of the ICL are those plunging into the cluster potential along nearly radial orbits (e.g. Moore et al. 1996), with some of them eventually merging into the BCG. If there is a significant anisotropy in the orientation of the orbits, a significant elongation in the shape of the BCG and of the ICL should be observable. However, because of the shorter orbital and scattering times at higher densities,

the elongation is expected to increase with increasing clustercentric distances, up to the asymptotic value given by the “original” distribution of orbital parameters. This may explain the outwardly increasing ellipticities of the ICL isophotes which we found above (see Fig. 3.6).

## 3.8 Conclusions

In this paper we have studied the mean properties of the intracluster optical emission of 683 clusters of galaxies between  $z = 0.2$  and  $0.3$ , imaged by the SDSS. Thanks to the high sensitivity achieved by stacking the imaging data, we have been able to trace the average SB profile of the ICL out to 600–700 kpc from the BCG. Measured SB ranges from  $27.5 \text{ mag arcsec}^{-2}$  at 100 kpc to  $\sim 32 \text{ mag arcsec}^{-2}$  at 700 kpc in the observed  $r$  band, which corresponds to  $\sim 1 \text{ mag arcsec}^{-2}$  brighter rest-frame  $g$ -band SB. The ICL fraction depends at most weakly on global cluster properties, such as BCG luminosity and richness. The ICL is ubiquitous in clusters of galaxies, as demonstrated by significant detections in all our subsamples.

We find that the ICL contributes in the mean 30–40 per cent of the total optical emission at around 100 kpc and a decreasing fraction at larger clustercentric distance, down to  $< 5$  per cent at 600–700 kpc. By integrating the fluxes of the different components within 500 kpc we obtain  $10.9 \pm 1.0$  per cent for the fraction of light in the ICL and  $21.9 \pm 1.0$  per cent for the BCG. Taking sampling uncertainties and systematic errors into account, the total errors on these fractions are about  $\pm 5$  per cent for the ICL and  $\pm 3$  per cent for the BCG. Our measurements of the diffuse light put also an independent constraint on the shape of the cluster luminosity function: faint-end slopes  $\alpha < -1.35$  are rejected as inconsistent.

The higher spatial concentration of the ICL with respect to the starlight in galaxies, indicates that the production mechanism for the ICL is more efficient the deeper one goes into the cluster potential well. Comparing different subsamples of clusters, we have observed a significant correlation of the surface brightness of the ICL with the luminosity of the BCG, as well as with the richness of the cluster, suggesting a link between the mechanisms responsible for the growth of the BCG and for the accumulation of intracluster stars.

The similarity in colours between the ICL and galaxies supports a scenario where intracluster stars originate in galaxies and are subsequently dispersed in the intracluster space by dynamical interactions leading to galaxy stripping or disruption. Moreover, the analysis of the shape (ellipticity) of the ICL with respect to the BCG core suggests that the main mechanism acting to create

the ICL is the tidal interaction of galaxies with the central cluster potential. This would also explain the observed link between the amount of ICL and the BCG's luminosity, the latter being strongly correlated to the depth of the potential well.

Due to the very large sample size and to the unprecedented depth of the present observations, our results provide the best and statistically most representative measurement of the intracluster light so far over a wide range of cluster types. Future extensions of our sample to the entire SDSS area and to nearer clusters, and improvements in classification algorithms for galaxy clusters will not only improve the sensitivity of our measurements, but also make it possible to study the relationship between cluster properties and the ICL in greater detail, providing new clues and stronger constraints on dynamical processes during the formation and evolution of galaxy clusters.

## Acknowledgements

We thank Jim Annis for kindly providing us with the maxBCG catalogue of clusters used in this work, and Sarah Hansen for making available unpublished results on the photometric determination of  $R_{200}$ . Thanks to the referee Neil Trentham for comments that have significantly improved this paper, to Anthony Gonzalez and Magda Arnaboldi for very stimulating discussions and the fruitful comparisons of respective results, and to Anna Gallazzi for her precious help.

This paper is dedicated to Jatush Sheth.

Funding for the creation and distribution of the SDSS Archive has been provided by the Alfred P. Sloan Foundation, the Participating Institutions, the National Aeronautics and Space Administration, the National Science Foundation, the U.S. Department of Energy, the Japanese Monbukagakusho, and the Max Planck Society. The SDSS Web site is <http://www.sdss.org/>.

The SDSS is managed by the Astrophysical Research Consortium (ARC) for the Participating Institutions. The Participating Institutions are The University of Chicago, Fermilab, the Institute for Advanced Study, the Japan Participation Group, The Johns Hopkins University, the Korean Scientist Group, Los Alamos National Laboratory, the Max-Planck-Institute for Astronomy (MPIA), the Max-Planck-Institute for Astrophysics (MPA), New Mexico State University, University of Pittsburgh, Princeton University, the United States Naval Observatory, and the University of Washington.

### 3 The optical emission from intracluster stars at $z \sim 0.25$

---

## Bibliography

- Abazajian K., et al., 2003, AJ, 126, 2081
- Abazajian K., et al., 2004, AJ, 128, 502
- Abell G. O., 1958, ApJS, 3, 211
- Abell G. O., Corwin H. G., Olowin R. P., 1989, ApJS, 70, 1
- Arnaboldi M., Freeman K. C., Mendez R. H., Capaccioli M., Ciardullo R., Ford H., Gerhard O., Hui X., Jacoby G. H., Kudritzki R. P., Quinn P. J., 1996, ApJ, 472, 145
- Bahcall N. A., McKay T. A., Annis J., Kim R. S. J., Dong F., Hansen S., Goto T., Gunn J. E., Miller C., Nichol R. C., Postman M., Schneider D., Schroeder J., Voges W., Brinkmann J., Fukugita M., 2003, ApJS, 148, 243
- Bartelmann M., 1996, A&A, 313, 697
- Bernstein G. M., Nichol R. C., Tyson J. A., Ulmer M. P., Wittman D., 1995, AJ, 110, 1507
- Bertin E., Arnouts S., 1996, A&AS, 117, 393
- Binggeli B., 1982, A&A, 107, 338
- Binggeli B., Sandage A., Tammann G. A., 1985, AJ, 90, 1681
- Blanton M. R., Lin H., Lupton R. H., Maley F. M., Young N., Zehavi I., Loveday J., 2003a, AJ, 125, 2276
- Blanton M. R., et al., 2003b, ApJ, 594, 186
- Bruzual G., Charlot S., 2003, MNRAS, 344, 1000
- Calcáneo-Roldán C., Moore B., Bland-Hawthorn J., Malin D., Sadler E. M., 2000, MNRAS, 314, 324
- Carlberg R. G., et al., 1997, ApJ, 485, L13

## Bibliography

---

- de Vaucouleurs G., 1948, *AnAp*, 11, 247
- Dressler A., 1979, *ApJ*, 231, 659
- Durrell P. R., Ciardullo R., Feldmeier J. J., Jacoby G. H., Sigurdsson S., 2002, *ApJ*, 570, 119
- Eisenstein D. J., et al., 2001, *AJ*, 122, 2267
- Feldmeier J. J., Ciardullo R., Jacoby G. H., Durrell P. R., Mihos J. C., 2004a, in Duc P.-A., Braine J., Brinks, E., eds, IAU Symposium no. 217, *Intra-cluster Planetary Nebulae in Clusters and Groups*, Astron. Soc. Pac., San Francisco, p. 86
- Feldmeier J. J., Mihos J. C., Morrison H. L., Harding P., Kaib N., Dubinski J., 2004b, *ApJ*, 609, 617
- Feldmeier J. J., Ciardullo R., Jacoby G. H., Durrell P. R., 2004c, *ApJ*, 615, 196
- Feldmeier J. J., Mihos J. C., Morrison H. L., Rodney S. A., Harding P., 2002, *ApJ*, 575, 779
- Fukugita M., Ichikawa T., Gunn J. E., Doi M., Shimasaku K., Schneider D. P., 1996, *AJ*, 111, 1748
- Gnedin O. Y., 2003, *ApJ*, 589, 752
- Gonzalez A. H., Zabludoff A. I., Zaritsky D., 2004, preprint (astro-ph/0406244)
- Gonzalez A. H., Zabludoff A. I., Zaritsky D., Dalcanton J. J., 2000, *ApJ*, 536, 561
- Goto T., Okamura S., McKay T. A., Bahcall N. A., Annis J., Bernard M., Brinkmann J., Gómez P. L., Hansen S., Kim R. S. J., Sekiguchi M., Sheth R. K., 2002, *PASJ*, 54, 515
- Gregg M. D., West M. J., 1998, *Nature*, 396, 549
- Gunn J. E., et al., 1998, *AJ*, 116, 3040
- Hansen S. M., McKay T. A., Annis J., Kimball A., Sheldon E. S., Wechsler R. H., 2002, *Bulletin of the American Astronomical Society*, 34, 1167
- Hogg D. W., Finkbeiner D. P., Schlegel D. J., Gunn J. E., 2001, *AJ*, 122, 2129

- Ivezić Ž., et al., 2002, in Green R.F., Khachikian E.Ye., Sanders D.B., eds, ASP Conference Proceedings, Vol. 284, AGN Surveys, Astron. Soc. Pac., San Francisco, p. 137
- Jedrzejewski R. I., 1987, MNRAS, 226, 747
- Lambas D. G., Maddox S. J., Loveday J., 1992, MNRAS, 258, 404
- Lin Y., Mohr J. J., 2004, ApJ, 617, 879
- Lupton R. H., Gunn J. E., Ivezić Z., Knapp G. R., Kent S., Yasuda N., 2001, in Harnden F. R., Jr., Primini F. A., Payne H. E., eds, ASP Conference Proceedings, Vol. 238, Astronomical Data Analysis Software and Systems X, Astron. Soc. Pac., San Francisco, p. 269
- Melnick J., Hoessel J., White S. D. M., 1977, MNRAS, 180, 207
- Merritt D., 1984, ApJ, 276, 26
- Mihos J. C., 2004, in Duc P.-A., Braine J., Brinks, E., eds, IAU Symposium no. 217, Intracluster Planetary Nebulae in Clusters and Groups, Astron. Soc. Pac., San Francisco, p. 390
- Mobasher B., Colless M., Carter D., Poggianti B. M., Bridges T. J., Kranz K., Komiyama Y., Kashikawa N., Yagi M., Okamura S., 2003, ApJ, 587, 605
- Moore B., Katz N., Lake G., Dressler A., Oemler A., 1996, Nature, 379, 613
- Murante G., Arnaboldi M., Gerhard O., Borgani S., Cheng L. M., Diaferio A., Dolag K., Moscardini L., Tormen G., Tornatore L., Tozzi P., 2004, ApJ, 607, L83
- Napolitano N. R., Pannella M., Arnaboldi M., Gerhard O., Aguerri J. A. L., Freeman K. C., Capaccioli M., Ghigna S., Governato F., Quinn T., Stadel J., 2003, ApJ, 594, 172
- Navarro J. F., Frenk C. S., White S. D. M., 1995, MNRAS, 275, 720
- Pier J. R., Munn J. A., Hindsley R. B., Hennessy G. S., Kent S. M., Lupton R. H., Ivezić Ž., 2003, AJ, 125, 1559
- Porter A. C., Schneider D. P., Hoessel J. G., 1991, AJ, 101, 1561
- Press W. H., Teukolsky S. A., Vetterling W. T., Flannery B. P., 1992, Numerical recipes in C. The art of scientific computing. Cambridge University Press, Cambridge

## Bibliography

---

- Richstone D. O., 1976, ApJ, 204, 642
- Sabatini S., Davies J., Scaramella R., Smith R., Baes M., Linder S. M., Roberts S., Testa V., 2003, MNRAS, 341, 981
- Schlegel D. J., Finkbeiner D. P., Davis M., 1998, ApJ, 500, 525
- Schombert J. M., 1986, ApJS, 60, 603
- Schombert J. M., 1988, ApJ, 328, 475
- Smith J. A., et al., 2002, AJ, 123, 2121
- Sommer-Larsen J., Romeo A. D., Portinari L., 2004, preprint (astro-ph/0403282)
- Stoughton C., et al., 2002, AJ, 123, 485
- Strauss M. A., et al., 2002, AJ, 124, 1810
- Trentham N., Hodgkin S., 2002, MNRAS, 333, 423
- Trentham N., Mobasher B., 1998, MNRAS, 293, 53
- Welch G. A., Sastry G. N., 1971, ApJ, 169, L3
- Willman B., Governato F., Wadsley J., Quinn T., 2004, MNRAS, 355, 159
- York D. G., et al., 2000, AJ, 120, 1579
- Zibetti S., White S. D. M., Brinkmann J., 2004, MNRAS, 347, 556
- Zwicky F., 1951, PASP, 63, 61

*La filosofia è scritta in questo grandissimo libro  
che continuamente ci sta aperto innanzi a gli occhi  
(io dico l'universo), ma non si può intendere se  
prima non s'impara a intender la lingua e conoscer  
i caratteri, ne' quali è scritto.*

Galileo Galilei, Il Saggiatore

# 4

## Conclusions and outlook

In this chapter I summarize the main achievements of this thesis. Its objective was to study the diffuse stellar haloes around disc galaxies and of the intra-cluster stellar light. This work is interesting not only for the understanding of these diffuse stellar components it has provided, but also for the methodology that has been applied.

In this work I have utilized for the first time the method of stacking a large number of images to measure very low surface brightnesses. A large imaging database, which comprises several hundreds of objects of the same class, is the necessary condition for this statistical technique to be possible. Such a large database has become available only very recently thanks to the Sloan Digital Sky Survey, as described in Section 1.4. In Chapters 2.1 and 3 I have shown that it is possible to reach average surface brightnesses as low as  $30 \text{ mag arcsec}^{-2}$  in the red bands by stacking several hundreds, up to a thousand images, which have been previously processed and masked in order to exclude the flux of polluting sources (fore- and backgrounds). Combining observations of many objects obtained with the same instrumentation, but in different conditions concerning flat-fielding anomalies and the presence of polluting sources, produces a very flat average background: this is one of the primary requirements for carrying out very low surface brightness photometry, but it is also one of the hardest to obtain while observing individual objects. The stacking technique has been proved to be of the greatest usefulness for investigating the average properties of large statistical samples, when suffi-

## 4 Conclusions and outlook

---

ciently deep observations of the individual objects are too demanding.

The analysis of the stacking of 1047 edge-on disc galaxies has demonstrated that stellar haloes are very common around this kind of galaxies. These haloes account for a few per cent of the total luminosity of the galaxy, and have average surface brightnesses which appear to be correlated to the total luminosity. Their SB profiles follow a power-law with index  $\approx -2$  (in projection), and are flattened with a mean axial ratio of 0.6. This is very similar to what is observed in the Milky Way's and M31's haloes. Low surface brightness, power-law haloes thus appear to be a common by-product of the galaxy formation processes. Detailed cosmological simulations and deeper observations in the next future will have to explain the mechanisms responsible for the formation of these haloes; whether they are rapidly formed during the early collapse of the galaxies or by the continuous disruption and accretion of dwarf satellites at later stages.

The comparison of the halo emission in three different bands has produced very puzzling results, lately confirmed by the observations (reported by Zibetti & Ferguson 2004, chapter 2.2) of an edge-on disc at  $z \approx 0.3$  in the Hubble Ultra Deep Field: although the optical colours in the blue-green-red bands are typical of old stellar populations with moderate metal enrichment, a flux excess around  $7500\text{\AA}$  is clearly measured, which is impossible to explain in terms of stellar emissions and might indicate a contribution from ionized gas. Deeper narrow-band observations will be required to solve this problem.

In the study of the intracluster light fundamental advances have been achieved through the stacking of 683 galaxy clusters selected in the redshift interval 0.2–0.3 over  $\approx 1500 \text{ deg}^2$  of the SDSS First Data Release. The average contribution of the intracluster light to the total luminosity has been measured as  $10.9 \pm 5\%$  within a fixed aperture of 500 kpc. The richest clusters and those with the most luminous Brightest Cluster Galaxy (BCG) have been found to have the highest amounts of intracluster stars within this radius. This indicates a possible link between the mechanisms responsible for the formation of the intracluster stars and the depth of the cluster potential well. Further support for this idea comes from the fact that the degree of alignment with the BCG is larger for the ICL than for the other cluster galaxies. A number of observations indicate that the intracluster stars originated from tidal interactions that occur in the deepest regions of the cluster potential well, and lead to the stripping of stars from the outskirts of massive galaxies or, in the most dramatic events, to the disruption of smaller galaxies. In fact, the amount of ICL is found to increase toward the center of the clusters much more rapidly than does the surface density of galaxies. Moreover, the con-

---

sistency between the colours of the ICL and those of the galaxies hints at a common origin; only after formation are some stars stripped and spread into intracluster space, giving rise to the ICL.

Future developments of this research will be focused on the creation of subsamples with very well determined properties in order to better understand which of them have most influence on the presence and distribution of diffuse stars. This will be made possible by the complete dataset of the SDSS, which will significantly enlarge the sample used in this thesis. However, substantial effort will be needed to develop algorithms that can reliably classify galaxies and galaxy clusters according to different properties. Such a project for the edge-on disc galaxies has already been started in collaboration with Lauren Grodnicky, a PhD student at the University of Chicago.

A further step will include the use of very large field imagers of the next generation and the development of appropriate imaging techniques to observe a sample of individual nearby objects, taking advantage of the larger flux reaching us thanks to the smaller distances.

Finally, it is worth mentioning that the image stacking technique has opened new perspectives in the statistical study of large samples of objects, which are now coming from surveys like the SDSS. An example of this kind of application is given by a project aimed at studying the photometric properties of two samples of a few thousand quasars with and without absorbers, that has been started in collaboration with Brice Menard, of the Institute for Advanced Studies in Princeton, and other members of the SDSS collaboration.

A new field of statistical photometry has been started, with plenty of possibilities to study previously inaccessible classes of astronomical objects. The hardest part of the work will be to select appropriate samples: we have to ask the Nature the right questions to get the “right” answers, those that help us understand how the Universe built the stunning variety of structures we observe today.

## 4 Conclusions and outlook

---

## Acknowledgements

Three years are a long time and represent a conspicuous fraction of my life, 10.5% to be precise (but hopefully this fraction is going to decrease with time...). Just to give an idea of how much this is to people familiar with my scientific work, this is very similar the average fraction of ICL in a cluster, but at least a factor two more than the relative light contribution of the stellar halo in a typical disc galaxy...

In such a long period many many people have contributed not only to make my science better and my skills improve, but also to make my life happier, more interesting, and more meaningful. My sincere thanks are due to all of them, even if they are not explicitly mentioned in the next few lines.

Starting from the scientific side, I want to thank my supervisor Simon White for his profound advice and scientific insights, for the many opportunities of exchange with other researchers that he has offered to me, and... for being so patient with my “macaronic” English! Special thanks are due to Annette Ferguson, Amina Helmi, Stéphane Charlot, and Anthony Gonzalez for their help and collaboration, and to Ralf Bender for trusting my skills.

I wish to thank the people in the Sloan collaboration for their direct or indirect contributions to my work, in particular Jim Annis, Michael Blanton, Tim MacKay, Sarah Hansen, Don Schneider, and Michael Strauss.

Many people have contributed to make my life at MPA more pleasant and I am grateful to them. In particular I must mention my friend Gabriella: we have shared the 12 m<sup>2</sup> of the office #241 for almost three years, roughly 12 hours a day. And along with that small space, we have shared interesting discussions about science, life, politics, movies and whatever, bad words, complainings, satisfactions and... her awful cigarette smoke!

Thanks to Greg, for being so persuasive when recruiting speakers for the cosmology seminar or the “wine&cheese”, Jarle, Hugues, Hans-Jacob, Felix, Serena and to our great secretaries Maria, Cornelia and Gabi.

A special mention is due to Manfred Georg Kitzbichler, very nice guy and my official German-speaking translator: without him I would not have been able to hand this thesis in.

Thanks to Luigi, for remembering me that lunch time is at 12.30 sharp every day, Debora, the dark(matter) lady, Maurilio, Veronica, Larry, Giovanna, and

## Acknowledgements

---

all the other friends that I have met here in Garching. And thanks to Roberto for his friendship and all the nice time we spent together in Tom's Bistrot.

No matter how far you are, true friends are always friends, and I want to thank all of them: Nicola (Nikipex), Matteo, Mauro, "gentediuncertolivello" Tommy, Lucia, Alberto and the old astrophysics lab group in Milano. I am also grateful to all my relatives, and to my aunt Amelia in particular, for their nice moral support during these years.

Last but not least... I want to heartily thank the very few people for which no specific motivation is really needed, since they are such an essential part of my life: my girlfriend Anna, my parents Enrico and Piera, to whom this thesis is dedicated, and my sister Anna, with little Costanza and Giovanni.

# Curriculum vitae

## PERSONAL DATA

---

Stefano Zibetti  
born 12 March 1976, in Gallarate (Varese), Italy, Italian citizen

## EDUCATION

---

1982-1987 Primary school at “Scuola Elementare Istituto Betlem” in Gallarate  
1987-1990 Secondary school at “Scuola Media Statale Ponti” in Gallarate  
1990-1995 High school at “Liceo Scientifico Statale” in Gallarate  
June 1995 High school diploma at “Liceo Scientifico Statale” in Gallarate reporting the degree of 60/60

## WORK EXPERIENCE

---

Oct.-Nov. 1995 work as Computer Aided Designer for Helitec S.p.A., in Gallarate, on engineering devices for Agusta helicopters

## ACADEMIC STUDIES

---

Oct. 1995-May 2001 Physics at “Università degli Studi di Milano”  
23 May 1995 “Laurea in Fisica” (Diploma in Physics) at “Università degli Studi di Milano”, final degree: 110/110 cum laude  
Sept. 2001-Fall 2004 PhD at Max-Planck-Institut für Astrophysik, Garching b. München  
“International Max-Planck Research School on Astrophysics” fellowship

## SPECIAL AWARDS

---

May 1995 Winner of the Italian contest for the Physic Olympiad  
July 1995 Participation in the XXV. International Physics Olympiad  
1995 and 1996 I.S.U. (Istituto per il diritto allo Studio Universitario) scholarships  
2001 2nd Winner of “Premio Zagar”-Osservatorio Astronomico di Brera-Milano for the best diploma Theses in Astronomy in Milano